REPORT DOCUMENTATION PAGE

The public reporting burden for this collection of information is estimated to average 1 hour per response, including the time for reviewing instructions, searching existing data sources, gathering and maintaining the data needed, and completing and reviewing the collection of information. Send comments regarding this burden estimate or any other aspect of this collection of information, including suggestions for reducing the burden, to the Department of Defense, Executive Service Directorate (0704-0188). Respondents should be aware that notwithstanding any other provision of law, no person shall be subject to any penalty for failing to comply with a collection of information if it does not display a currently valid OMB control number.

PLEASE DO NOT RETURN YOUR FORM TO THE ABOVE ORGANIZATION.

1. REPORT DATE (DD-MM-YYYY)	2. REPORT TYPE	3. DATES COVERED (From - To)
26-01-2012	Final Report	Aug 1, 2008 - Sept 14, 2011

4. TITLE AND SUBTITLE
Oxidation Resistance, Electrical and Thermal Conductivity, and Spectral Emittance of Fully Dense HfB2 and ZrB2 with SiC, TaSi2, and LaB6 Additives

5a. CONTRACT NUMBER

5b. GRANT NUMBER
FA9550-08-1-0408

5c. PROGRAM ELEMENT NUMBER

6. AUTHOR(S)
Speyer, Robert F.

5d. PROJECT NUMBER

5e. TASK NUMBER

5f. WORK UNIT NUMBER

7. PERFORMING ORGANIZATION NAME(S) AND ADDRESS(ES)
Georgia Tech Research Corporation
505 Tenth Street NW
Atlanta, GA 30332

8. PERFORMING ORGANIZATION REPORT NUMBER

9. SPONSORING/MONITORING AGENCY NAME(S) AND ADDRESS(ES)
Air Force Office of Scientific Research
875 N. Randolph Street, Room 3112
Arlington, VA 22203

10. SPONSOR/MONITOR'S ACRONYM(S)
AFOSR/PKR2

11. SPONSOR/MONITOR'S REPORT NUMBER(S)
AFRL-OSR-VA-TR-2012-0279

12. DISTRIBUTION/AVAILABILITY STATEMENT
Approved for Public Release; Distribution is Unlimited

13. SUPPLEMENTARY NOTES

14. ABSTRACT
The oxidation resistances of ZrB_2 containing SiC, TaB_2, and $TaSi_2$ additions of various concentrations were studied using isothermal thermogravimetry at 1200, 1400, and 1500°C. Theoretically-dense ZrB_2-SiC two-phase microstructures were isothermally oxidized for ~90 min in a thermogravimetric analyzer in flowing air in the range 1500-1900°C. The oxidation resistances of theoretically-dense HfB_2 - SiC test specimens were evaluated via isothermal thermogravimetry at 1600, 1700 and 1800°C. The thermal diffusivities of theoretically dense ZrB_2-SiC (10.7, 21.9, or 48.7 vol% SiC) sintered/HIPed with B_4C sintering aid was measured using the laser flash technique. Spectral emittances of direct electrically-heated ZrB_2-30 mol% SiC specimens were measured in the 1-6 μm range.

15. SUBJECT TERMS
zirconium diboride, UHTC, oxidation resistance, thermal conductivity, spectral emissivity, microstructure, thermogravimetry

16. SECURITY CLASSIFICATION OF:			17. LIMITATION OF ABSTRACT	18. NUMBER OF PAGES	19a. NAME OF RESPONSIBLE PERSON
a. REPORT	b. ABSTRACT	c. THIS PAGE	UU	99	
					19b. TELEPHONE NUMBER (Include area code)

Reset

Standard Form 298 (Rev. 8/98)
Prescribed by ANSI Std. Z39.18
Adobe Professional 7.0

OXIDATION RESISTANCE, ELECTRICAL AND THERMAL CONDUCTIVITY, AND SPECTRAL EMITTANCE OF FULLY DENSE HfB$_2$ AND ZrB$_2$ WITH SiC, TaSi$_2$, AND LaB$_6$ ADDITIVES

Final Report

Robert F. Speyer, Professor, Principal Investigator
School of Materials Science and Engineering
Georgia Institute of Technology
Atlanta, GA 30332-0245
Robert.Speyer@mse.gatech.edu

Executive Summary

This report describes the work performed under AFOSR contract FA9550-08-1-0408. We gratefully acknowledge program managers Drs. Joan Fuller and Ali Sayir. The 1900°C thermogravimetry work was facilitated through the use of a Zircothal furnace from Dr. Jeffrey Furgus at Auburn University, and thermal conductivity measurements were performed under the supervision of Robert Campbell at Netzsch Instruments (Exton, PA). Most of this work has been (or is in the process of being) published in refereed Journals, and each paper is provided herein in the form of a chapter. The overriding theme of the work was to characterize the properties of ZrB_2- (and HfB_2-) based multiphase materials for properties important for aerospace applications. Specifically, as leading edges exposed to frictional heating from the atmosphere, they must be refractory enough to survive the temperatures reached, oxidation resistant, and have adequately high thermal conductivity and emissivity to maintain tolerable steady-state temperatures. Abstracts for each chapter are enumerated below:

1. **Effect of SiC, TaB_2 and $TaSi_2$ Additives on the Isothermal Oxidation Resistance of Fully Dense Zirconium Diboride**[1]
The oxidation resistances of ZrB_2 containing SiC, TaB_2, and $TaSi_2$ additions of various concentrations were studied using isothermal thermogravimetry at 1200, 1400, and 1500°C, and specimens were further characterized using x-ray diffraction and electron microscopy. Increasing SiC concentration resulted in thinner glassy surface layers as well as thinner ZrO_2-rich underlayers deficient in silica. This silica deficiency was argued to occur by a wicking process of interior-formed borosilicate liquid to the initially-formed borosilicate liquid at the surface. Small (3.32 mol%) concentrations of TaB_2 additions were more effective at increasing oxidation resistance than equal additions of $TaSi_2$. The benefit of these additives was related to the formation of a zirconium-tantalum boride solid solution during sintering, which during oxidation, fragmented into fine particles of ZrO_2 and TaC. These particles resisted wicking of their liquid/glassy borosilicate encapsulation, which increased overall oxidation resistance. With increasing TaB_2 or $TaSi_2$ concentration, oxidation resistance degraded, most egregiously with TaB_2 additions. In these cases, zirconia dendrites appeared to grow through the glassy layers, providing conduits for oxygen migration.

2. **Thermogravimetric Analysis of the Oxidation Resistance of ZrB_2-SiC and ZrB_2-SiC-TaB_2-based Compositions in the 1500-1900°C Range**[2]
Theoretically-dense ZrB_2-SiC two-phase microstructures were isothermally oxidized for ~90 min in flowing air in the range 1500-1900°C. Specimens with 30 mol% SiC formed distinctive reaction product layers which were highly protective; 28 mol% SiC - 6 mol% TaB_2 performed similarly. At and above 1700°C, the composition with only 15 mol% SiC oxidized extensively because of deficient silicate liquid formation. Specimens with 60 mol% SiC were resistant to oxidation up to 1800°C; at 1900°C, this composition

[1]F. Peng, Y. Berta, and R. F. Speyer, "Effect of SiC, TaB_2 and $TaSi_2$ Additives on the Isothermal Oxidation Resistance of Fully Dense Zirconium Diboride," *Journal of Materials Research,* **24** [5] 1855-1867 (2009).

[2]F. Peng, G. Van Laningham, and R. F. Speyer, "Thermogravimetric Analysis of the Oxidation Resistance of ZrB_2-SiC and ZrB_2-SiC-TaB_2-Based Compositions in the 1500-1900°C Range," *Journal of Materials Research*, **26** [1] 96-107 (2011).

displayed periodic ruptures of the passivating layer by emerging gas bubbles. Oxide coating thicknesses calculated from weight loss data were consistent with those measured from SEM micrographs. A layer of ZrB_2 devoid of SiC was argued to be from preferential removal of SiC by reaction of silica oxidation product with adjacent unreacted SiC to form escaping gases.

3. **Isothermal Oxidation of HfB_2 - 60% SiC at 1600-1800°C[3]**
The oxidation resistances of theoretically-dense HfB_2 - SiC test specimens were evaluated via isothermal thermogravimetry at 1600, 1700 and 1800°C. Compositions with 15 and 30 mol% SiC propelled out of their crucibles while being raised into the oxidation furnace; such thermal-shock ruptures were not observed with analogous ZrB_2-based compositions in a previous study. HfB_2 - 58.92 mol% SiC specimens were stable against oxidation at 1600 and 1700°C, but displayed more pervasive oxidation at 1800°C, and periodic ruptures of the silicate glass/liquid surface layer. An analogous ZrB_2 - 58.92 mol% SiC composition was more resistant to oxidation at 1800°C, and did not display bubble ruptures at the glass/liquid layer until 1900°C.

4. **Thermal Conductivity of ZrB_2-SiC-B_4C Compositions from 25-2000°C[4]**
The thermal diffusivities of theoretically dense ZrB_2-SiC (10.7, 21.9, or 48.7 vol% SiC) sintered/HIPed with B_4C sintering aid was measured using the laser flash technique. These were converted to thermal conductivities using temperature dependent specific heat and density data; thermal conductivity decreased with increasing temperature over the range 25-2000°C. The composition with the highest SiC content showed the highest thermal conductivity at room temperature, but the lowest at temperatures in excess of $\sim$400°C, because of the greater temperature sensitivity of the thermal conductivity of the SiC phase, as compared to more electrically-conductive ZrB_2. Finite difference calculations, using literature data for the individual phases, and the concentration of phases as depicted in microstructures, were good predictors of multi-phase thermal conductvities for the three compositions. The thermal conductivities of pure ZrB_2 as a function of temperature were back-calculated from the experimental results for the multi-phase materials, and literature thermal conductivities of the other two phases. This established a relatively constant thermal conductivity of 88-104 W/m·K over the evaluated temperature range.

5. **Spectral Emittance of ZrB_2-30 mol% SiC Electrically Heated Ribbons over 1-6 μm[5]**
Spectral radiosities of direct electrically-heated ZrB_2-30 mol% SiC specimens were measured in the 1-6 μ range. Using Wein's displacement law, the temperatures of these specimens were determined, in turn permitting calculation of spectral emissivities via Planck's law. Spectral emissivities decreased slightly with second scans due to degradation of the oxide coatings on the specimens (formed by a prior oxidation heat-treatment) in a flowing Ar environment. Spectral emissivities increased with increasing wavelength, increasing from $\sim$0.7 to 0.9 over the measured spectrum. Over the temperature range of 1100-1330°C, no clear temperature dependence on spectral emittance was detected.

---

[3]Unpublished work.

[4]F. Peng, G. Van Laningham, R. Erdmann, R. Campbell, and R. F. Speyer, "Thermal Conductivity of ZrB_2-SiC-B_4C Compositions from 25-2000°C," In second submission to the *Journal of Materials Research,* January 2012.

[5]In preparation for publication as a Communication.

Chapter 1

Effect of SiC, TaB$_2$ and TaSi$_2$ Additives on the Isothermal Oxidation Resistance of Fully Dense Zirconium Diboride

I Introduction

Transition metal borides including ZrB$_2$, TaB$_2$, and HfB$_2$ are of interest for their ultra-high melting temperature (>3000°C), high hardness and strength, and high thermal and electrical conductivities [1]-[3]. They are candidates for leading edges on re-entry vehicles; their survival against atmospheric frictional heating is dependent of a combination of refractoriness and the ability to dissipate heat through thermal conduction away from the leading edge and radiant emission to the cold ambient. Engineering of these ceramics for oxidation resistance has focused on a two-phase microstructure of ZrB$_2$ and SiC, in which a borosilicate viscous liquid with interdispersed ZrO$_2$ forms as a passivating surface layer.

Oxidation of single-phase ZrB$_2$ does not form a protective surface layer since B$_2$O$_3$ is volatile (boiling point, i.e. 1 atm vapor pressure, of B$_2$O$_3$ is 1860°C). Oxidation heat treatments of ZrB$_2$ + 20 vol% SiC at 1200°C and below have shown weight gain no less extensive than those of specimens composed of ZrB$_2$ alone. However, above 1200°C, a borosilicate coating forms [4, 5]. Given the high volatility of boron oxide, the borosilicate glass surface coating might be expected to become more of a near-pure fused silica coating with increasing temperature. One investigation has shown that the boron content of the oxide layer after heating to 1500°C for 30 min is less than 1 wt% [8]. However, B$_2$O$_3$ vapor pressure is suppressed by its entering into solution with SiO$_2$. Further, standard glass-forming practice melts, homogenizes, and fines borosilicate (e.g. Pyrex) glass compositions at 1550-1600°C with residence times of several hours to days [7]. However, far less of the boron oxide component of this liquid would be exposed to the liquid-vapor interface, where it could volatilize, as would occur in a thin liquid/amorphous coating.

Opila et al. showed that a ZrB$_2$-20 vol% SiC composition exposed to ten 10 min oxidation cycles at 1327 and 1627°C developed protective oxide scales: 30 μm at 1327°C and 150 μm

at 1627°C [4]. Thermal cycling at 1927°C resulted in an oxide layer thickness of over 1 mm. The 1627°C surface oxide coating was identified (via energy dispersive spectrometry) to be silica. Underneath this coating was a region of ZrO_2 dispersed in silica, which in turn was above a region of ZrB_2 depleted of SiC. This region was argued to have resulted from active oxidation of SiC to form $SiO_{(g)}$ [4, 5]. Opeka et al. have suggested that formation of $SiO_{(g)}$ could build up to pressures exceeding ambient, facilitating rupture of the protective glass layer, resulting in a cyclic protective/non-protective scale-forming sequence [7].

In low oxygen partial pressures, formed by $CO_{(g)}/CO_{2(g)}$ mixtures, ZrB_2 oxidized to $ZrO_{2(s)}$ and a volatile boron oxide, and SiC oxidized to carbon monoxide and $SiO_{(g)}$. This left a non-protective (porous) ZrO_2 scale [8]. Han et al. found that for ZrB_2-20 vol% SiC, the thickness of the oxide layer increased and oxidation resistance decreased with decreasing oxygen partial pressure [16]. Karlsdottir et al. showed that zirconia is deposited on the surface of the glassy coating during oxidation at 1550 and 1700°C by convection of a boron-zirconium-silicon oxide liquid phase which evolves volatile B_2O_3 at the surface, precipitating ZrO_2 [3].

Talmy et al. investigated additions of Cr-, Ti-, Nb-, V-, and Ta-borides to ZrB_2-25 vol% SiC, and found that all additions (all of which formed solid solutions with ZrB_2 after sintering) improved oxidation resistance over the base composition, with TaB_2 additions being the most effective [13]. It was found that improved oxidation resistance correlated with increasing cation field strength (defined as Z/r^2, where Z is the valance of the cation and r is the ionic radius) of the added diborides. In a borosilicate or silicate glass with transition metal cations, the tendency toward liquid immiscibility is known to increase with increasing cation field strength of the transition metal. This phase separation has been argued to result in increased viscosity [14], which has been correlated to reduced oxygen diffusion rates [7].

Opila et al. found that $TaSi_2$ additions in the form of a ZrB_2-20 vol% SiC-20 vol% $TaSi_2$ composition showed a lower oxidation rate after cyclic oxidation at 1627°C than a ZrB_2-20 vol% SiC composition [15]. Improved oxidation resistance was related to evidence of phase separation in the amorphous surface layer. The composition containing $TaSi_2$ showed rapid consumption as compared to ZrB_2-20 vol% SiC compositions exposed to similar oxidation heat treatments at 1927°C. This was attributed to melting of Ta_2O_5 (1785°C) and/or compounds of Ta_2O_5 and ZrO_2. Talmy et al. demonstrated enhanced oxidation resistance from adding 8-30 vol% Ta_5Si_3 to ZrB_2 [16]. A purported general advantage of tantalum compound additions is that tantalum can stabilize zirconium oxide, circumventing the tetragonal/monoclinic phase transformation, whose volume change can create fissures in the oxide scale [17].

Zhang et al. have reported that a ZrB_2-SiC composition with 10 vol% LaB_6 additions showed good oxidation resistance at 2400°C (oxyacetylene torch); lanthanum stabilizes the tetragonal form of zirconia, and the $La_2Zr_2O_7$ along with zirconia forms a coherent and compact oxide surface scale [19]. Fahrenholtz et al. have recently shown the benefits of tungsten additions to ZrB_2 [18]. The tungsten functions as a sintering aid to the surface zirconia which forms via oxidation, decreasing the oxygen permeability through this surface layer.

In our previous work [1], the oxidation resistances of ZrB_2 containing SiC, TaB_2 and $TaSi_2$ additives were studied using scanning thermogravimetry (3°C/min) over the range 1100-1550°C. It was shown that SiC additions to ZrB_2 improved oxidation resistance, as did TaB_2, and to a greater extent, $TaSi_2$ additions. In this investigation, relative oxidation

resistances of these compositions and their causes were studied in more detail via isothermal thermogravimetry studies at 1200, 1400, and 1500°C.

II Experimental Procedure

Commercially-available powders were used for raw materials. The major crystalline phase(s), grade, and suppliers are listed for each powder in Table 3.1. The particle sizes of commercially-

Table 1.1: Raw Material Characteristics

	Phases	Particle Size	Supplier
ZrB_2	ZrB_2	$d_{50} = 2.20 \ \mu m$	Grade B, H. C. Starck, GmbH
B_4C	stoichiometric B_4C	$d_{50} = 0.8 \ \mu m$	Grade HS, H. C. Starck, GmbH
SiC	α-SiC	$d_{50} = 0.88 \ \mu m$	Grade 8S490NDP, Superior Graphite, Chicago, IL
TaB_2	TaB_2, Ta_3B_4	$< 43 \ \mu m$	ESPI Metals, Ashland, OR
$TaSi_2$	$TaSi_2$	$< 43 \ \mu m$	Cerac Inc., Milwaukee, WI

available TaB_2 and $TaSi_2$ were deemed too large for pressureless sintering. Hence, sedimentation-based selection was used to obtain finer particles: Powders were dispersed in ethanol using an ultrasonicator (FS-14 Solid State Ultrasonicator, Fisher Laboratory Equipment Division, Pittsburgh, PA) for 10 min. The mixture was allowed to settle in ethanol for 1 h. The top 7 cm of fluid was then extracted using a pipette. Based on laser particle size analysis (Model LS 13 320, Beckman Coulter, Fullerton, CA), decanted particles had a d_{50} of 1.1 μm for TaB_2 and 1.7 μm for $TaSi_2$. The decanted suspensions were dried in a beaker on a hot-plate.

The compositions of synthesized powder mixtures are given in Table 2.2[1]. The powder mixtures were suspended in methanol, and mixed in a ball mill for 24 h, using B_4C as media. The milled powders were then dried in static air at 75°C. The powder mixtures were then ball milled again in water with dissolved polyvinyl alcohol (PVA, Celanese Ltd., Dallas, TX), polyethylene glycol (PEG, Alfa Aesar, Ward Hill, MA), and Darvan 821A (R.T. Vanderbilt Company Inc., Norwalk, CT), using B_4C as media for 8 h. PVA functioned as a binder with PEG functioning as a plasticizer, and Darvan 821A served as a dispersing agent. The highly viscous suspension after this milling step was dried in an oven at 75°C, and then sieved using a 60 mesh screen.

Approximately 400 mg of powder were uniaxially pressed into cylindrical pellets using a pressure of 117 MPa, holding for 1 min. The pellets were loaded into latex encapsulants which were in turn evacuated. These were cold isostatically pressed (CIP) at 345 MPa for 1 min. This was followed by a binder-removal heat treatment of 0.25°C/min to 500°C under vacuum (~4 Pa). Fifteen pellets were fabricated for each composition.

These pellets were fired in a graphite tube furnace (Model M11, Centorr Vacuum Industries Inc., Nashua, NH) under flowing argon, using graphite setters. The furnace was initially evacuated to ~4 Pa (roughing pump) and backfilled with argon. The typical heating schedule was 50°C/min to 2000°C, soaking for 1 h, and then cooling at 40°C/min to room temperature. The pellets were then hot isostatically pressed (HIP, American Isostatic Press, Columbus, OH) at 1800°C for 30 min under an argon gas pressure of 207 MPa. The densities of unfired pellets were determined from measured dimensions and mass; the densities

---

[1]Some compositions are indicated by two different codes. This was done to display compositional trends in logical groupings.

Table 1.2: Sample Compositions in Mole Percent

Code	ZrB_2	B_4C	SiC	TaB_2	$TaSi_2$
ZBS2	77.39	7.27	15.34	0	0
ZBS6	70.20	6.60	23.20	0	0
ZBS10	64.25	6.04	29.70	0	0
ZBS14	57.53	5.40	37.06	0	0
ZBS18	50.78	4.78	44.45	0	0
ZBS22	43.80	4.12	52.08	0	0
ZBS26	37.55	3.53	58.92	0	0
ZBSTB1	63.14	5.62	27.91	3.32	0
ZBSTB2	59.82	5.62	27.91	6.65	0
ZBSTB3	56.49	5.62	27.91	9.97	0
ZBSTB4	53.17	5.62	27.91	13.29	0
ZBSTB5	49.85	5.62	27.91	16.61	0
ZBSTS1	63.14	5.62	27.91	0	3.32
ZBSTS2	58.82	5.62	27.91	0	6.65
ZBSTS3	56.49	5.62	27.91	0	9.97
ZBSTS4	53.17	5.62	27.91	0	13.29
ZTBS1-1	59.82	5.62	27.91	6.65	0
ZTBS1-5	59.82	5.62	27.91	3.32	3.32
ZTBS1-9	58.82	5.62	27.91	0	6.65
ZTBS2-1	53.17	5.62	27.91	13.29	0
ZTBS2-5	53.17	5.62	27.91	6.65	6.65
ZTBS2-9	53.17	5.62	27.91	0	13.29

of pressureless sintered and post-HIPed pellets were determined using Archimedes' method. All specimens were 100% dense based on theoretical densities calculated from the rule of mixtures.

All of the surfaces of all post-HIPed samples were ground away using 320 grit SiC grinding paper (Buehler, Lake Bluff, IL), and the resulting pellet dimensions were measured with calipers. The oxidation behaviors were then investigated using thermogravimetric analysis (TG, Model STA 409, Netzsch, Exton, PA, with an Innovative Thermal Systems interface, Atlanta, GA). The samples were supported on alumina chips which filled an alumina crucible, to minimize the contact between sample surfaces and alumina. Samples were exposed to flowing air from a compressed air tank with a flow rate of 0.1 liter/min. Flow rate was maintained via a mass flow controller (Model GFC 17, Aalborg, Orangeburg, NY). Specimens were heated to soak temperatures of 1200, 1400, or 1500°C and held for 4 h. For the 1200°C soak, specimens were heated at 50°C/min to 950°C, 30°C/min to 1100°C, 10°C/min to 1170°C and 5°C/min to the soak temperature. For the 1400°C soak, specimens were heated at 50°C/min to 1150°C, 30°C/min to 1300°C, 10°C/min to 1370°C, and 5°C/min to the soak temperature. For the 1500°C soak, specimens were heated at 50°C/min to 1250°C, 30°C/min to 1400°C, 10°C/min to 1470°C, and 5°C/min to 1500°C. Displayed data is truncated to the start of the soak temperature. To evaluate repeatability, 3-4 TG oxidation heat-treatments were performed on each composition. Displayed traces are those considered most representative.

Crystalline phases in the samples were identified using X-ray diffraction (XRD, Model X'Pert PRO Alpha-1, PANalytical, Netherlands). Scans were recorded at room temperature

over a 2θ range of 10-80° at a scan rate of 0.01°/s. Prior to oxidation heat-treatment, specimen surfaces were ground to expose specimen interior regions for XRD analysis. XRD of oxidized specimens were taken from unaltered surfaces. Microstructures of oxidized samples were investigated using scanning electron microscopy (SEM, LEO 1530, Carl Zeiss SMT, Inc., Thornwood, NY) and energy dispersive spectrometry (EDS, Oxford Pentafet detector with ultrathin window, Oxford Instruments, Oxfordshire, UK). Specimen cross-sections were formed via impact-formed fracture surfaces, with the oxidized surfaces mounted on the SEM stub to be parallel with the beam axis. Specimens were coated with gold (sputtering for 2 min) to form a conductive surface.

Thin sections of specimen cross-sections were prepared by using a focused ion beam milling system (Nova Nanolab 200 FIB/SEM system, FEI Corp., Hillsboro, OR). Approximately 2 μm of Pt was deposited on the top of the samples to avoid ion beam damage. The samples were milled through the specimen cross section using a gallium ion beam at 30 kV, 30 pA to 20 nA, until specimen thicknesses reached ~100 nm. These specimens were analyzed for microstructure on a JEOL 4000EX 400kV high resolution transmission electron microscope (TEM, JEOL USA, Peabody, MA) with a point-to-point resolution of 0.18 nm, and a Hitachi HF-2000 200 kV field emission gun TEM (Hitachi High Technologies America, Inc., Pleasanton, CA) with EDS capabilities (Noran detector with ultrathin window, for detection of elements down to boron, Thermo Scientific, Madison, WI). Specimens evaluated by XRD, SEM, and TEM were surface-oxidized in the TG as previously described.

III   Results

Phases identified in as-fabricated specimen interiors, as well as phases identified from surfaces after oxidation heat-treatments are listed in Table 1.3. For the as-fabricated specimens, the boron carbide additive was not detected. TaB_2 formed a solid solution with ZrB_2 as evidenced by distinct shifts in the 2θ values of the ZrB_2 peaks. This also occurred with $TaSi_2$ additions.

Figure 1.1 shows the microstructures of fracture surfaces of densified ZBS samples of two different SiC concentrations. The darker phase is SiC, and the ligher is ZrB_2, as would be expected based on atomic weights, and as implied by the EDS spectra of marked regions. SiC appeared as a continuous phase in the specimen with 52.1 mol% SiC, and as an isolated phase in the specimen with 15.3 mol% SiC. The occasional round darkest regions (e.g. region B in the upper micrograph) are interpreted to be B_4C, based on comparisons of EDS spectra and the dark shading consistent with light elements. In general, boron has not been reliably detected using the available EDS detector.

After oxidation heat-treatments of the ZBS series, zirconia in its stable monoclinic form was sometimes detected by XRD (orthorhombic zirconia was detected in trace quantities at 1500°C). SiC and ZrB_2 were also detected for some of the higher SiC-containing samples. For the various series containing TaB_2 and/or $TaSi_2$, TaC was detected (on occasion, trace quantities of ZrC were also detected). TaB_2 additions resulted in no apparent shifting in ZrO_2 2θ peak positions, nor were there noticeable increases in peak intensity of orthorhombic-ZrO_2.

Figure 1.2 shows TG traces of the ZBS series at three different soaking temperatures. Mass increases after the 4 h soaks were less extensive with increasing SiC content. The rates of weight gain were decreasing with time, with the exception of low concentrations of SiC (i.e. < 27.9 mol% SiC) at 1200°C.

Table 1.3: Phases Identified via XRD of As-synthesized and Oxidized Specimens at Indicated Temperatures ("ss" indicates solid solution, "tr" indicates trace quantities, M and O indicate the monoclinic and orthorhombic forms of zirconia, respectively.)

| Code	As-Fabricated	1200°C	1400°C	1500°C
ZBS2	ZrB_2	M-ZrO_2	M-ZrO_2	M-ZrO_2
ZBS6	ZrB_2	M,O-ZrO_2	M-ZrO_2	M,O-ZrO_2
ZBS10	ZrB_2, $SiC_{(tr)}$	M-ZrO_2	M-ZrO_2, SiC	M,O-ZrO_2
ZBS14	ZrB_2, SiC	M-ZrO_2, SiC	M-ZrO_2, SiC	M-ZrO_2
ZBS18	ZrB_2, SiC	M-ZrO_2, SiC, ZrB_2	M-ZrO_2, SiC, ZrB_2	M-ZrO_2, SiC, ZrB_2
ZBS22	ZrB_2, SiC	M-ZrO_2, SiC, ZrB_2	M-ZrO_2, SiC, ZrB_2	M-ZrO_2, SiC, ZrB_2
ZBS26	ZrB_2, SiC	M-ZrO_2, SiC	M-ZrO_2, SiC	M-ZrO_2, SiC, ZrB_2
ZBSTB1	ZrB_2-$TaB_{2(ss)}$, SiC	M,O-ZrO_2, TaC	M-ZrO_2, TaC	M,O-ZrO_2, TaC
ZBSTB2	ZrB_2-$TaB_{2(ss)}$ SiC	M,O-ZrO_2, TaC	M-ZrO_2, TaC	M,O-ZrO_2, TaC
ZBSTB3	ZrB_2-$TaB_{2(ss)}$, SiC	M,O-ZrO_2, TaC	M,O-ZrO_2, TaC	M,O-ZrO_2, TaC
ZBSTB4	ZrB_2-$TaB_{2(ss)}$, SiC	M-ZrO_2, TaC, SiC, $ZrC_{(tr)}$	M,O-ZrO_2, TaC, TaB_2	M,O-ZrO_2, TaC, TaB_2
ZBSTB5	ZrB_2-$TaB_{2(ss)}$, SiC	M,O-ZrO_2, TaC, $TaZr_{2.75}O_8$	M,O-ZrO_2, TaC, TaB_2	M,O-ZrO_2, TaC
ZBSTS1	ZrB_2-$TaB_{2(ss)}$, SiC	M-ZrO_2, TaC $ZrC_{(tr)}$	M,O-ZrO_2, TaC	M,O-ZrO_2 TaC
ZBSTS2	ZrB_2-$TaB_{2(ss)}$, SiC	M,O-ZrO_2 TaC	M,O-ZrO_2, TaC, SiC, ZrB_2-$TaB_{2(ss)}$	M,O-ZrO_2, TaC, ZrB_2-$TaB_{2(ss)}$
ZBSTS3	ZrB_2-$TaB_{2(ss)}$, SiC	M,O-ZrO_2, TaC ZrB_2-$TaB_{2(ss)}$, $ZrC_{(tr)}$	M-ZrO_2, TaC, ZrB_2-$TaB_{2(ss)}$, $ZrC_{(tr)}$	M,O-ZrO_2, TaC ZrB_2-$TaB_{2(ss)}$
ZBSTS4	ZrB_2-$TaB_{2(ss)}$, SiC	M,O-ZrO_2, TaC, ZrB_2-$TaB_{2(ss)}$, $ZrC_{(tr)}$	M-ZrO_2, TaC, TaB_2, $ZrC_{(tr)}$	M,O-ZrO_2, TaC, TaB_2
ZTBS1-1	ZrB_2-$TaB_{2(ss)}$, SiC	M,O-ZrO_2, TaC	M-ZrO_2, TaC	M,O-ZrO_2, TaC
ZTBS1-5	ZrB_2-$TaB_{2(ss)}$, SiC, $TaSi_{2(tr)}$	M-ZrO_2, TaC, TaB_2	M-ZrO_2, TaC, SiC, ZrB_2-$TaB_{2(ss)}$	M-ZrO_2, TaC, ZrB_2-$TaB_{2(ss)}$
ZTBS1-9	ZrB_2-$TaB_{2(ss)}$, SiC	M,O-ZrO_2, TaC	M,O-ZrO_2, TaC, SiC, ZrB_2-$TaB_{2(ss)}$	M,O-ZrO_2, TaC
ZTBS2-1	ZrB_2-$TaB_{2(ss)}$, SiC	M-ZrO_2, TaC, SiC, $ZrC_{(tr)}$	M,O-ZrO_2, TaC, TaB_2	M,O-ZrO_2, TaB_2, TaC
ZTBS2-5	ZrB_2-$TaB_{2(ss)}$, SiC	M-ZrO_2, TaC, TaB_2	M-ZrO_2, TaC, TaB_2, $ZrC_{(tr)}$	M,O-ZrO_2, TaC, TaB_2
ZTBS2-9	ZrB_2-$TaB_{2(ss)}$, SiC	M,O-ZrO_2, TaC, ZrB_2-$TaB_{2(ss)}$, $ZrC_{(tr)}$	M-ZrO_2, TaC, TaB_2, $ZrC_{(tr)}$	M,O-ZrO_2, TaC, TaB_2
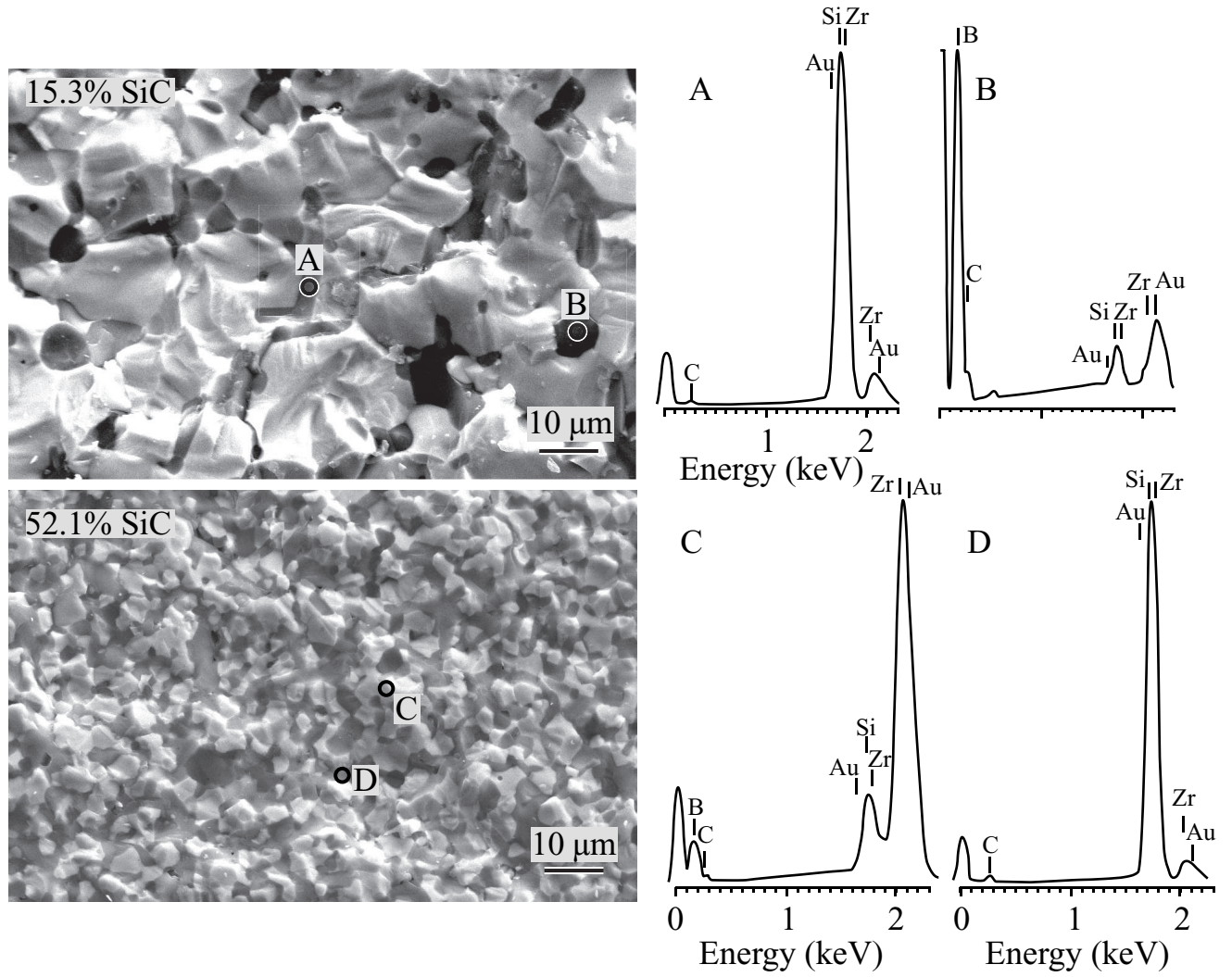
Figure 1.1: Microstructures of fracture surfaces of two ZBS compositions. EDS data and compositional contrast imply dark round regions are B_4C, slightly lighter-shaded, sometimes elongated, grains are SiC, and light-shaded regions are ZrB_2.
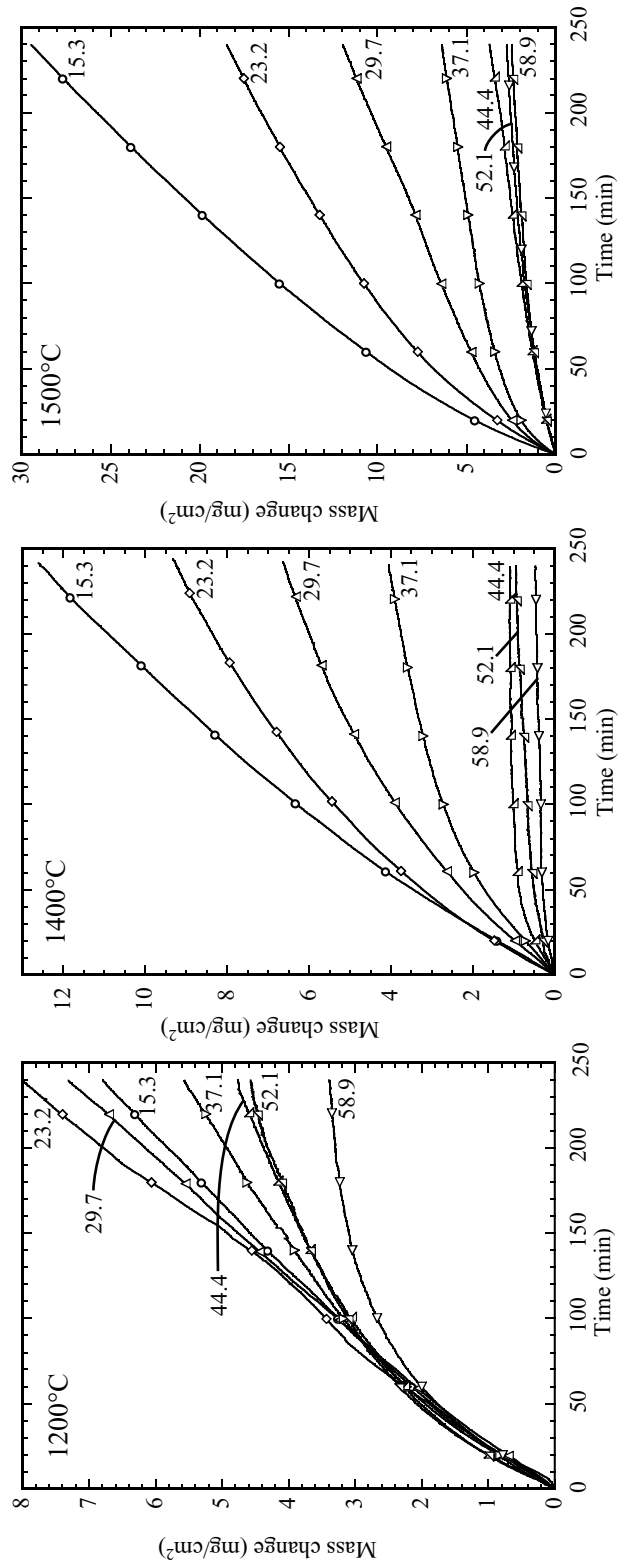
Figure 1.2: TG of ZrB_2-B_4C specimens with varying amounts of SiC (ZBS series), soaked at three different temperatures. Numbers in the plots indicate SiC content in mole percent. Data sets consist of approximately 2000 data points; the symbols on the traces are for curve identification purposes. This is the case for all TG traces in this paper.

11

Figure 1.3 shows the cross-section microstructures of ZBS specimens with varying SiC concentrations, in which a glassy surface coating is seen covering an oxide underlayer. Based on comparisons of EDS spectra, microstructure morphology, and XRD results, the oxide underlayer is interpreted to be zirconia particles surrounded by porosity and some remnant borosilicate glass. For the 1500°C heat-treatment, both the glassy and oxide underlayer thicknesses decreased with increasing SiC concentration. EDS patterns show zirconium along with silicon in the glassy surface layer for the specimen with 15.3 mol% SiC, but only silicon in the glassy layer for the specimen with 29.7 mol% SiC.

Glassy surface layer and oxide underlayer thicknesses as a function of soak temperature and SiC concentration, based on measurements on SEM micrographs, are depicted in Figure 1.4a. Figure 1.4b summarizes the weight gains (based on weight losses after 4 h soaks determined from Figure 1.2) as a function of SiC concentration and soak temperatures.

Figure 1.5 shows TG traces of the ZBSTB series (varying TaB_2 concentrations). For specimens soaked at 1200°C, higher TaB_2 concentrations resulted in increased oxidation resistance, while for soaks at 1500°C, increasing TaB_2 concentrations showed diminishing oxidation resistance. Weight change was low (lower than many compositions soaked at 1200°C), and relatively unchanged with composition, for specimens soaked at 1400°C. Higher (13.29 and 16.61 mol%) concentrations of TaB_2 resulted in marked points of acceleration in mass increase during oxidation at 1500°C (at ~60 min for 16.61 mol% TaB_2, and at ~120 min for 13.29 mol% TaB_2).

Figure 1.6 shows glassy surface layers and oxide underlayers covering un-reacted non-oxide phases for ZBSTB5. EDS spectra show Si, Zr, and Ta in the oxide underlayer. No tantalum was confirmed by EDS in the glassy layer. Figure 1.7 shows a TEM micrograph of the amorphous surface layer with a rectangularly-shaped zirconia crystal; such crystals were observed occasionally in TEM analysis of the glassy surface layer. No tantalum is indicated in the glass, though major Ta peaks overlap with Si and Cu, which may mask small concentrations. There was no evidence of phase separation in the glass. As shown in Figure 1.8, the oxide underlayer consists of zirconia and TaC (dark round) particles which are incompletely coated by a glassy phase. The TaC crystals were ~50 nm—substantially smaller than the ZrO_2 crystals. The glassy phase shows very faint evidence of tantalum, while the zirconia crystals show slightly better evidence of tantalum. Figure 1.9a displays glassy surface layer and oxide underlayer thicknesses, while Figure 1.9b summarizes weight changes for the ZBSTB series.

Figure 1.10 shows TG traces of the ZBSTS specimens (varying $TaSi_2$ content). Figure 1.11a shows the glassy and oxide layer thicknesses for these compositions, and Figure 1.11b summarizes the oxidation weight gain measurements. Oxide underlayer thicknesses decreased with initial increases in $TaSi_2$ content. Glassy layer thicknesses were relatively constant at 1400 and 1500°C; at 1200°C, the layer did not form for $TaSi_2$ contents less than 6.65 mol%. As with TaB_2 additions, the effects of $TaSi_2$ on oxidation resistance reversed at 1500°C; $TaSi_2$ additions above 3.32 mol% resulted in a decreased oxidation resistance, though not nearly as extensive as observed with increasing TaB_2. Figure 1.12 shows the effect of substitution of $TaSi_2$ for TaB_2 (ZTBS series). For these compositions, $TaSi_2$ is shown to be a more effective additive for oxidation resistance than equimolar additions of TaB_2.

The appearances of the oxide underlayers in the ZBS10 (no tantalum additive), ZBSTB5 (TaB_2 added), and ZBSTS4 ($TaSi_2$ added) series are compared in Figure 1.13 for the 1400°C heat-treatment, and Figure 1.14 for the 1500°C heat-treatment. Zirconia particles were
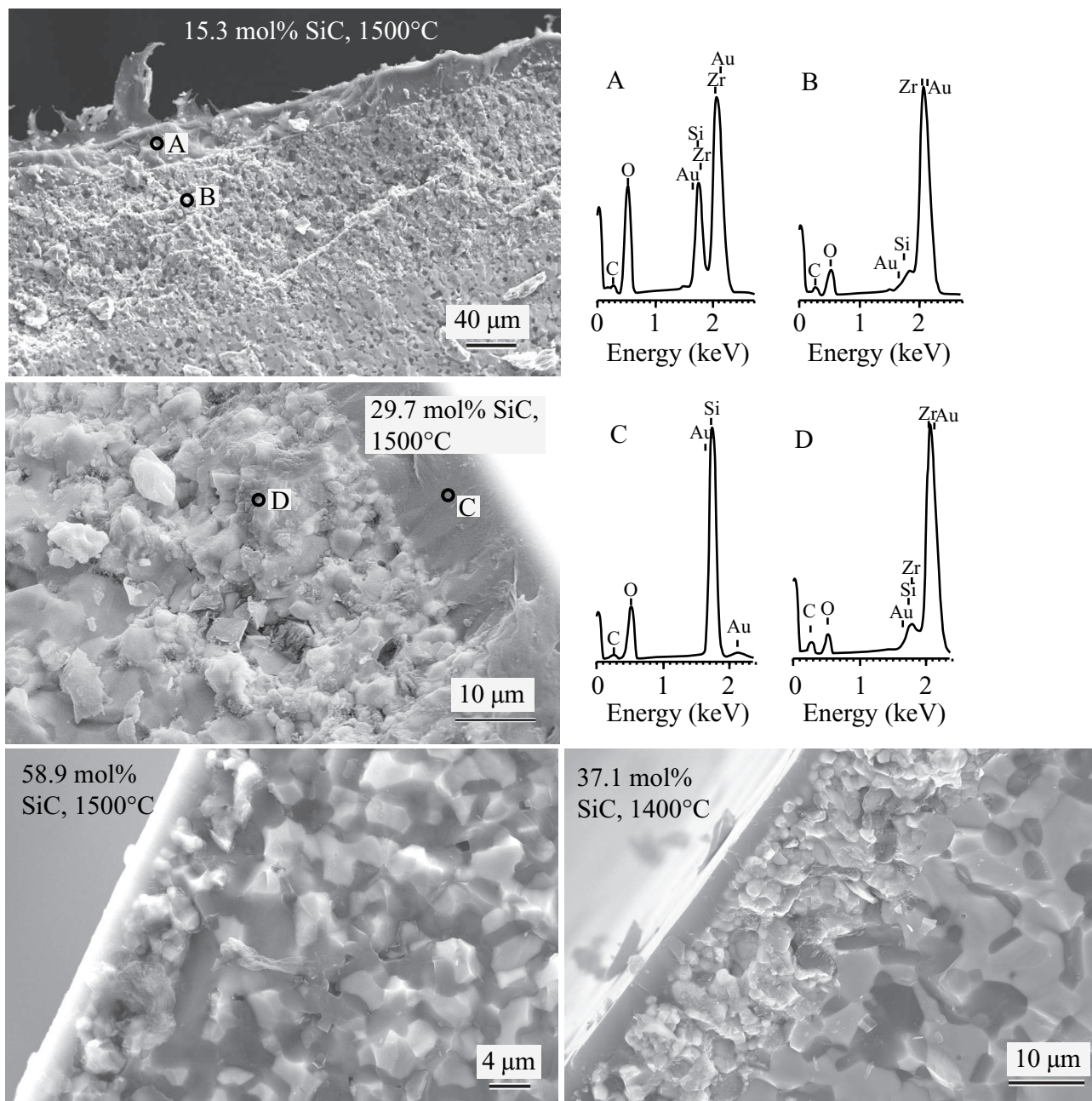
Figure 1.3: Cross-section microstructures of ZBS series samples with varying concentrations of SiC, oxidized in flowing air at the indicated temperatures. Energy dispersive spectroscopy spectra corresponds to the marked regions in the microstructures. EDS peaks identified as gold correspond to conductive coatings applied to specimen surfaces.
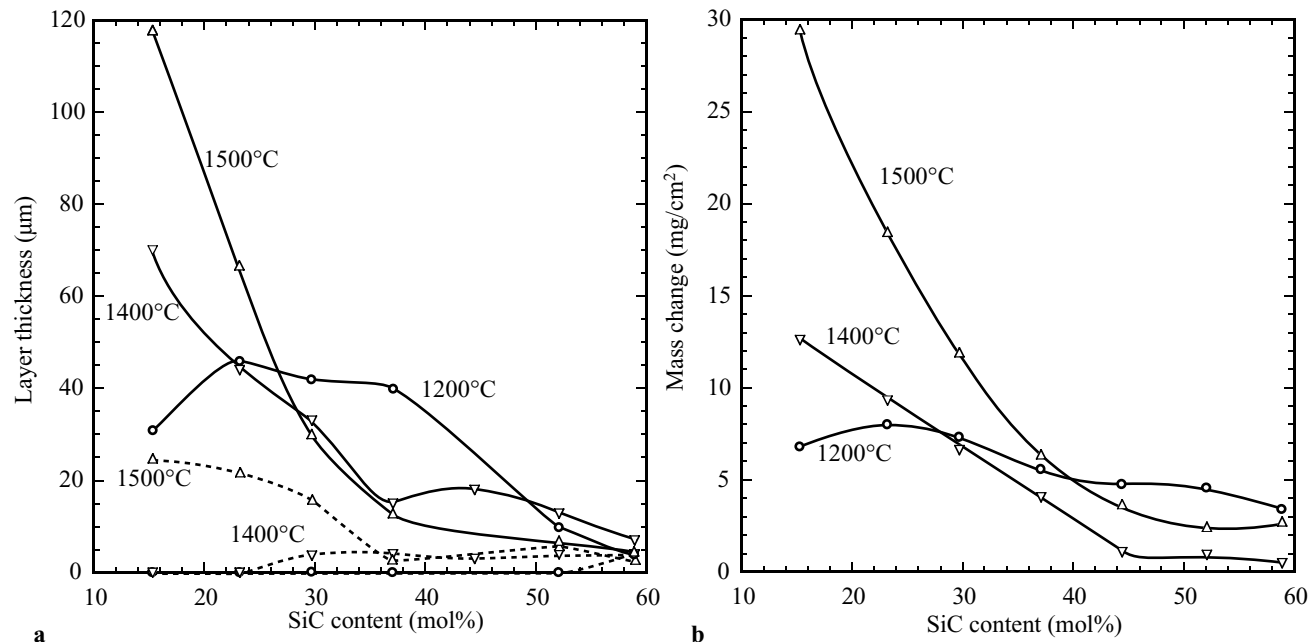
Figure 1.4: Effects of oxidation heat-treatments (in the TG) for ZBS compositions of varying SiC content. a) Layer thicknesses estimated from SEM micrographs of specimen cross-sections. Solid lines indicate the thicknesses of the oxide underlayers. Dashed lines indicate the thicknesses of the glassy layers adjacent to the surfaces. Temperatures marked in the figure refer to the isothermal soak temperatures. b) Mass changes after soaking at the indicated temperatures for 4 h in the TG.
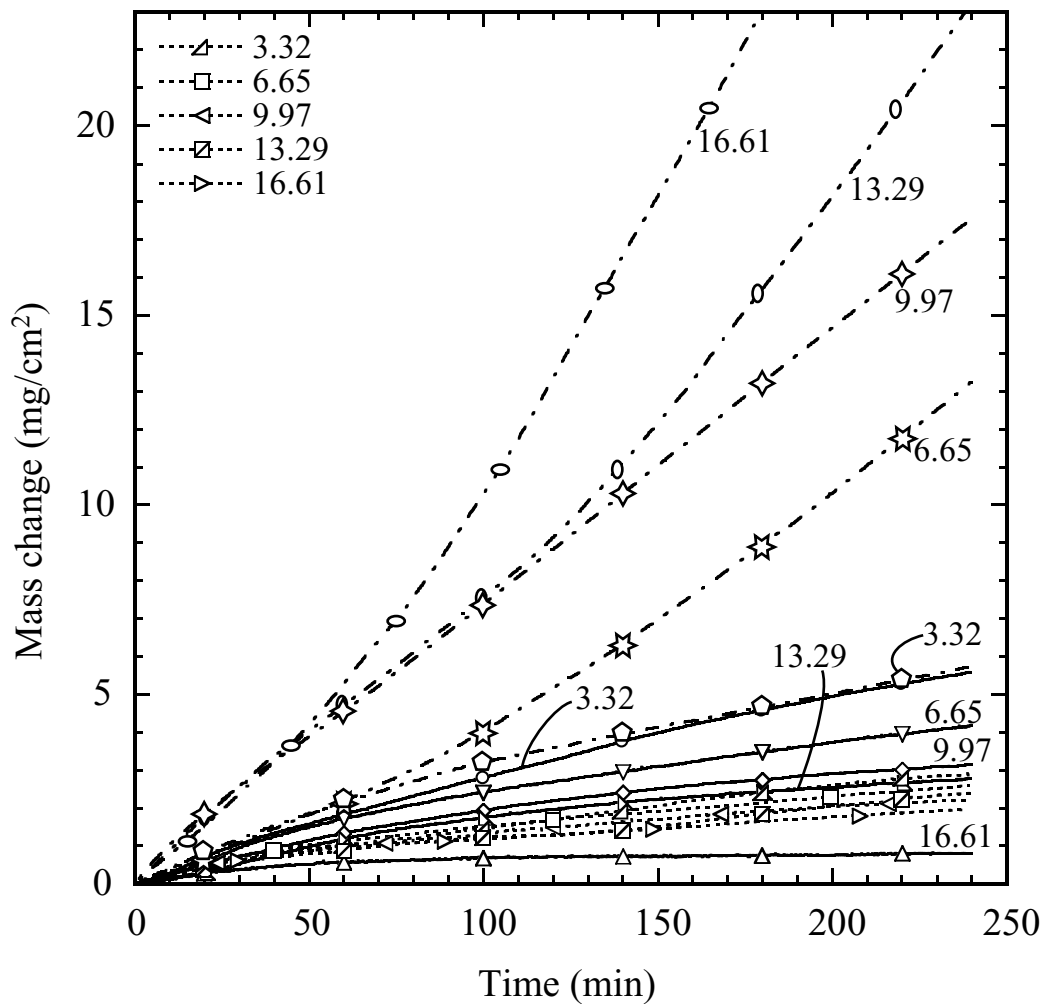
Figure 1.5: Isothermal TG traces of ZrB_2-B_4C-SiC specimens containing varying amounts of TaB_2 (ZBSTB series). Solid curves correspond to 1200°C heat-treatments, dashed curves correspond to 1400°C heat-treatments, and dot-dashed curves correspond to 1500°C heat-treatments. Numbers in the figure indicate mol% of TaB_2.
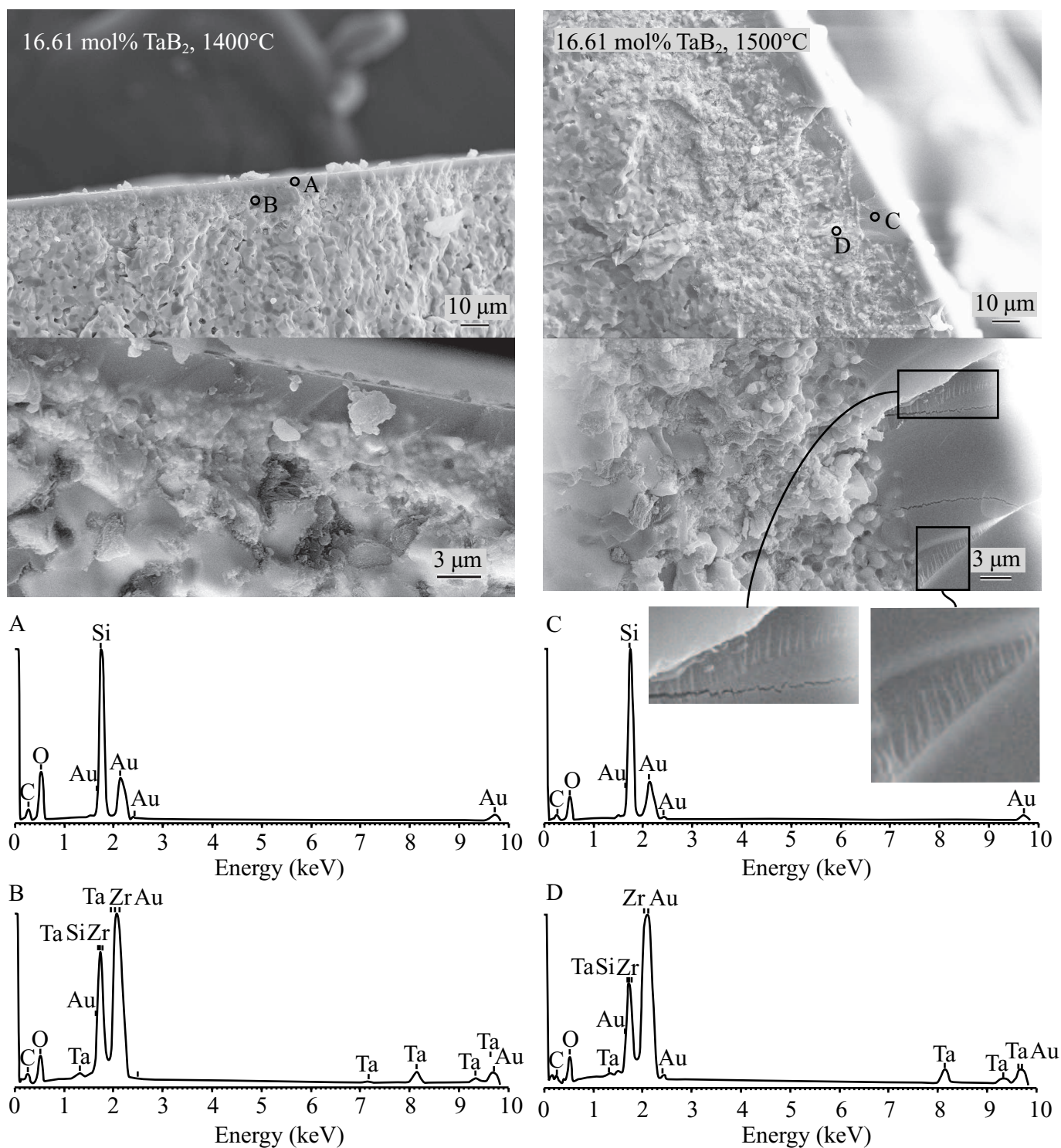
Figure 1.6: Cross-section microstructures and selected EDS spectra of ZBSTB5 for two soak temperatures. Although tantalum was clearly detected by EDS in the oxide underlayers, its complete absence in the glassy layer cannot be confirmed because of EDS peak overlap with other elements.
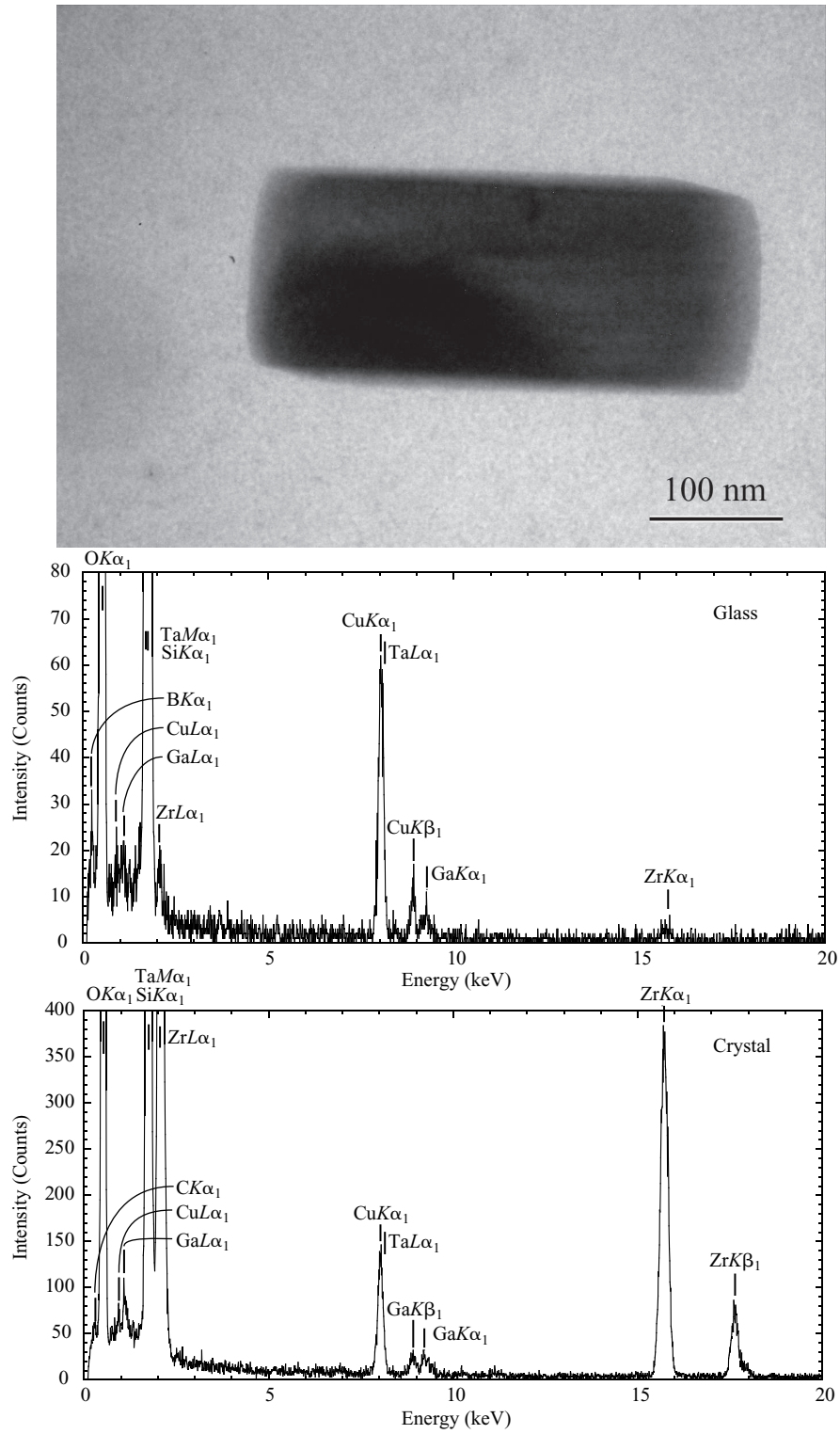
Figure 1.7: TEM micrograph of the amorphous surface layer of ZBSTB5 heat treated at 1500°C, along with EDS spectra of selected regions. Copper EDS peaks correspond to the copper grid upon which the specimen was mounted, and gallium peaks correspond to embedded gallium FIB gas milling atoms.

17
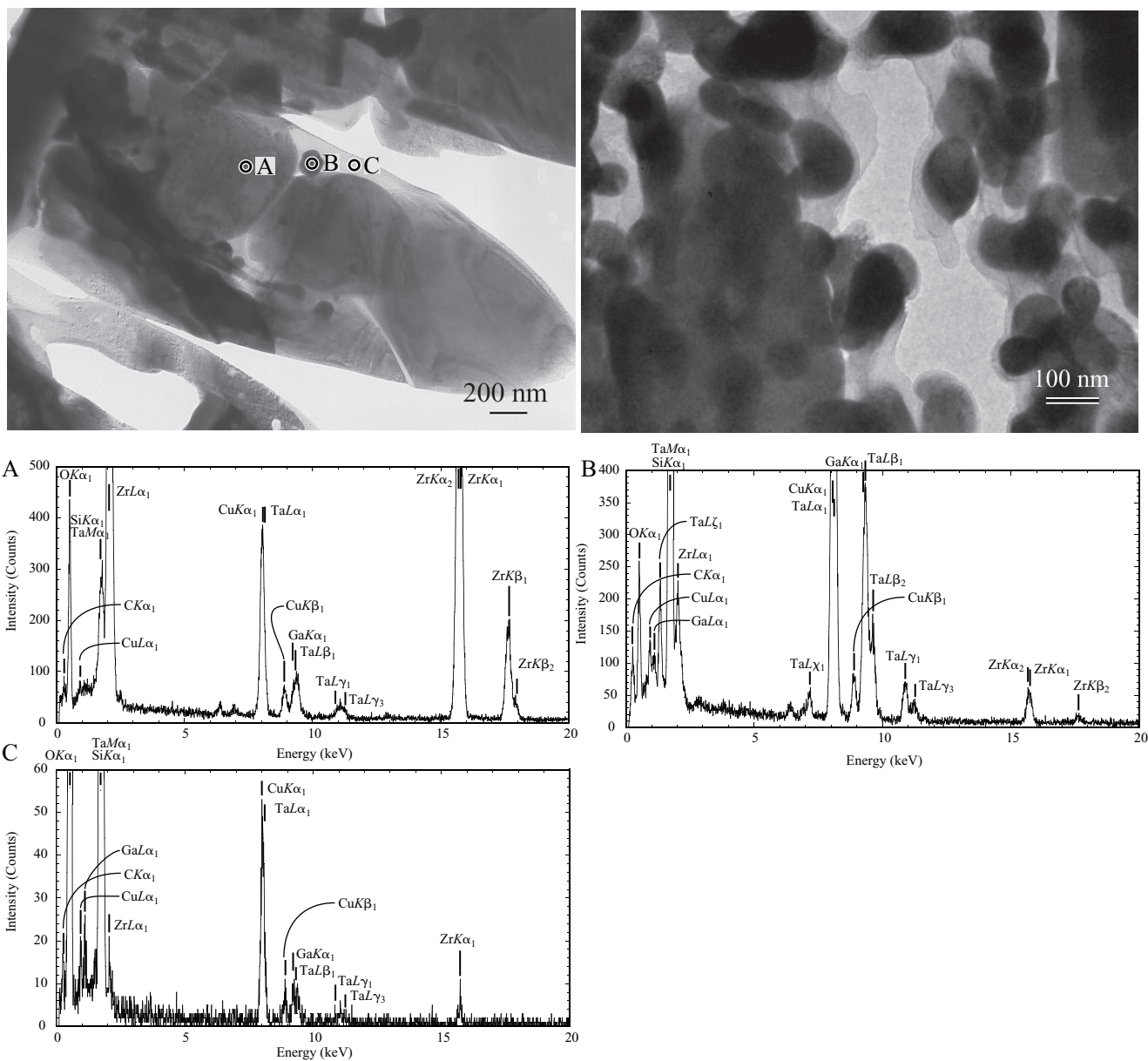
Figure 1.8: TEM micrographs of the oxide underlayer of ZBSTB5 (16.61 mol% TaB$_2$) heat-treated at 1500°C, along with EDS spectra of selected regions.
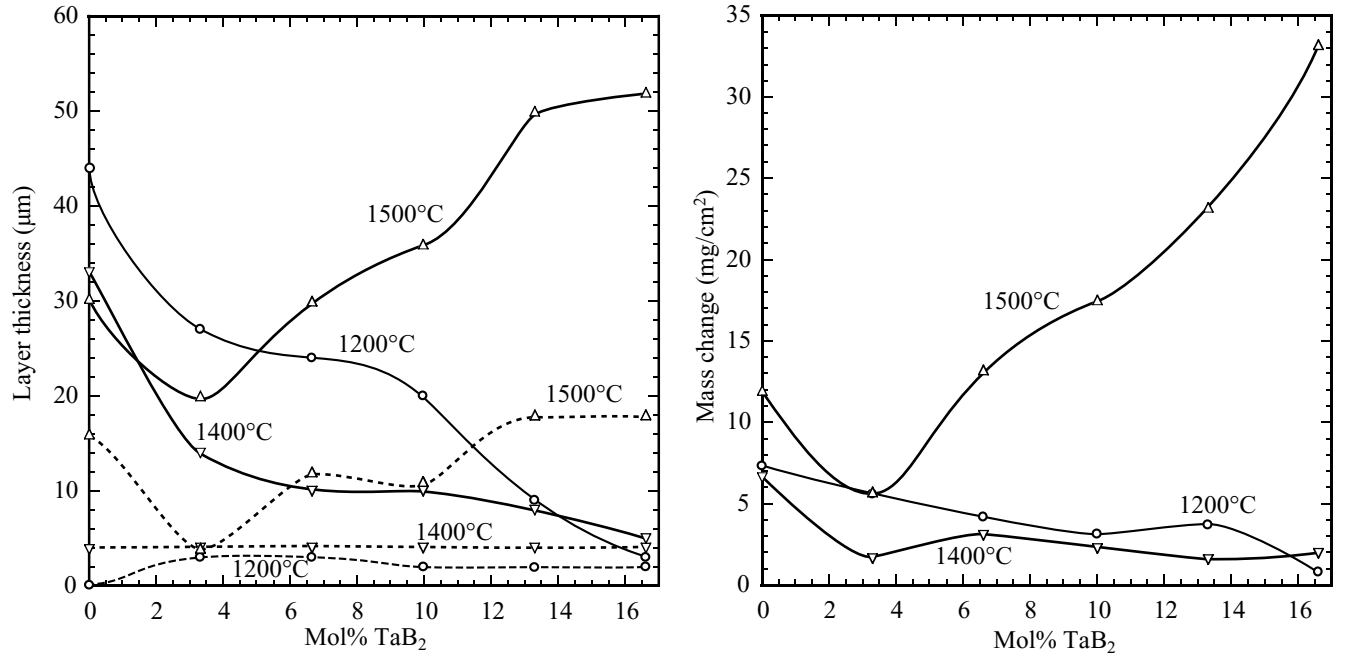
Figure 1.9: Effects of heat treatment in the TG in flowing air for compositions of ZrB_2-B_4C-SiC, with varying concentrations of TaB_2 (ZBSTB series). a) Oxide underlayer thicknesses were estimated from SEM micrographs of specimen cross-section fracture surfaces. Solid and dashed lines, and indicated temperatures, have the same meaning as Figure 1.4. b) Mass change after soaking at the indicated temperatures for 4 h in the TG. Values corresponding to 0 mol% TaB_2 were from sample ZBS10.
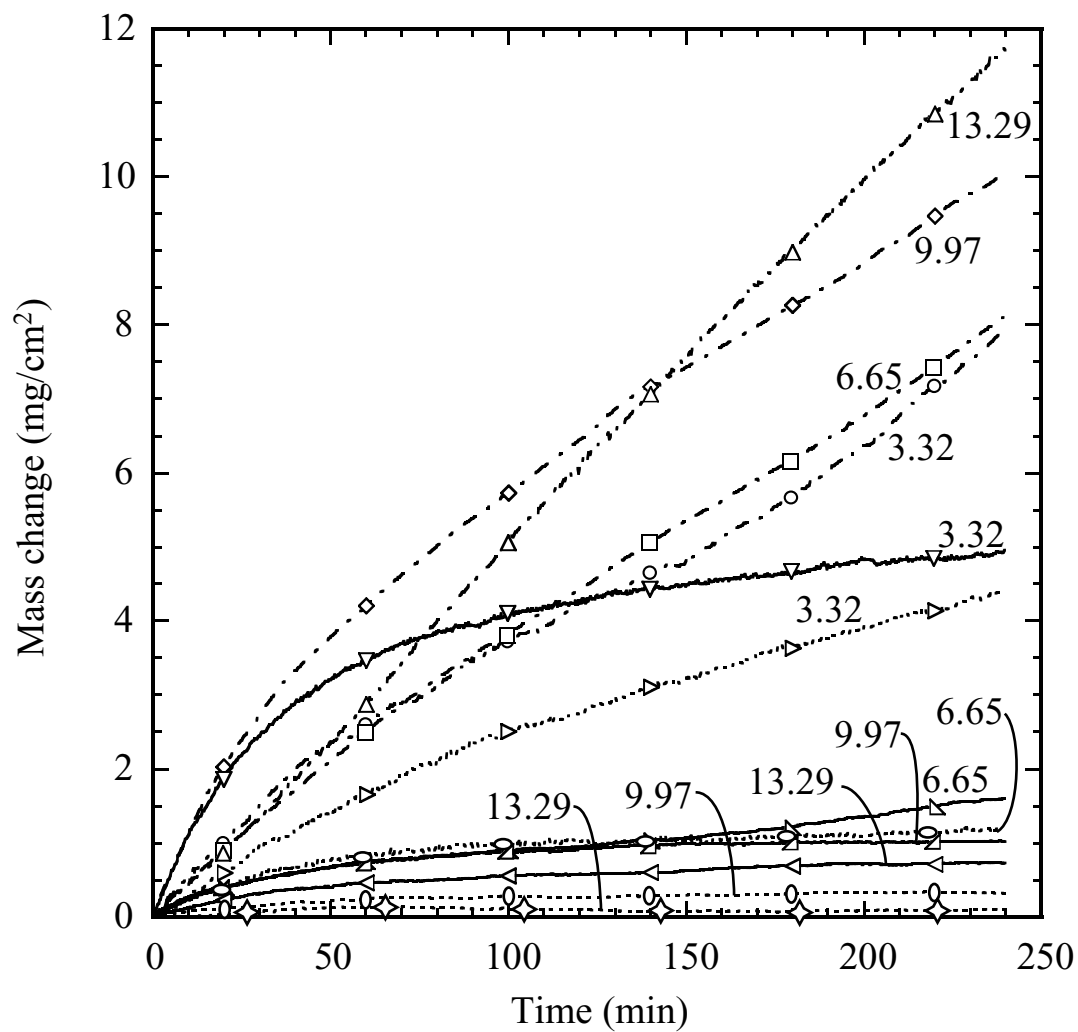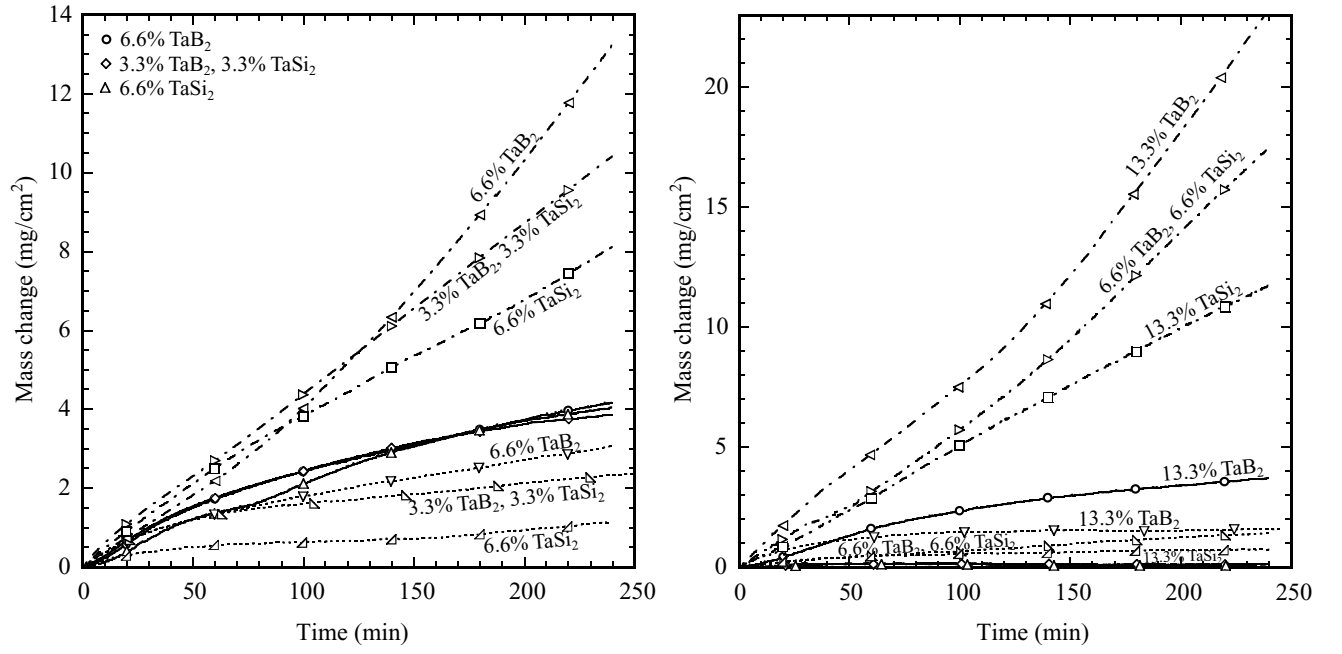
Figure 1.10: TG traces of specimens of varying TaSi$_2$ content oxidized in air at three different temperatures. Dashed curves are 1200°C, solid curves are 1400°C, and dot-dashed curves are 1500°C.
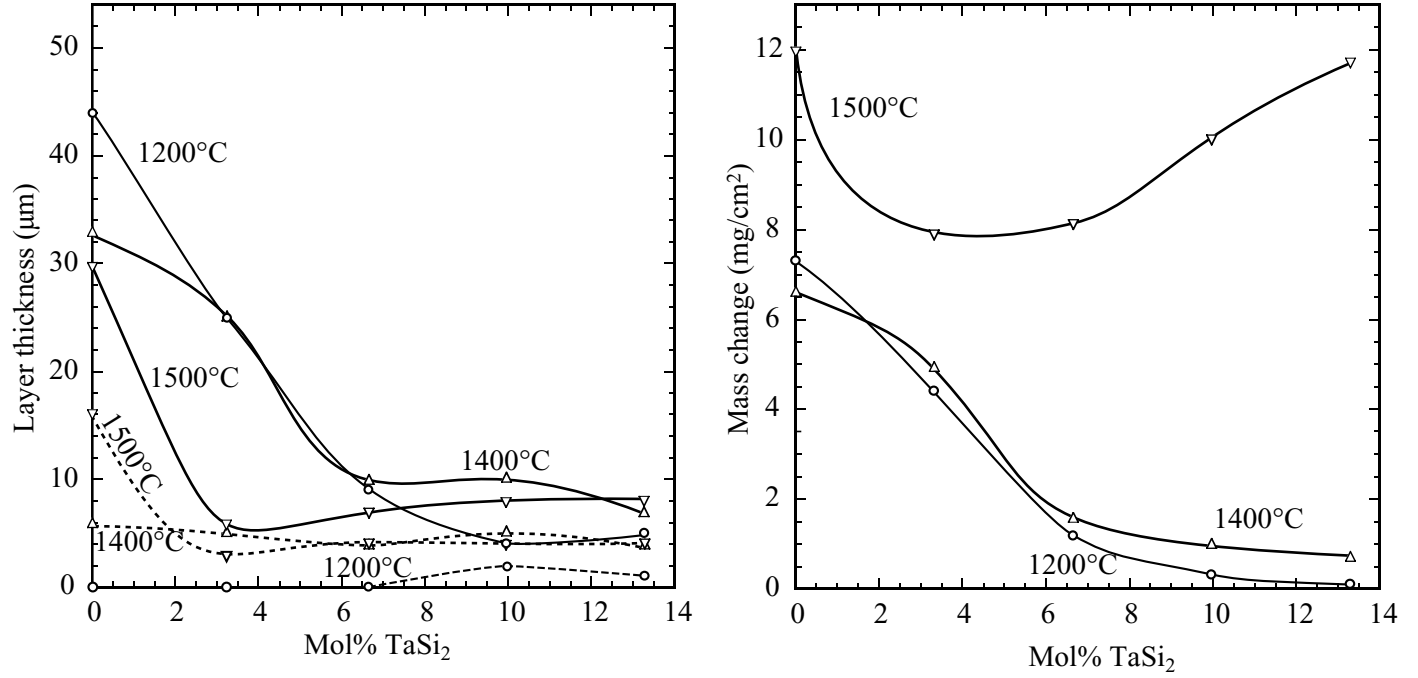
Figure 1.11: Effects of heat treatment in the TG under flowing air for ZrB_2-B_4C-SiC with varying concentrations of $TaSi_2$ (ZBSTS series). a) Oxide layer thicknesses estimated from SEM micrographs of specimen fracture surface cross-sections. Solid and dashed lines, and indicated temperatures have the same meaning as Figure 1.4. b) Mass changes after soaking at the indicated temperatures for 4 h in the TG. Values corresponding to 0 mol% $TaSi_2$ were from sample ZBS10.

Figure 1.12: TG traces of specimens of varying $TaB_2/TaSi_2$ ratio (ZTBS series) oxidized in air at three different temperatures. Dashed curves are $1200°C$, solid curves are $1400°C$, and dot-dashed curves are $1500°C$.
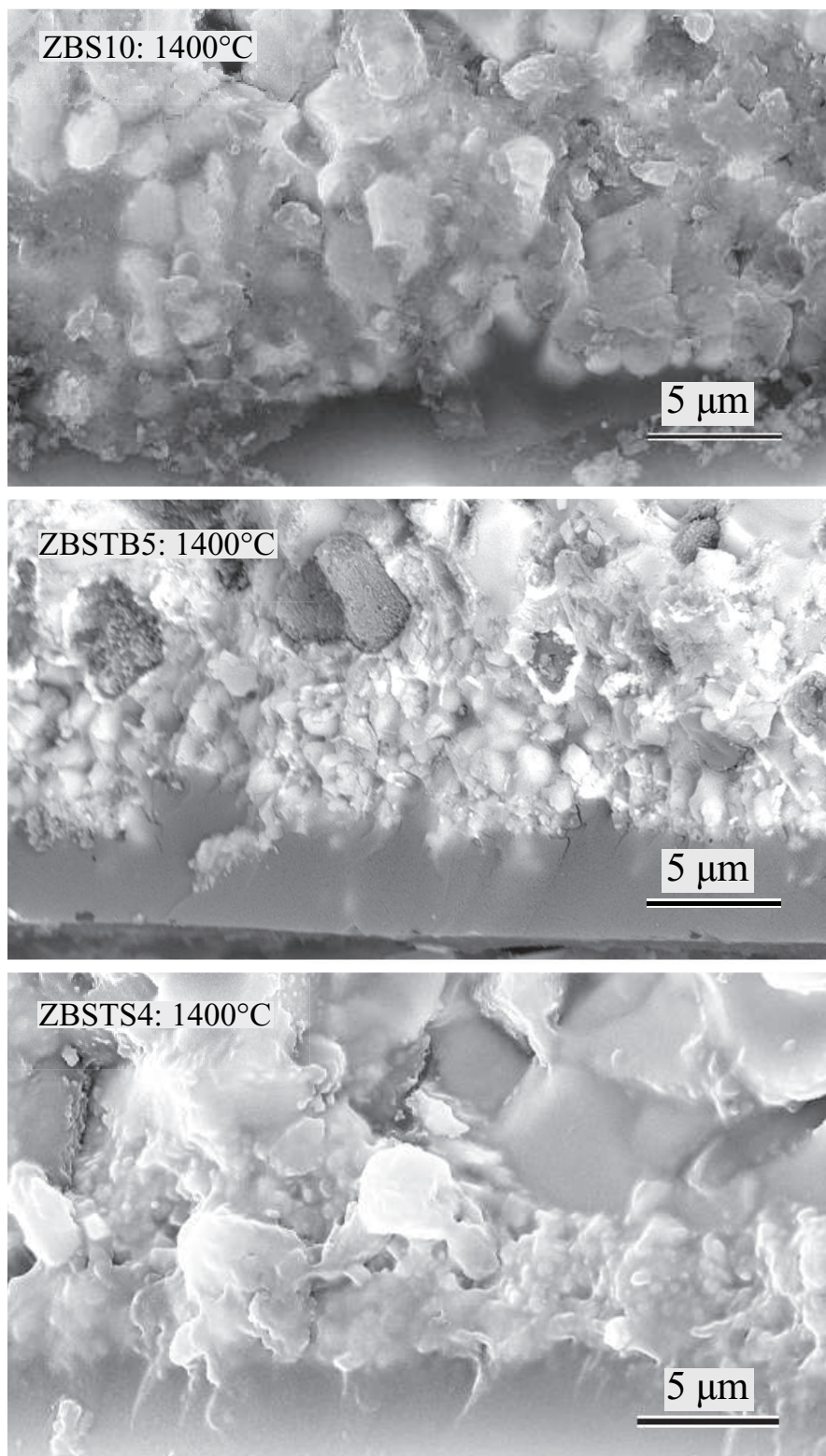
Figure 1.13: Comparison of oxide underlayers at the same magnification for ZBS10, ZBSTB5, and ZBSTS4, oxidized at 1400°C.
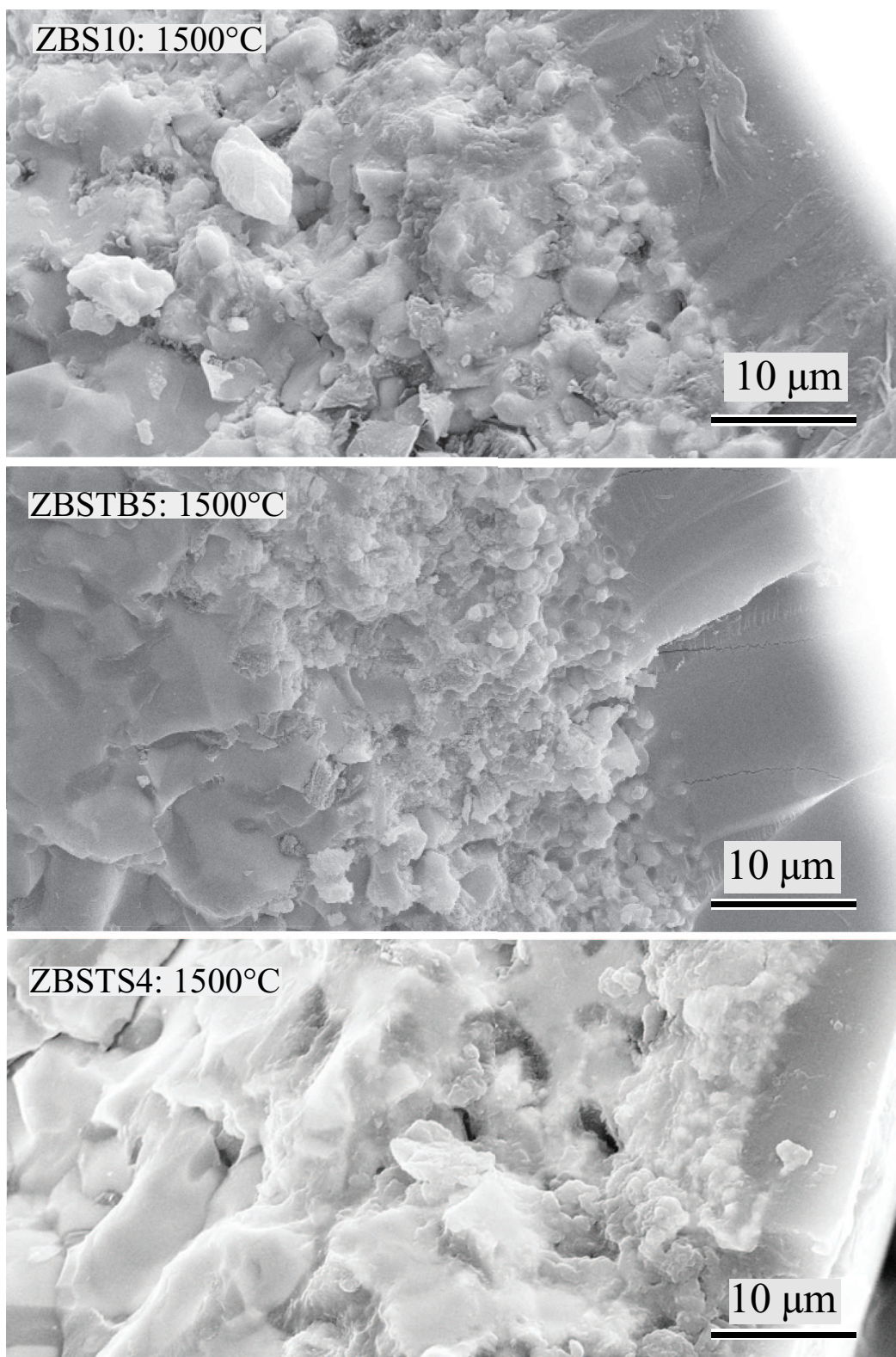
Figure 1.14: Comparison of oxide underlayers at the same magnification for ZBS10, ZBSTB5, and ZBSTS4, oxidized at 1500°C.

substantially smaller in the specimens containing TaB_2 or $TaSi_2$ additions. A relatively substantial amount of glassy phase was seen interdispersed in the oxide underlayer in samples containing $TaSi_2$ as a batch additive.

IV   Discussion

In the ZBS series, ZrB_2 and SiC form distinct phases (Table 1.3 and Figure 1.1). While B_4C was not detected by XRD, its presence as a distinct phase is implied by SEM/EDS. TG traces (Figure 1.2) of these compositions at 1400 and 1500°C show a decreasing weight change slope with time, indicative of the buildup of a barrier coating against the diffusion of reactant and product gases. At 1200°C, this was not observed for low SiC concentrations ($\leq$ 15.3 mol% SiC, Figure 1.2), indicating that such a barrier layer was not forming. As implied from Figure 1.4, a visibly distinct silica-rich liquid/glassy surface layer was not necessary for a decelerating oxidation rate; a decreasing mass change slope with time was observed for the ZBS specimen with 37.1 mol% SiC, but a glassy layer was first observed for the ZBS specimen with 52.1 mol% SiC. The formation of enough silica to seal around zirconia particles near the surface would function as a diffusion barrier, even if a visually-distinct amorphous surface layer is not visible.

SiC concentrations in the ZBS series at and above 44.4 mol% are impressively effective at forming a thin passivating layer. Under rapid impact with the atmosphere, as would be seen in a leading-edge aerospace application, such a high concentration of SiC may result in a liquid/glassy layer which may rapidly ablate away. In contrast, a lower concentration of SiC might be expected to form an amorphous surface layer with anchored zirconia crystalline phases interdispersed, providing protection against the silica being convected away by a high velocity gas stream. This assumes that the dominant mechanism of glassy phase removal is not vaporization from frictional heating.

An interesting result from the specimens oxidized at 1500°C is that the silica layer thickness decreased, and oxidation resistance increased, with increasing SiC content. For compositions of low SiC content, since there would be an inadequate concentration of silica formed to fully infiltrate the extensive amount of zirconia formed, a seal would not initially develop, and further oxidation penetrating into the specimen would continue. Eventually, enough silica would form so that it could flow toward the surface, filling in the space between zirconia crystals with liquid, forming a coherent sealing layer, appearing as the glassy surface layer in the cross-section electron micrographs. For higher SiC content specimens, more liquid phase is formed relative to zirconia, allowing a sealing layer to develop with less zirconia surface area to infiltrate, and such glassy layers would be less thick. The oxide underlayers would correspondingly also be less thick, as less SiC must be oxidized to supply liquid phase to form the sealing layer.

The question remains as to why liquid phase is drawn to near-surface regions to form the distinct glassy surface layer observed, leaving a porous region of zirconia, deficient in silica, behind: A completely wetting liquid will flow to coat all solid surfaces, while a non-wetting liquid tends to bead up into a sphere, being self-cohesive and minimizing contact with the solid as well as minimizing its own surface area. Silicate liquids are known to be non-wetting to zirconia [21]. This is consistent with the newly-formed borosilicate liquid phase in this work being wicked up to the initially-formed liquid phase at the surface. The liquid phase

apparently remains adequately wetting to zirconia to form an even surface coating, rather than forming beads on the surface. The wicking direction may also be a result of the newly-formed liquid phase having a lower viscosity than the liquid phase at the surface, since the latter may be more silica-rich from B_2O_3 volatilization. The more fluid liquid would more easily draw to the more viscous liquid.

X-ray diffraction results (Table 1.3) show that TaB_2 or $TaSi_2$ additions to batch compositions form a ZrB_2-TaB_2 solid solution after sintering heat treatments. In the case of $TaSi_2$ additions (ZBSTS), an enhanced SiC content is detected in XRD patterns. This implies the reaction: $TaSi_{2(s)} + 2B_4C_{(s)} \rightarrow TaB_{2(s)} + 2SiC_{(s)} + 6B_{(s)}$ ($\Delta G^\circ_{\text{rxn,1927°C}} = -111.0$ kJ/mol) occurred, in which the TaB_2 product formed a solid solution with ZrB_2, and the B product may be amorphous or below XRD detection. In cases in which TaB_2 is identified in XRD patterns of the ZBSTS series, it is interpreted that the TaB_2 product phase from the above reaction was isolated from contact with ZrB_2, so that a solid solution did not form.

During oxidation heat treatments, SiC oxidized to form $CO_{2(g)}$ (initially) or $CO_{(g)}$ (subsequently) and amorphous silica—the latter not being detectable via XRD. Phases such as SiC and ZrB_2 detected from XRD analysis of the oxidized surfaces of the ZBS series are interpreted as being from phases residing beneath the surface glassy layers and the oxide underlayers. With TaB_2 additions, in our previous work [1], it was shown that the TaC (again detected in this work), is a thermodynamically possible reaction product of oxidation of TaB_2 and SiC. TEM EDS (Figure 1.8) may imply slight solubility of tantalum in ZrO_2, though there is no indication of this from XRD results.

Increasing TaB_2 additions to a ZrB_2-SiC-B_4C composition showed general, though modest, improvement in oxidation resistance at 1200 and 1400°C. At 1500°C, small (3.32 mol%) TaB_2 additions improved oxidation resistance as well. These additions resulted in decreases in the thicknesses of the oxide underlayers, but had no significant effect on the thicknesses of the amorphous surface layers. This improved oxidation resistance is interpreted to correspond to better sealing in the oxide underlayer. This may be from the greater wetting of liquid phase to the TaC particles formed (implied by the right-hand micrograph in Figure 1.8). Alternatively, and the preferred explanation, is that the zirconia particle size is substantially smaller (for equal amounts of SiC) when TaB_2 was introduced (Figures 1.13 and 1.14). This would be expected as oxidation of the tantalum-zirconium boride solid solution to produce segregated phases (ZrO_2 and TaC) would result in smaller particle sizes than the oxidation of pure ZrB_2 to form ZrO_2 alone. The borosilicate liquid phase which forms would have a greater tendency to be entrapped in the oxide underlayers of finer particle sizes. This would make the liquid-encapsulated oxide underlayer more impermeable to atmospheric oxygen, and increase overall oxidation resistance.

Remarkably, additions of TaB_2 in excess of 3.32 mol% resulted in linear mass increases, or in fact, showed acceleration inflection points during the four hour soak periods (Figure 1.5). An overall reduction in oxidation resistance is seen with increasing TaB_2 concentration (Figure 1.9). As the TaB_2 content was increased, both amorphous surface layer and oxide underlayer thicknesses coarsened. As can be seen in Figure 1.14 (lower micrograph), zirconia dendrites appear to be growing through the amorphous surface coating. The rectangular zirconia particle floating in the glass in Figure 1.7 is likely a broken-off portion of a dendite, fractured away by convection currents in the liquid phase [3]. It is speculated that the presence of tantalum, perhaps slightly soluble in the glass, facilitated enhanced solution and precipitation of zirconia in the glassy phase. After a time delay associated with a certain

density of these dendrites having grown to span from the oxide underlayer to the glass surface, a discontinuous acceleration in overall oxidation rate was induced: The dentrites would cause this by either functioning as channels of fast oxygen anion conductors, or via imperfect wetting (sealing) between liquid and the dendrites, facilitating enhanced oxygen penetration through interfacial fissures.

TaB_2 is a more effective additive than $TaSi_2$ at 1500°C, when added in low concentrations (3.32 mol%) (compare Figures 1.9 and 1.11). The accelerating rate of oxidation at 1500°C with TaB_2 additions converts to a decelerating rate as TaB_2 is substituted with $TaSi_2$. As with TaB_2, additions of $TaSi_2$ above 3.32 mol% $TaSi_2$ reduces oxidation resistance, though not to nearly the extent observed with increasing TaB_2. Oxidation of the silicon provided by the $TaSi_2$ additive increased the amount of liquid phase relative to zirconia, and changed the composition of the liquid phase to one which is more silica rich. This liquid phase may be interpreted as being more impermeable to diffusing gaseous oxygen, and/or more inhospitable to solution and precipitation of zirconia dendrites.

V   Conclusions

In the ZBS series, ZrB_2 and SiC oxidized to form a borosilicate liquid and ZrO_2. If the amount of liquid phase was inadequate, it was interpreted that newly-formed liquid was wicked up to join liquid previously formed at the specimen surface. Lower concentrations of SiC resulted in thicker glassy surface layers, with high concentrations of embedded zirconia, and thicker zirconium oxide underlayers. Fixing the SiC content at 27.91 mol%, small (3.32 mol%) additions of TaB_2 were shown to be beneficial in improving oxidation resistance at 1500°C. This was attributed to the oxidation and breakup of TaB_2-ZrB_2 boride solid solution grains into fine-scale ZrO_2 and TaC particles, which better retained an encapsulating liquid phase. Increasing TaB_2 content beyond 3.32 mol% improved oxidation resistance at 1200 and 1400°C; however, oxidation resistance was precipitously degraded at 1500°C. The presence of higher concentrations of tanatlum in some way facilitated solution and precipitation of zirconia dendrites. After some period of time, these dendrites permitted acceleration of oxidation via providing a fast diffusion path either through or along the glass/crystal interfaces of these dendrites. $TaSi_2$ concentrations above 3.32 mol% also resulted in diminished oxidation resistance, but on a much-reduced scale. The higher silica content of the borosilicate glass was interpreted to be less facilitating of the zirconia solution and precipitation mechanism.

Bibliography

[1] Y. Murata and E. B. Whitney, "Densification and Wear Resistance of Ceramic Systems: III. Tantalum Mononitride-Zirconium Diboride," *Am. Ceram. Soc. Bull.,* **48** [7] 698-702 (1969).

[2] Y. Murata, "Densification and Wear Resistance of HfN-ZrB$_2$ Compositions," *Am. Ceram. Soc. Bull.,* **52** [3] 255-259 (1973).

[3] X. Zhang, P. Hu, S. Meng, J. Han, and B. Wang, "Microstructure and Mechanical Properties of ZrB$_2$-Based Ceramics," *Key Engin. Mater.,* **312** 287-292 (2006).

[4] W. C. Tripp, "Effect of an SiC Addition on the Oxidation of ZrB$_2$," *Am. Ceram. Soc. Bull.,* **52** [8] 1606-10 (1973).

[5] M. M. Opeka, I. G. Talmy, E. J. Wuchina, J. A. Zaykosi, and S. J. Causey, "Mechanical, Thermal, and Oxidation Properties of Refractory Hafnium and Zirconium Compounds," *J. Eur. Ceram. Soc.,* **19** 2405-2414 (1999).

[6] A. R. Rezaie, W. G. Fahrenholtz, and G. E. Hilmas, "Oxidation of Zirconium Diboride-Silicon Carbide at 1500°C in a Low Partial Pressure of Oxygen, *J. Am. Ceram. Soc.,* **89** [10] 3240-45 (2006).

[7] A. K. Varshneya, *Fundamentals of Inorganic Glasses,* Academic Press, Inc., New York, 1994.

[8] E. J. Opila, M. C. Halbig, "Oxidation of ZrB$_2$-SiC," *Elec. Chem. Soc. Proc.,* **12** 221-228 (2002).

[9] A. Rezaie, W. G. Fahrenholtz, and G. E. Hilmas, "Evolution of Structure During the Oxidation of Zirconium Diboride-Silicon Carbide in Air up to 1500°C," *J. Europ. Ceram. Soc.,* **27** 2495-2501 (2007).

[10] M. Opeka, I. Talmy, J. Zaykoski, "Oxidation-based Materials Selection for 2000°C $^+$ Hypersonic Aerosurfaces: Theoretical Considerations and Historical Experience," *J. Mater. Sci.,* **39** 5887-5904 (2004).

[11] J. Han, P. Hu, X. Zhang, and S. Meng, "Oxidation Behavior of Zirconium Diboride—Silicon Carbide at 1800°C," *Scripta Mater.,* **57** 825-828, (2007).

[12] S. N. Karlsdottir, J. W. Halloran, and A. N. Grundy, "Zirconia Transport by Liquid Convection During Oxidation of Zirconium Diboride-Silicon Carbide," *J. Am. Ceram. Soc.,* **91** [1] 272-277 (2008).

[13] I. G. Talmy, J. A. Zaykoski, M. M. Opeka, S. Dallek, "Oxidation of ZrB_2 Ceramics Modified With SiC and Group IV-VI Transition Metal Diborides," *Elec. Chem. Soc. Proc.*, **12** 144-158 (2001).

[14] W. Vogel, *Glass Chemistry*, 2nd Ed., Springer-Verlag, New York (1994).

[15] E. Opila, S. Levine, J. Lorincz, "Oxidation of ZrB_2- and HfB_2-based Ultra-high Temperature Ceramics: Effect of Ta Additions," *J. Mater. Sci.*, **39** 5969-5977 (2004).

[16] I. G. Talmy, J. A. Zaykoski, M. M. Opeka, and A. H. Smith, "Properties of Ceramics in the System ZrB_2-Ta_5Si_3," *J. Mat. Res.*, **21** [10] 2593-99 (2006).

[17] S. R. Levine, E. J. Opila, "Tantalum Addition to Zirconium Diboride for Improved Oxidation Resistance," NASA/TM-2003-212483.

[18] S. C. Zhang, G. E. Hilmas, and W. G. Fahrenholtz, "Improved Oxidation Resistance of Zirconium Diboride by Tungsten Carbide Additions," accepted for publication in the *Journal of the American Ceramic Society* August 14, 2008.

[19] X.-H. Zhang, P. Hu, J.-C. Han, L. Xu and S.-H. Meng, "The Addition of Lanthanum Hexaboride to Zirconium Diboride for Improved Oxidation Resistance," *Scripta Mater.*, **57** 1-36-39 (2007).

[20] F. Peng and R. F. Speyer, "Oxidation Resistance of Fully Dense ZrB_2 with SiC, TaB_2, and $TaSi_2$ Additives,"*J. Am. Ceram. Soc.*, **91** [5] 1489-1494 (2008).

[21] W. E. Lee and W. M. Rainforth, *Ceramic Microstructures, Property Control by Processing*, Chapman and Hall, London, UK, 1994.

Chapter 2

Thermogravimetric Analysis of the Oxidation Resistance of ZrB$_2$-SiC and ZrB$_2$-SiC-TaB$_2$-based Compositions in the 1500-1900°C Range

I Introduction

In our previous work [1], the oxidation resistances of ZrB$_2$ containing SiC, TaB$_2$ and TaSi$_2$ additives were studied using isothermal thermogravimetry at 1200, 1400 and 1500°C. Higher concentrations of SiC in ZrB$_2$-SiC mixtures resulted in improved oxidation resistance (up to ~60 mol% SiC) and thinner glassy surface layers, as well as thinner interior layers of ZrO$_2$ mixed with SiO$_2$ and porosity. No layers of ZrB$_2$ depleted of SiC were observed. For low concentrations of SiC, ZrO$_2$ dendrites/needles were observed dispersed in the glassy surface layer. It was interpreted [2] that as borosilicate liquid phase formed, soluble zirconia precipitated out in this form as boron oxide volatilized out of the liquid at its surface, consistent with the observations of Karlsdottir [3]. This zirconia precipitate increased the permeability of oxygen through the glassy layer, facilitating more extensive oxidation and a relatively thick glassy layer. With higher concentrations of SiC, the solubility of zirconia in the more silica-rich borosilicate liquid was diminished, ultimately resulting in a thinner glassy layer forming. Small concentrations of TaB$_2$ (3.32 mol%) enhanced oxidation resistance. TaB$_2$ formed a complete solid solution with ZrB$_2$, the oxidation of which formed a comparatively fine debris of ZrO$_2$ and TaC, which appeared to resist wicking of interpenetrating (boro)silicate liquid phase away to the glassy/liquid surface layer. Higher concentrations of TaB$_2$ resulted in substantially degraded oxidation resistance by facilitating solution and precipitation of zirconia in the glassy surface layer.

Opila et al. studied ZrB$_2$-20 vol% SiC compositions exposed to cyclic oxidation at 1627°C.

30

The microstructure consisted of a surface silicate glassy oxide coating, followed by a region of ZrO_2 dispersed in silica, which in turn was above a region of ZrB_2 depleted of SiC. This region was argued to have resulted from active oxidation of SiC to form $SiO_{(g)}$ [4, 5]. Fahrenholtz [6] showed via a thermodynamic volatility diagram that SiC will oxidize to $SiO_{(g)}$ and $CO_{(g)}$ at lower oxygen partial pressures than ZrB_2 oxidizes to $ZrO_{2(s)}$ and $B_2O_{3(l)}$. Opeka et al. have suggested that formation of $SiO_{(g)}$ could build up to pressures exceeding ambient, facilitating rupture of the protective glass layer, resulting in a cyclic protective/non-protective scale-forming sequence [7]. In low oxygen partial pressures, formed by $CO_{(g)}/CO_{2(g)}$ mixtures, ZrB_2 oxidized to $ZrO_{2(s)}$ and a volatile boron oxide, and SiC oxidized to carbon monoxide and $SiO_{(g)}$. This left a non-protective (porous) ZrO_2 scale [8].

Studies on the oxidation resistance of ZrB_2-SiC two-phase mixtures at temperatures above 1500°C are limited. Oxidation heat-treatments based on zirconia heating elements [9, 10] or self-heated ribbons [11] have been used for the range 1700-1900°C. Karlsdottir et al. found that after oxidation heat-treatment at 1700°C for 15 min, a thin outermost silica layer formed, followed by a columnar zirconia layer with embedded silicate liquid phase, followed by a SiC-depleted ZrB_2 zone, in turn followed by an unreacted core. Han et al. found that the oxidation resistance of a ZrB_2-20 vol% SiC composition at 1900°C for 1 h exceeded compositions with either 10 or 30 vol% SiC [9]. Hu et al. have shown that (10 vol%) TiB_2 or TaB_2 additions to ZrB_2-20 vol% SiC had markedly detrimental effects on 1800°C oxidation resistance [12]. At temperatures at and above ∼2000°C, arc-jet heating has been used to evaluate the ablation resistances of UHTCs [13, 14, 15]. At 2300°C, a ZrB_2-20 vol% SiC composition was unable to resist the simulated aerothermal load [13]. Below 2200°C the oxide scales are similar to those oxidized under static air furnace conditions. Above this temperature, no distinct silica layer was observed, and the outermost layer was composed of a zirconia scale [13]. An oxyacetylene torch has also been used to evaluate the resiliance of a ZrB_2-SiC composite to the gasous environment created by the torch at a temperature of 2200°C [16]. The testing results are similar to those of arc-jet testing, however a more distinct SiC-depleted zone was observed.

In our previous work, as well as many others, the temperature limitations of commercially-available thermogravimetric analyzers in an oxidizing environment has limited in-situ characterization of oxidation resistance to ∼1500°C. In this work, for selected compositions, that range was expanded to 1900°C through the use of zirconia heating element furnace with a water-cooled analytical balance coupled beneath it.

II   Experimental Procedure

Commercially-available powders were used for raw materials. The major crystalline phase(s), grade, and suppliers are listed for each powder in Table 3.1. The particle sizes of commercially-available TaB_2 were deemed too large for pressureless sintering. Hence, sedimentation-based selection was used to obtain finer particles: Powders were dispersed in ethanol using an ultrasonicator (FS-14 Solid State Ultrasonicator, Fisher Laboratory Equipment Division, Pittsburgh, PA) for 10 min. The mixture was allowed to settle in ethanol for 1 h. The top 7 cm (of a total column height of 14 cm) of fluid was then extracted using a pipette. Based on laser particle size analysis (Model LS 13 320, Beckman Coulter, Fullerton, CA), decanted particles had a d_{50} of 1.1 μm. The decanted suspensions were dried in a beaker on

Table 2.1: Raw Material Characteristics

	Phases	Particle Size	Supplier
ZrB_2	ZrB_2	$d_{50} = 2.20~\mu m$	Grade B, H. C. Starck, GmbH
B_4C	stoichiometric B_4C	$d_{50} = 0.8~\mu m$	Grade HS, H. C. Starck, GmbH
SiC	α-SiC	$d_{50} = 0.88~\mu m$	Grade 8S490NDP, Superior Graphite, Chicago, IL
TaB_2	TaB_2, Ta_3B_4	$< 43~\mu m$	ESPI Metals, Ashland, OR

a hot-plate.

The compositions of synthesized powder mixtures are given in Table 2.2. The powder

Table 2.2: Sample Compositions

Composition	Mole Percent				Volume Percent			
	ZrB_2	B_4C	SiC	TaB_2	ZrB_2	B_4C	SiC	TaB_2
1	77.39	7.27	15.34	0	80.35	8.94	10.71	0.0
2	64.25	6.04	29.70	0	70.30	7.82	21.88	0.0
3	37.55	3.53	58.92	0	46.15	5.14	48.71	0.0
4	63.14	5.62	27.91	3.32	68.79	7.25	20.45	3.51

mixtures were suspended in methanol, and mixed in a ball mill for 24 h, using B_4C as media. These powders were then dried in air in a free convection oven at 75°C. The powders were then ball milled again in water with dissolved polyvinyl alcohol (PVA, Celanese Ltd., Dallas, TX), polyethylene glycol (PEG, Alfa Aesar, Ward Hill, MA), and Darvan 821A (R.T. Vanderbilt Company Inc., Norwalk, CT), using B_4C as media for 8 h. PVA functioned as a binder with PEG functioning as a plasticizer, and Darvan 821A served as a dispersing agent. The highly viscous suspension after this milling step was dried in a free convection oven at 75°C, and then sieved using a 60 mesh screen.

Approximately 400 mg of powder were uniaxially pressed into cylindrical pellets using a maximum pressure of 117 MPa, holding for 1 min. The pellets were loaded into latex encapsulants which were in turn evacuated. These were cold isostatically pressed (CIP) in a water/oil mixture at 345 MPa for 1 min. This was followed by a binder removal heat-treatment of 0.25°C/min to 500°C under a flowing argon atmosphere. Fifteen pellets were fabricated for each composition.

These pellets were fired in a graphite tube furnace (Model M11, Centorr Vacuum Industries Inc., Nashua, NH) under flowing argon, using graphite setters. The furnace was initially evacuated to ~4 Pa (roughing pump) and backfilled with argon. The typical heating schedule was 50°C/min to 2100°C, soaking for 1 h, and then cooling at 40°C/min to room temperature. The pellets were then hot isostatically pressed (HIP, American Isostatic Press, Columbus, OH) at 1800°C for 30 min under an argon gas pressure of 207 MPa. The densities of unfired pellets were determined from measured dimensions and mass; the densities of pressureless sintered and post-HIPed pellets were determined using Archimedes' method.

All HIPed specimens were 100% dense based on theoretical densities calculated from the rule of mixtures.

All of the surfaces of the post-HIPed samples were ground away using 320 grit SiC grinding paper (Buehler, Lake Bluff, IL), and the resulting pellet dimensions were measured with calipers, from which surface areas were calculated. Pellets were ~5.3 mm in diameter and 3-4 mm in height. The oxidation behaviors were then investigated using thermogravimetric analysis. An analytical balance (model AX205, Mettler-Toledo, Inc, Columbus OH) with a measurement precision of 0.01 mg was fully encased in a water-cooled aluminum enclosure. The enclose had a coupling extending from its top which mated with a water-cooled coupling attached to the base of the furnace which was sealed to and supported a stabilized zirconia tube with a 4.7 cm inner diameter. This tube extended upward through the hot zone of the furnace and continued through the top of the furnace for an additional 35.5 cm into the ambient air. Loose refractory alumina fiber rested at the top of the tube to minimize air turbulence within the tube which would otherwise disturb the balance reading. A mass flow controller (Model GFC 17, Aalborg, Orangeburg, NY), attached to a cylinder of compressed dry air controlled air flow into the enclosure and then through the zirconia tube which in turn extended through the furnace. The furnace (model DT-36-VT 2000°C vertical tube furnace, Deltech, Inc, Denver, CO) was of cylindrical shape, mounted (cylindrical axis) vertically. Outer radial positions of the furnace were heated using uniformly-spaced $MoSi_2$ U-tube heating elements. These were partially insulated from radial positions toward the furnace center by shaped stabilized zirconia bricks. Along still more inner radial positions of the furnace, six symmetrically-placed rod-type stabilized zirconia heating elements extended vertically through the furnace. Two independent PID control systems were used, one which brought the furnace temperature up to ~1300°C via the $MoSi_2$ elements, at which point power was additionally applied across the semiconducting zirconia elements. The hot zone of the furnace was approximately 10 cm along the axial direction, with another 40.5 cm of length extending from the edges of the hot zone to the axial extremes of the furnace. Raising the hot-zone temperature from room temperature to 1900°C required ~2 days. The furnace was brought to isothermal soak temperatures of 1500, 1600, 1700, 1800, and 1900°C and held at each of those temperatures while isothermal oxidation experiments were performed on all compositions. Data was collected on a personal computer through rapid polling (using Microsoft Visual Basic 4.0) through RS232 communications.

A brass tripod with set-screw feet (for orientation adjustment) was fabricated and placed on the balance stage. Inserted into this was a stabilized yttria-stabilized zirconia (McDaniel Advanced Ceramic Technologies, Beaver Falls, PA) hollow tube (6.3 mm outer diameter, 61 cm long). Placed at the top of the hollow tube were stabilized zirconia crucibles, consisting of a bottom stem which could be inserted into the stabilized zirconia tube, and a cylindrically-shaped partially hollowed cylindrical container. These were fabricated by uniaxially pressing 2 cm cylinders of stabilized zirconia powder (8 mol% Y_2O_3 stabilized ZrO_2, $d_{50} = 0.5$ μm, Inframat Advanced Materials, Manchester, CT) mixed with binder at 125 MPa. These were subsequently loaded into latex bags which were evacuated and sealed, and were then CIPed at 345 MPa. These functioned as blanks for CNC machining (model DSLS 3000, Taig Micromill, Chandler AZ) into the aforementioned crucible shape. Binder was extracted from the green parts in static air at a heating rate of 0.5°C/min to a soak temperature 500°C, and held for 4 h. These parts were then fired in the same furnace as the oxidation experiments using soak temperatures in the range 1600-1800°C for 1 h. Specimens for oxidation experiments

were placed in these crucibles (on top of zirconia chips lining the bottom of the crucible) so that the axial direction of the disks was horizontal, leaving a portion of the disk within the crucible, and a larger proportion extending above the upper lip of the crucible.

The analytical balance and its enclosure, with the specimen mounted above it, were raised using a foot-pedal-based jack system into the hot zone of the furnace. Specimens were elevated over ∼5 min so as to raise the sample quickly to its soak temperature, while minimizing the propensity for thermal shock of the stabilized zirconia crucibles and supporting tube. Air flow rate upward through the tube was maintained at 0.1 l/min. Specimen weight change was based on the weight measured by the balance while the specimen was at room temperature. Weight change data during the period of elevating the balance was omitted since the balance measurement was unstable. To evaluate repeatability, 2-3 thermogravimetric oxidation heat-treatments were performed on each composition at each soak temperature. Displayed traces are those considered most representative.

Thermogravimetric analyzers show a buoyancy effect [17] in which the condensed phases of the specimen, and the structure which holds it up, applies an upward force based on the mass of gas which is displaced (Archimedes principle). As the furnace is heated, this gas expands and the displaced mass decreases, giving the impression of a weight gain on the TG trace. This mass change can be calculated assuming an ideal gas (air), a constant temperature in the hot zone of the furnace, and a linear temperature gradient extending from the edge of the hot zone to the point of exit of the furnace, which is assumed to be at room temperature. For the specimen, crucible, and the hot-zone portion of the hollow tube the crucible is mounted on, the buoyancy mass m was calculated based on:

$$m = \frac{MpV_H}{RT_F}$$

where M is the molar mass of air, p is atmospheric pressure, V_H is the volume of the specimen, crucible, and support tube (1032.31 mm^3), R is the gas constant, and T_F is the hot zone absolute temperature. For the hollow stabilized zirconia tube extending through the linear temperature gradient, the bouoyant mass was calculated based on:

$$m = \frac{MpA}{R\left(\frac{T_F - T_R}{h}\right)} \ln\left(\frac{T_F}{T_R}\right)$$

where A is the cross-sectional area of the tube, T_R is absolute room temperature, and h is the height of the portion of the furnace associated with the linear temperature gradient going from room temperature to the hot zone temperature. The mass of displaced gas at a given hot-zone temperature minus the mass of displaced gas at room temperature was calculated.

Crystalline phases in the samples were identified using X-ray diffraction (XRD, Model X'Pert PRO Alpha-1, PANalytical, Netherlands). Scans were recorded at room temperature over a 2θ range of 10-80° at a scan rate of 0.01°/s. XRD of oxidized specimens were taken from cross sections formed via a diamond wafering blade.

Specimens were directly photographed with a digital camera after cross-sections were made via a diamond-impregnated wafering blade. Microstructures of oxidized samples were investigated using scanning electron microscopy (SEM, LEO 1530, Carl Zeiss SMT, Inc., Thornwood, NY) and energy dispersive spectrometry (EDS, Oxford Pentafet detector with ultrathin window, Oxford Instruments, Oxfordshire, UK). For displayed micrographs, specimen cross-sections were fractured surfaces formed via impact, with the oxidized surfaces

mounted on the SEM stub to be parallel with the beam axis. Specimens were coated with gold (sputtering for 2 min) to form a conductive surface. For measurement of layer thicknesses, specimens were cut perpendicular to the oxidized surfaces using a diamond-impregnated wafering blade, and then imaged in the SEM. Separate measurements of the top, sides, and bottom layer thicknesses were recorded. Side thicknemss measurements were generally averages of measurements from the left and right sides.

III Results

Initial experiments were performed using an alumina gas flow tube and either alumina stages or crucibles to hold the specimens. Oxidation heat-treatment in this study at and above 1700°C showed substantial reaction of specimens with their containers. For that reason, the furnace was reconstructed so that no alumina was present in the hot zone. All results which follow correspond to oxidation under that configuration.

Phases identified from XRD of oxidized specimen cross sections were ZrB_2, SiC, and ZrO_2. For compositions in which TaB_2 was a batch additive, no distinct TaB_2 phase was detected, but a shift in 2θ positions of ZrB_2 peaks imply the formation of a $Zr_xTa_{1-x}B_2$ solid solution. Trace amounts of ZrC were detected for the composition with ∼60 mol% SiC after oxidation heat-treatments at 1600 and 1700°C. Trace amounts of ZrC were also detected for the composition with ∼3 mol% TaB_2 after oxidation heat-treatment at 1800°C.

Figure 2.1 shows TG traces of the compositions exposed to temperatures ranging from 1500 to 1900°C. At 1500 and 1600°C, all compositions are roughly grouped together with the exception of ∼15 mol% SiC, which showed a higher initial weight gain, but roughly equal rate of weight gain with time as the other specimens. This was not the case for 1700 to 1900°C heat-treatments; the ∼15 mol% SiC composition gained weight at a comparatively rapid rate, though the rate slowed over the 10-30 min time span. At 1900°C the ∼30 mol% SiC and ∼28 mol% SiC – ∼3 mol% TaB_2 specimens showed a constant and remarkably small weight gain over the evaluated time span. The ∼60 mol% SiC specimen showed an initial rapid rate of weight gain that decreased at longer times. The thermograimetry trace shown for the specimen with ∼60 mol% SiC was altered from the original, which displayed periodic spikes from the popping of bubbles, after which an instantaneous downward shift in mass was recorded. For the trace displayed in Figure 2.1, the spikes were deleted and subsequent data were adjusted upward to align with the data before the spikes.

The results of buoyancy calculations are shown in Figure 2.2. Also shown in this figure is a summary of the results in Figure 2.1 by comparing the mass change after 100 minutes of exposure at the various soak temperatures. Accounting for buoyancy effects, a weight loss for the specimen with ∼30 mol% SiC occurred after heat-treatments at 1600 and 1700°C. Using the weight loss (per unit surface area) in Figure 2.2, the thickness of a ZrO_2/SiO_2 oxide coating was calculated (Figure 2.3) based on equations developed in the appendix. Weight losses used in the calculation were based on the differences between measured values after 100 min and the weight change associated with buoyancy for a given temperature.

The oxidation resistances of all specimens except ∼15 mol% SiC are remarkably good. The substantial difference between oxidation resistances of specimens with ∼15 mol% SiC and ∼30 mol% SiC is visually apparent when the oxidation scale was examined in cross section (Figure 2.4). With ∼15 mol% SiC (Figure 2.4a) the extensive oxidation product layer is
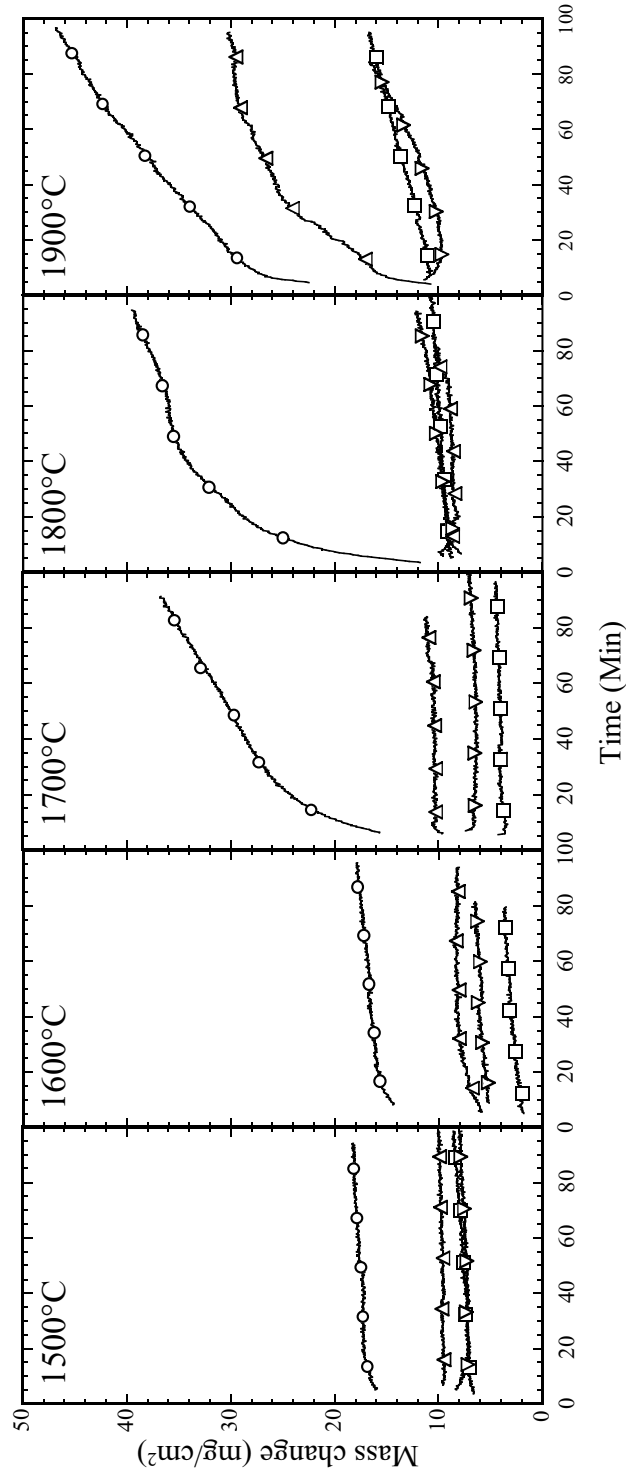
Figure 2.1: Compilation of thermogravimetry traces for various isothermal exposures to flowing dry air at the indicated temperatures. Circle: 15.34 mol% SiC; square: 29.74 mol% SiC; upward triangle: 58.92 mol% SiC; downward triangle: 27.91 mol% SiC – 3.32 mol% TaB_2. In this figure, symbols are used only to identify traces; each TG trace is made up of ∼1000 data pairs.
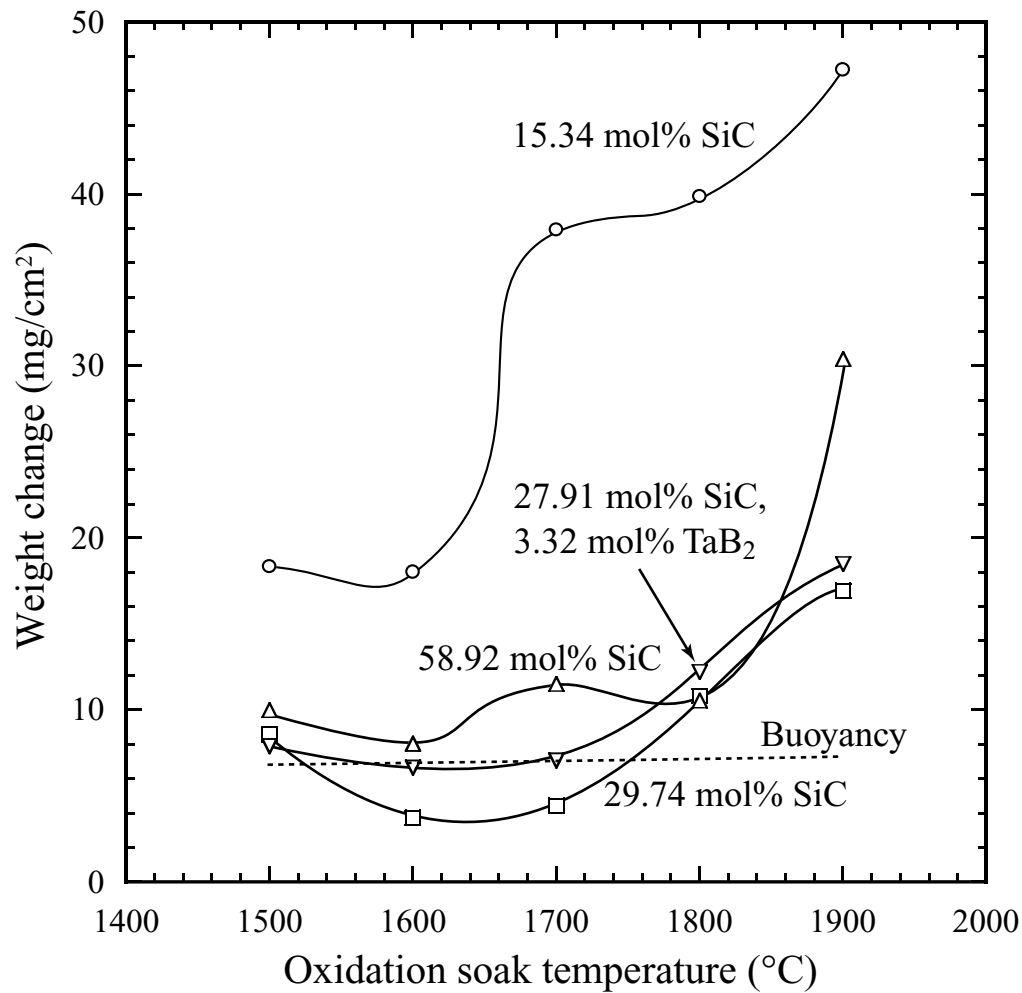
Figure 2.2: Weight change of various compositions exposed to flowing air at various temperatures after 100 min of oxidation. Extrapolated values were used for oxidations which were completed before 100 min. Experimental data are not corrected for buoyancy effects, which are separately displayed in the figure (dashed line).
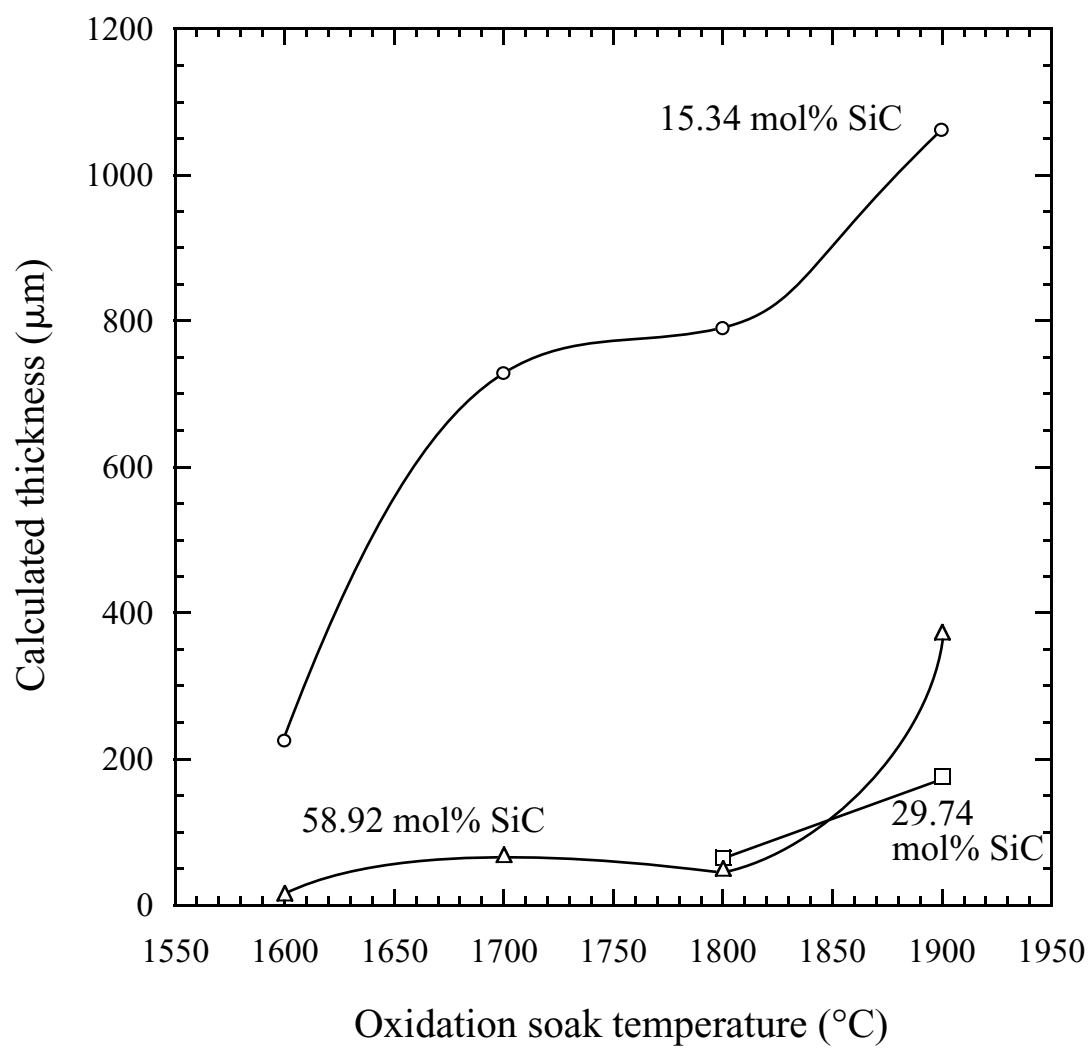
Figure 2.3: Oxide coating thicknesses based on measured weight losses.
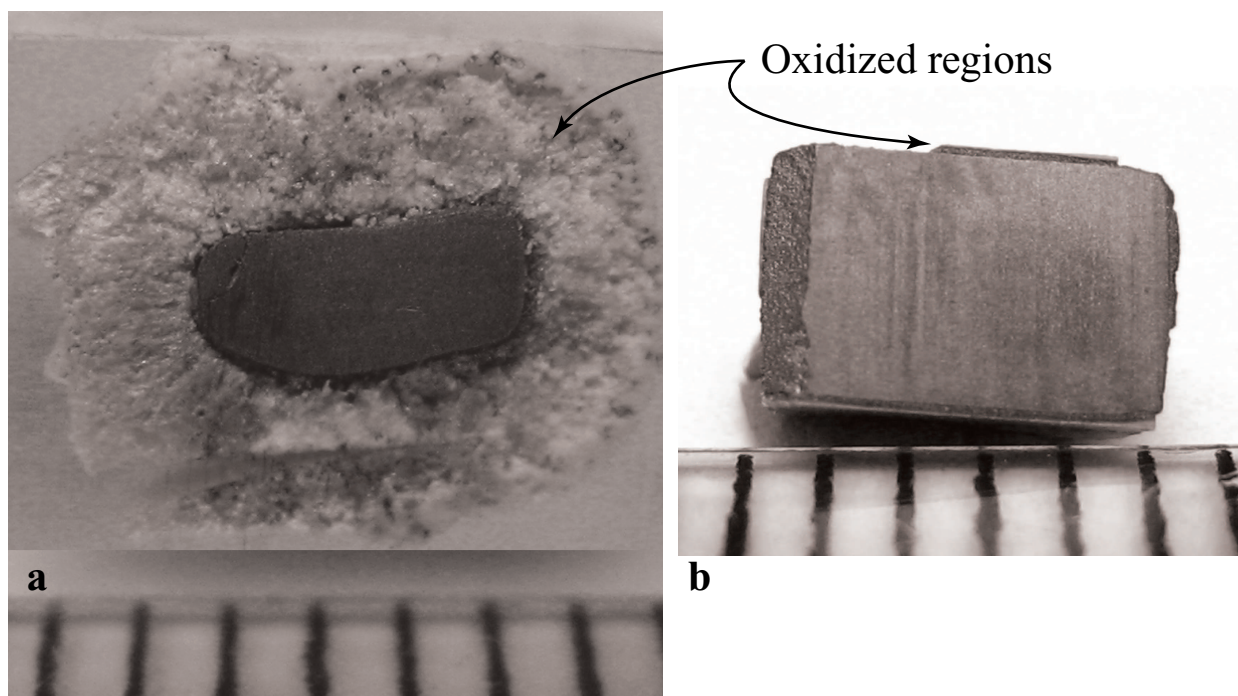
Figure 2.4: Cross sections (via diamond wafering blade) of specimens heat-treated at 1800°C for ~90 min. a) 15.34 mol% SiC. b) 27.91 mol% SiC. The ruled lines are 1 mm apart. The specimen in a) was mounted in the crucible in the furnace such that the bottom of the part is out of the page, and the top extends into the page. The reaction layer in b) is not uniform as portions of it snapped off as the displayed axial cross-section was being cut.

mostly zirconia (based on EDS analysis of this region of the specimen in the SEM) with a small concentration of silica, in the region nearest to unreacted ZrB_2/SiC. The specimen with ~30 mol% SiC (Figure 2.4b) showed comparatively impressive oxidation resistance, with only a thin (~0.1 mm) reaction product layer (the makeup of which is discussed subsequently) covering an unaltered interior.

Figure 2.5 shows a cross-sectional fracture surface of near-surface regions of the ~15 mol% SiC specimen oxidized at 1600°C. An amorphous silica-containing layer (a) with embedded zirconia coats the specimen surface. Boron is unreliably detected with the available EDS so the extent to which the amorphous layer contained boron oxide has not been established. Slightly (~10 μm) below this layer are fragmented zirconia particles (b), making up collective shapes correlating to ZrB_2 grains appearing in the specimen interior. The zirconia regions were distinguished from ZrB_2 by presence/absence of oxygen peaks in EDS data, and the tendency for bright spots from charging effects on the non-conductive ZrO_2 regions. Pores (c) (of shapes similar to SiC grains seen in the specimen interior) reside in the region of transition from ZrO_2 to ZrB_2 grains. The specimen interior (d) consists of ZrB_2 lighter-shaded grains and darker-shaded SiC grains.

As shown in Figure 2.6, the ~15 mol% SiC specimen heat-treated at 1800°C showed distinct layers of oxidation products penetrating from the surface inward: a zirconia-embedded silica-containing glass surface layer (a), a region of high concentration of ZrO_2 particles in-
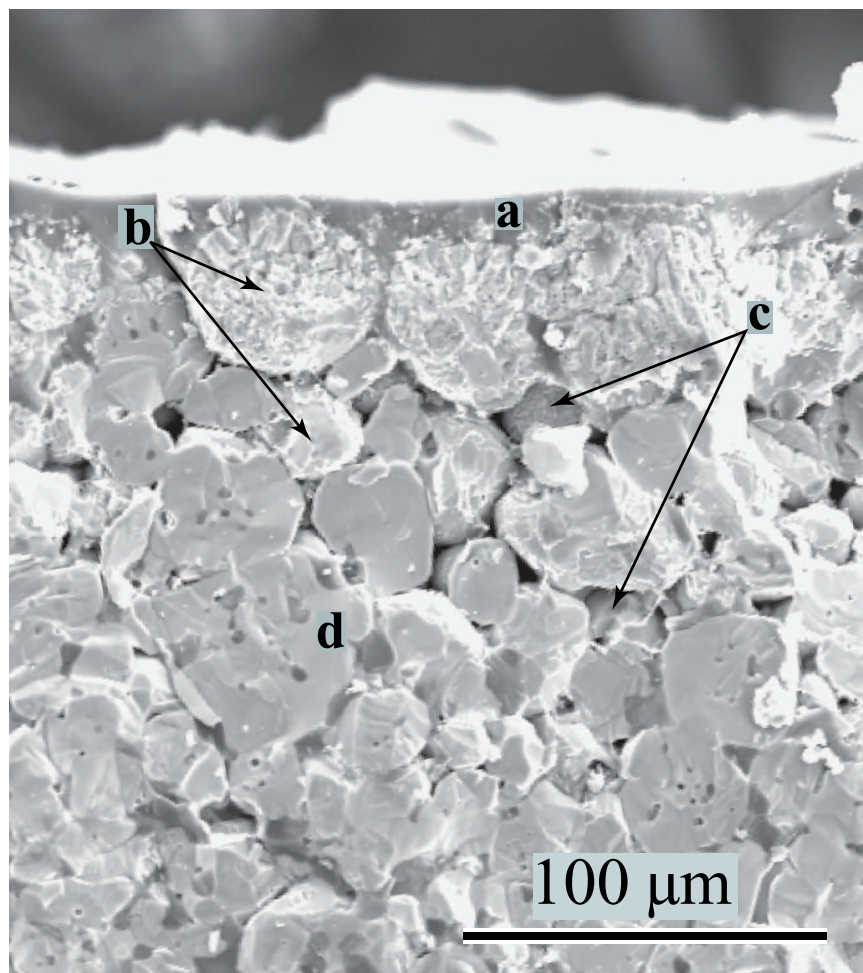
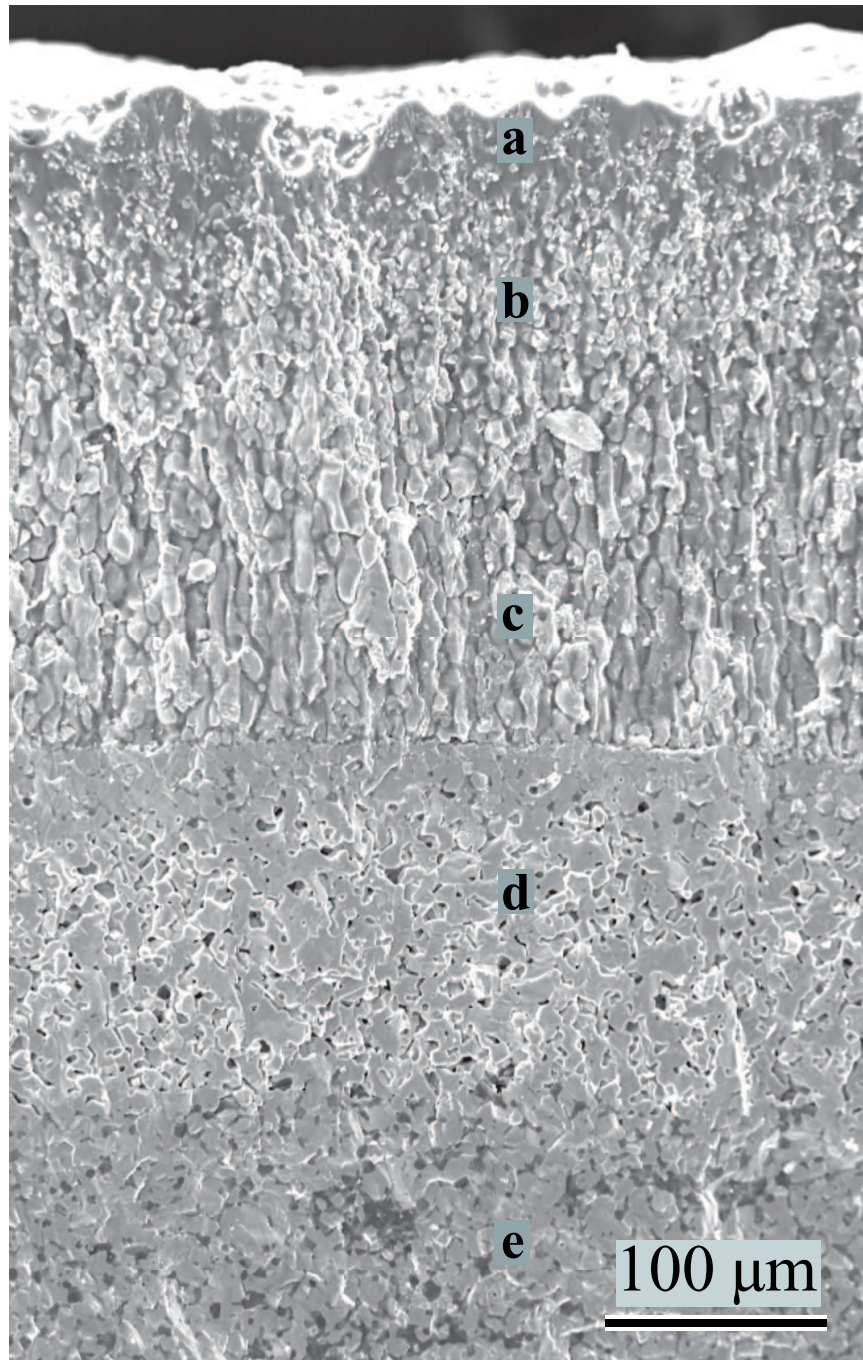Figure 2.5: ~15 mol% SiC specimen oxidized at 1600°C for ~90 min.

Figure 2.6: ~15 mol% SiC specimen oxidized at 1800°C for ~90 min.

fused with silica-containing glass (b), a region in which zirconia particles with no surrounding liquid/glass phase are elongated in the direction orthogonal with the surface (c). A transition along a distinct interface is then observed to ZrB_2 grains with pores taking the place of what was once SiC grains (d). The most interior region consists of the original ZrB_2-SiC matrix (e). The $\sim$15 mol% SiC oxidized at 1700°C showed similar layers, though of diminished thicknesses. The microstructure in Figure 2.6 came from the top portion of the specimen.

Increasing the SiC content from 15 to 30 mol% produces a microstructure with a separate silicate glassy layer largely devoid of zirconia, and layers similar to that previously described underneath, with the exception that there was no zone of elongated ZrO_2 and porosity (Figure 2.7). At 1900°C (Figure 2.8), the specimen with $\sim$30 mol% SiC developed a glassy silica-containing surface layer (a), within which the amount of embedded zirconia is difficult to determine. At greater depths, this transitions through a sharp boundary to a broad zone of ZrB_2 (b), which is devoid of SiC. These particles have rounded from their appearance as grains in the original two-phase matrix, surrounded by porosity. Still deeper, at another sharp boundary, the original ZrB_2/SiC matrix can be seen (c).

The microstructure of $\sim$60 mol% SiC oxidized at 1700 and 1800°C is similar to $\sim$30 mol% SiC oxidized at the same temperatures, though the relative depths of the SiC-depleted ZrB_2 zones are thinner, and the zone of ZrO_2 surrounded by glass is more dilute in ZrO_2. After heat-treating this composition at 1900°C, bubbles are observed in the glassy silica-containing layer (Figure 2.9).

In our previous work at 1200-1500°C, addition of TaB_2 to specimens oxidized at 1600°C changed the appearance of the layer of ZrO_2 embedded in glass to one in which the crystalline phases appear more fragmented. That effect was not as visually apparent for oxidation heat-treatments at 1700-1800°C; however, these specimens showed somewhat thinner layers of glass-infused zirconia and SiC-depleted ZrB_2, as compared to specimens without TaB_2 additions, but similar SiC content. After oxidation at 1900°C (Figure 2.10), the region of ZrB_2 depleted of SiC was substantially thinner than the case in which TaB_2 was not added (Figure 2.8).

There was clear visual evidence of the flow of silicate glassy phase onto the ZrO_2 chips on which specimens were resting, as well as down onto the bottom of the zirconia crucible. Figure 2.11 shows the temperature variation in thicknesses of the glassy surface layers, the oxide ZrO_2/silicate liquid layers beneath them, and the SiC-depleted ZrB_2 regions still further into specimen interiors. For $\sim$15 mol% SiC composition, distinct glass layers were not apparent. The layers of predominantly ZrO_2 were coarser than the SiC-depleted layers; both layers generally coarsened with increasing soak temperatures. The ZrO_2 layer became generally coarser in going from top to bottom of the specimen. For the $\sim$30 mol% SiC specimens, the thickness of the layer at the specimen bottom was again coarser than the sides or top. Glassy surface layers were apparent, whose thickness did not vary substantially with soak temperature. The composition with $\sim$60 mol% SiC showed a substantial increase in layer thicknesses in going from 1800 to 1900°C soaking temperatures. Layer thicknesses were generally least coarsened for the compositions with $\sim$28 mol% SiC and $\sim$ 3 mol% TaB_2. For both $\sim$30 mol% SiC and the composition with $\sim$28 mol% SiC and $\sim$3 mol% TaB_2, glassy layer thicknesses appeared to decrease slightly in going from 1700 to 1800°C soak temperatures.
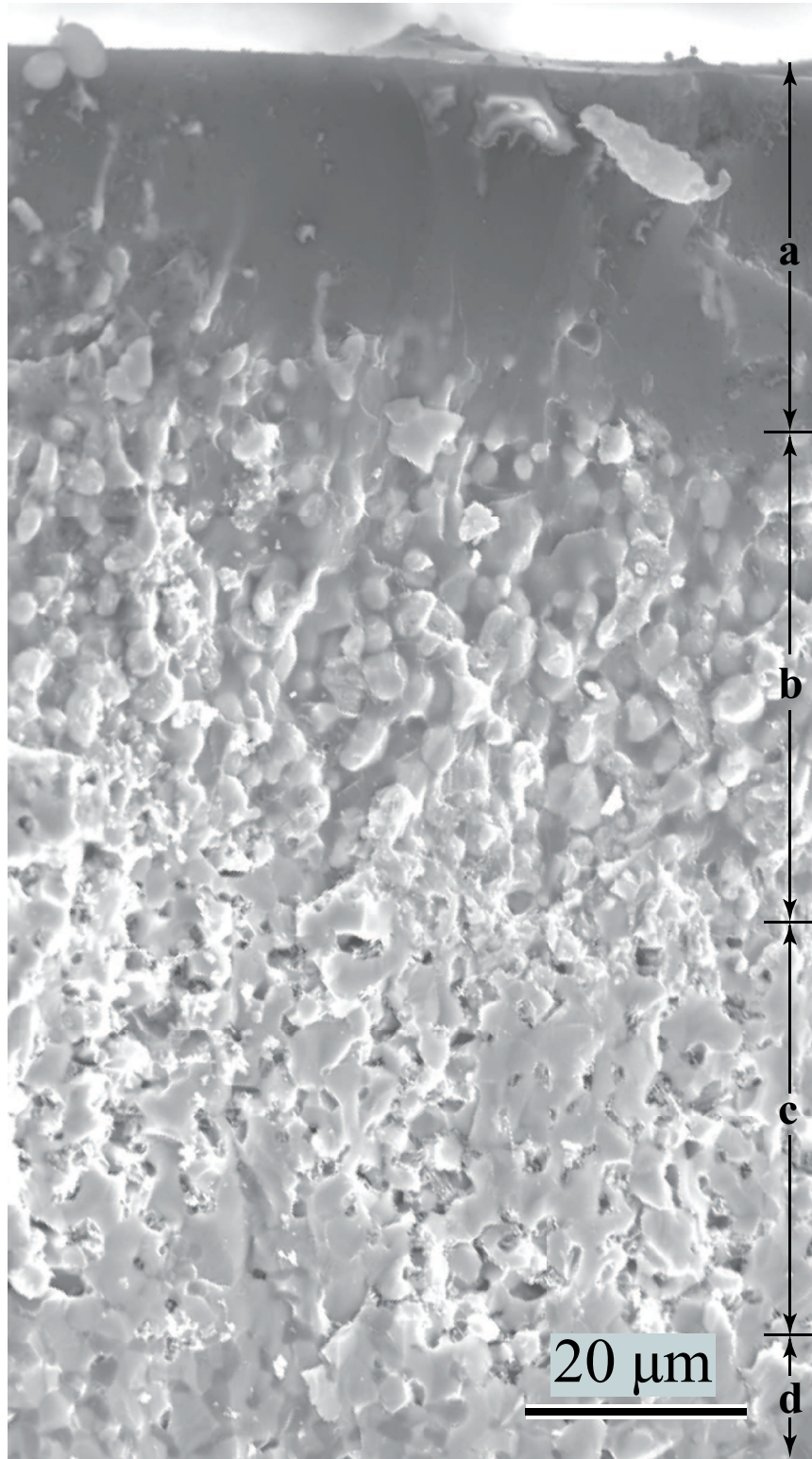
Figure 2.7: ~30 mol% SiC specimen oxidized at 1700°C for ~90 min. Marked regions: a) Glassy region adjacent to the surface. b) Zirconia particles immersed in silicate glass. c) ZrB_2 regions depleted of SiC. d) Un-transformed ZrB_2-SiC.

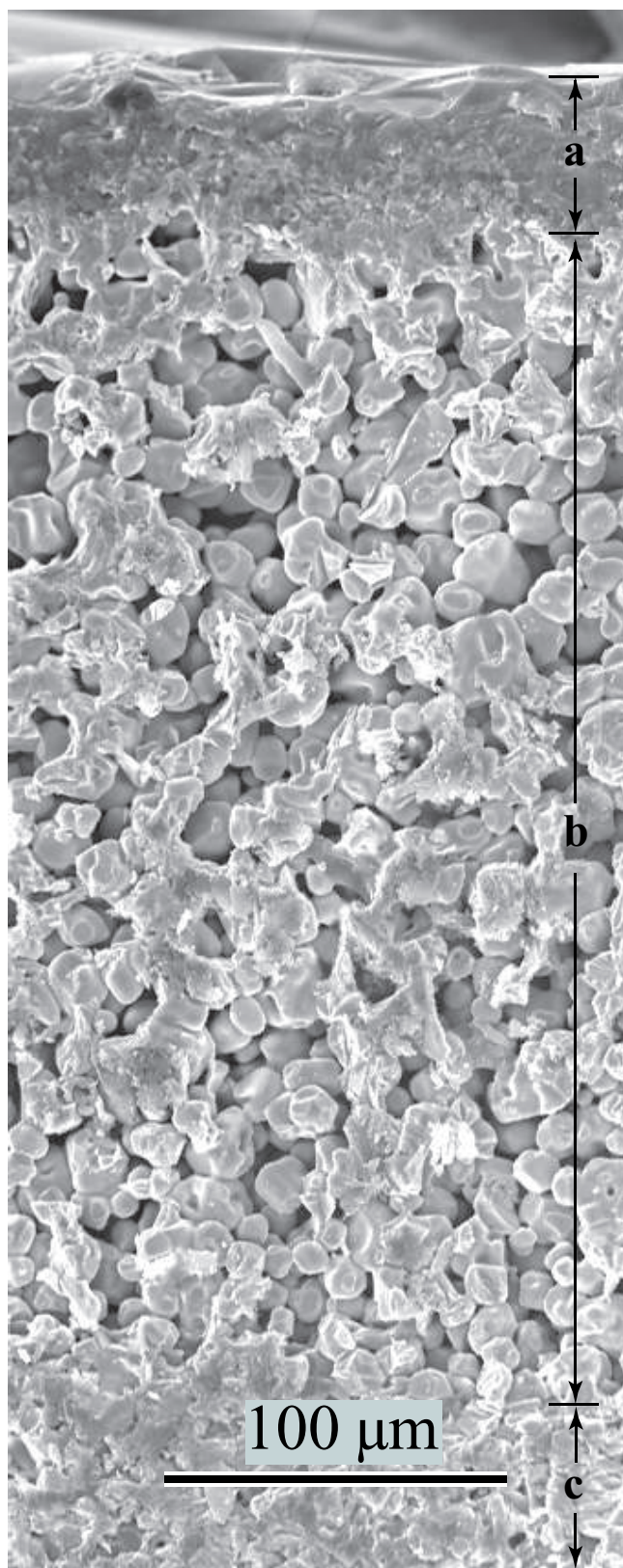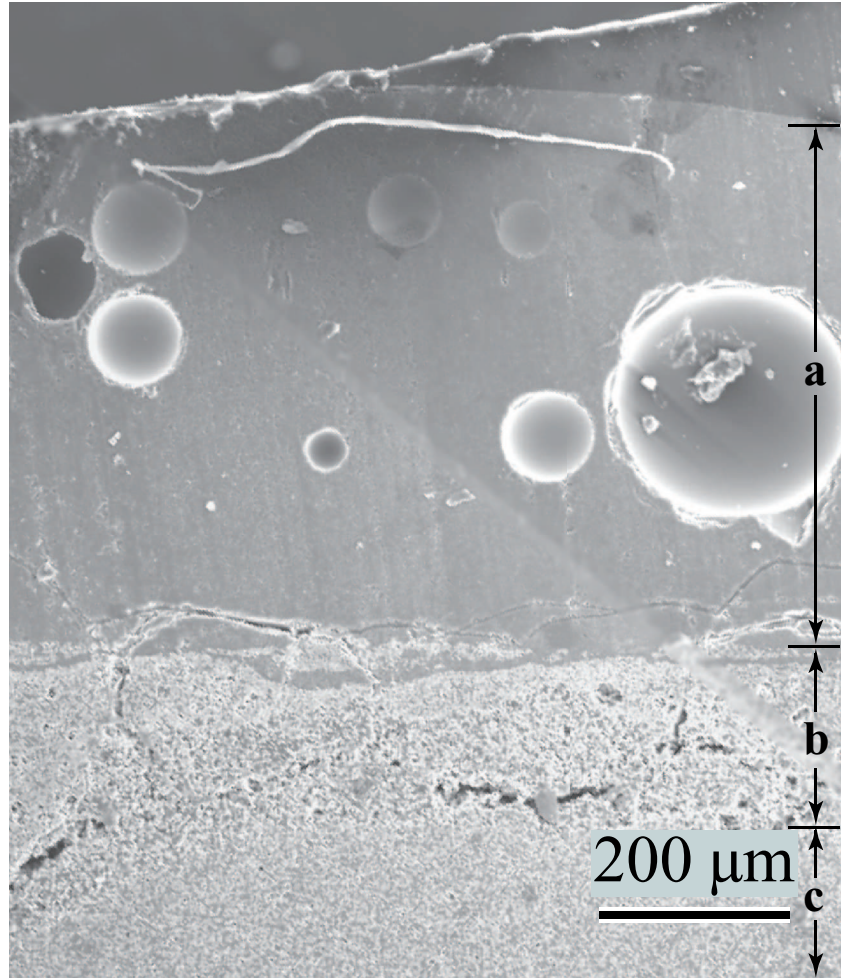Figure 2.8: ~30 mol% SiC specimen oxidized at 1900°C for ~90 min.

Figure 2.9: Comparatively low-magnification of ∼60 mol% SiC specimen oxidized at 1900°C for ∼90 min. a) Glassy layer with imbedded bubbles. b) ZrB_2 with regions which had SiC replaced by porosity. Cracks/fissures in this layer are interpreted to have resulted from stresses via differences in coefficient of thermal expanions during cooling. c) Un-transformed ZrB_2-SiC.
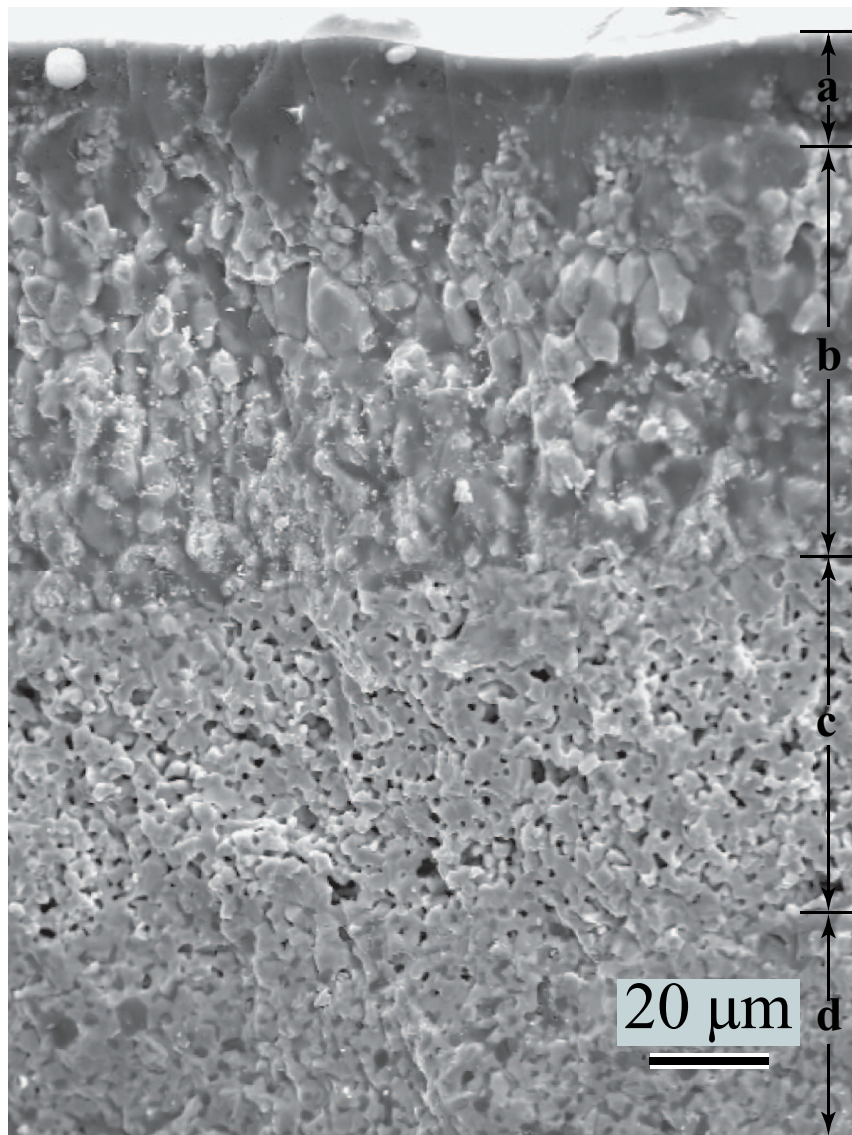
Figure 2.10: ~28 mol% SiC - ~3 mol% TaB$_2$ specimen oxidized at 1900°C for ~90 min. Letter markers correspond to the same region types as in Figure 2.7.

Figure 2.11: Thicknesses of various layers, as measured in the SEM, of oxidation-altered ZrB_2-based ceramics.
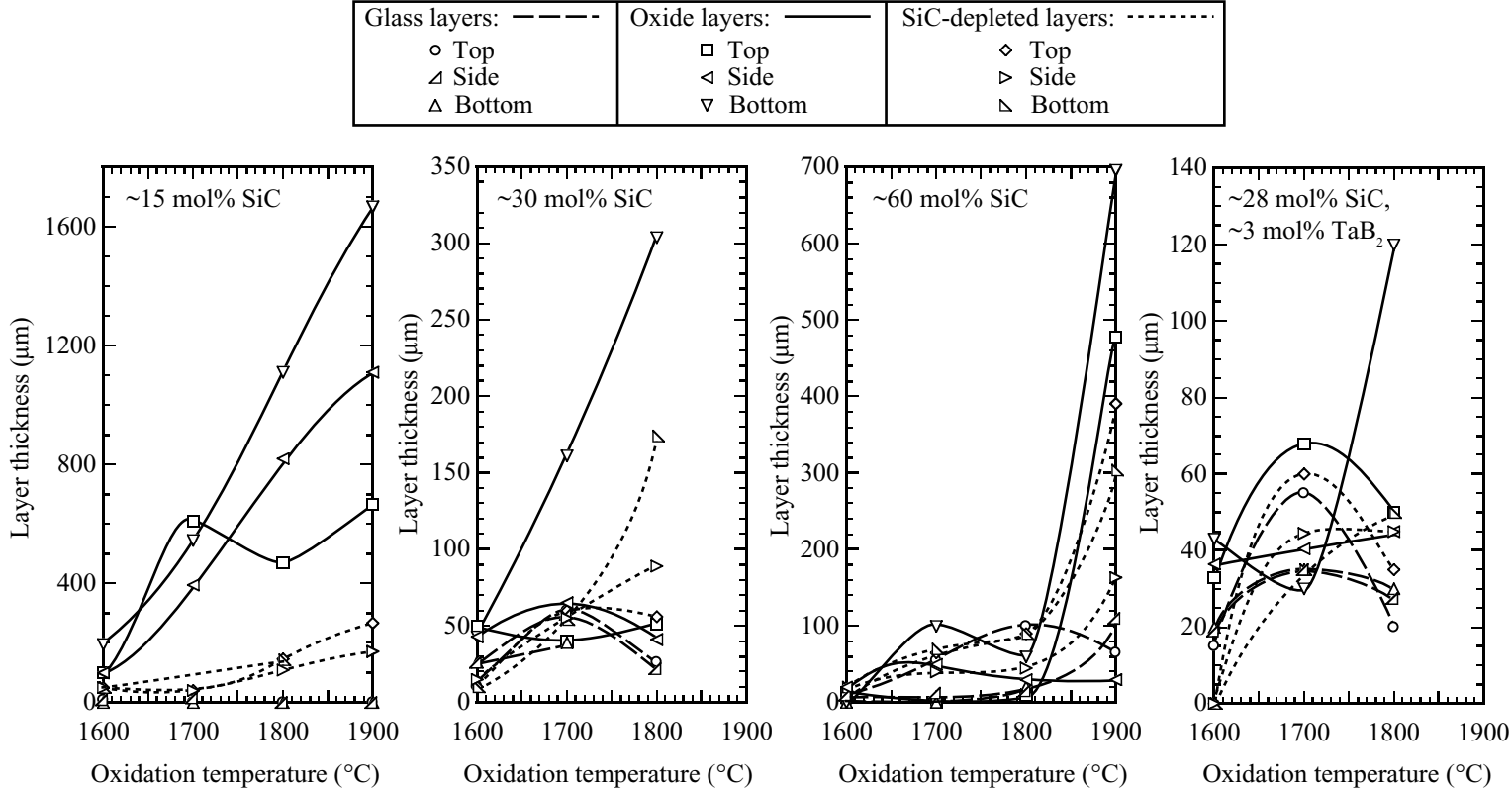
IV Discussion

Up through oxidation temperatures of 1600°C, all evaluated compositions developed a passivating glassy surface layer along with an oxide layer beneath it which were protective for the evaluated time period. Starting at 1700°C, the composition with ∼15 mol% SiC lacked enough SiC to form an adequate volume of silica/borosilicate glass for passivation.

Silicate liquid phase was drawn into the crucible either by gravity, or by capillary action at the contact points. The capillary removal mechanism would imply preferential removal of liquid in close proximety, which is near the bottom of the specimen. This in turn would make this region more vulnerable to oxidation, the coarser oxide layers observed in these regions.

The ∼15 mol% SiC specimen shows a slowing of weight gain after ∼30 min to a near-linear weight gain with time (Figure 2.1). If oxidation were occurring through a diffusion-resistive layer which was coarsening with time, TG traces with a more continuous parabolic shape would have been expected. It is interpreted that initial parabolic behavior changed to a linear weight gain as the formation of silica liquid through oxidation was matched by its capillary extraction.

Calculated oxide layer thicknesses from weight loss data were within the spread of the three measured (top, middle, bottom) thicknesses of the oxide portion of the microstructure (Figure 2.11). Compared to the total thicknesses of all the characteristic layers, the calculated thicknesses were roughly lower. The differences may be attributable to the inaccuracy of assumptions in the buoyancy calculations (e.g. linear temperature gradient), development of porosity (e.g. vapor pressure within the specimen pushing liquid toward the surface), and/or preferential oxidation of SiC in interior regions near unaltered ZrB_2-SiC (which was not accounted for in the calculation).

Figure 2.12 is a plot of equilibrium constants as a function of temperature for differing versions of the oxidation of SiC and ZrB_2, showing that all indicated reactions are highly favorable. The equilibrium constants are so large at all temperatures, that a buildup of product gas partial pressures to and exceeding ambient would not stop reactants from going toward products. It is reasonable to assume that in the gaseous environment within the SiC-depleted ZrB_2 region, that the partial pressure of oxygen is substantially lower than the ambient, as it is being consumed through oxidation and its supply is limited by diffusion through layers closer to the surface. In the reduction of metal oxides, plots such as Figure 2.12 can be used to specify the p_{O_2} for which certain metals will oxidize while other metal oxides will reduce. In this case; however, the equilibrium constants do not represent the same ratio of partial pressures, making such evaluations difficult.

The SiC-depleted ZrB_2 zone is seen ubiquitously for oxidation temperatures of 1700°C and above. Figure 2.13 shows the stability of reaction product $SiO_{2(l)}$ in contact with reactant $SiC_{(s)}$. If it assumed that a pressure within the SiC-depleted ZrB_2 layer cannot exceed atmospheric (since a bubble would otherwise form and burst), and equimolar amounts of SiO and CO gaseous products form, then as shown in the figure, $SiO_{2(l)}$ will react with SiC to form vapor phases above ∼1525°C. Thus for temperatures above this, any SiO_2 which forms immediately reacts with the SiC in contact with it to form gas phases which escape from the reaction zone. In contrast, oxidation of ZrB_2 forms B_2O_2 vapor and a zirconia scale; this scale impedes subsequent oxidation of the ZrB_2 beneath it. Hence, available oxygen preferentially attacks constantly-exposed SiC, rather than neighboring ZrB_2 grains
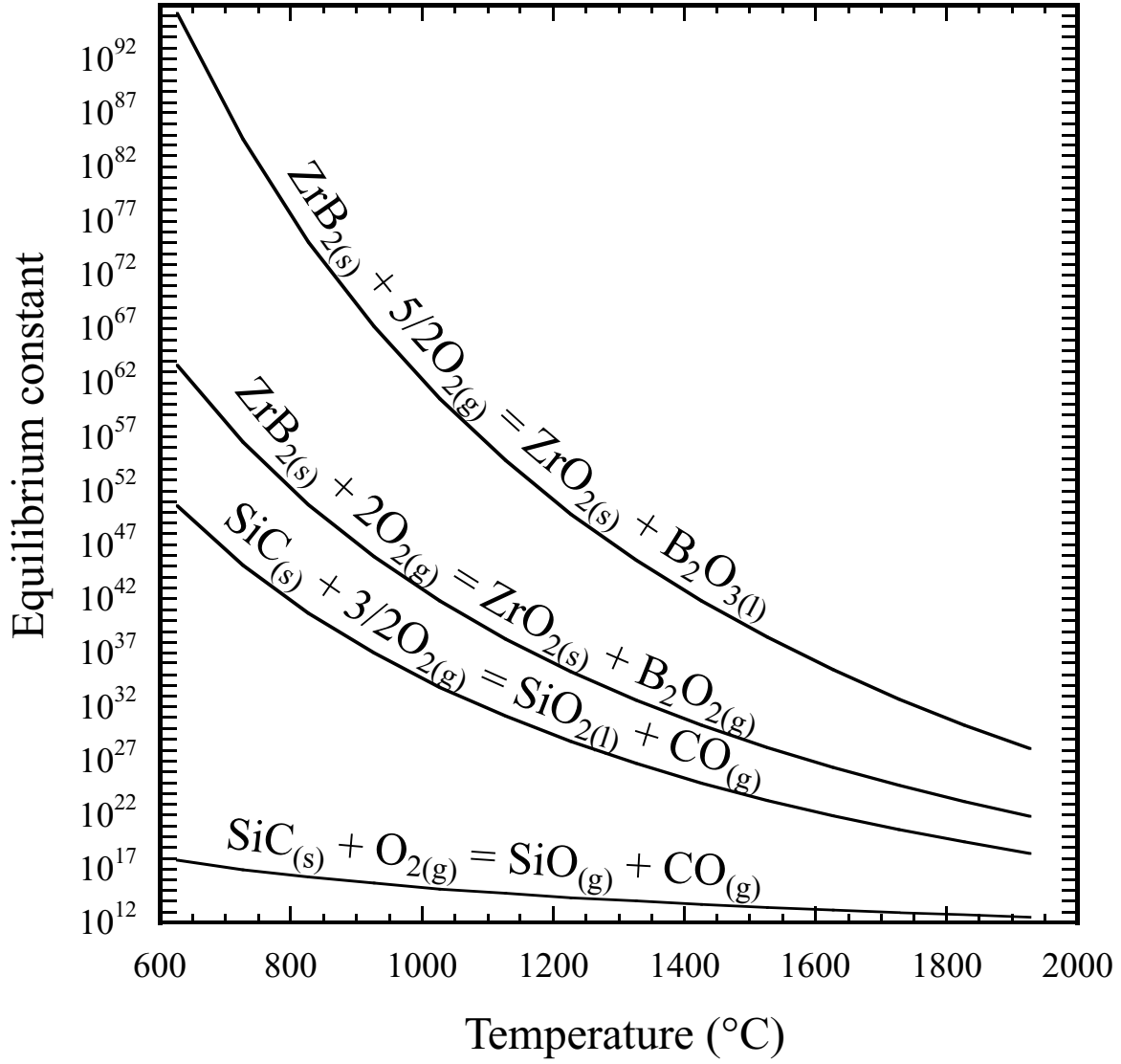
Figure 2.12: Equilibrium constant versus temperature as calculated by the expression $\Delta G^{\circ}_{\text{rxn}} = -RT \ln k_p$ where $\Delta G^{\circ}_{\text{rxn}}$ is the standard (1 bar) Gibbs energy of reaction, R is the gas constant, T is absolute temperature, and k_p is the equilibrium constant. $k_p = 1/p_{O_2^{5/2}}$, $k_p = p_{B_2O_2}/p_{O_2^2}$, $k_p = p_{CO}/p_{O_2^{3/2}}$, $k_p = p_{CO}p_{SiO}/p_{O_2}$, for the highest to lowest traces, respectively. Standard Gibbs energies of reactions were based on the Gibbs energies of formation of compounds [18].
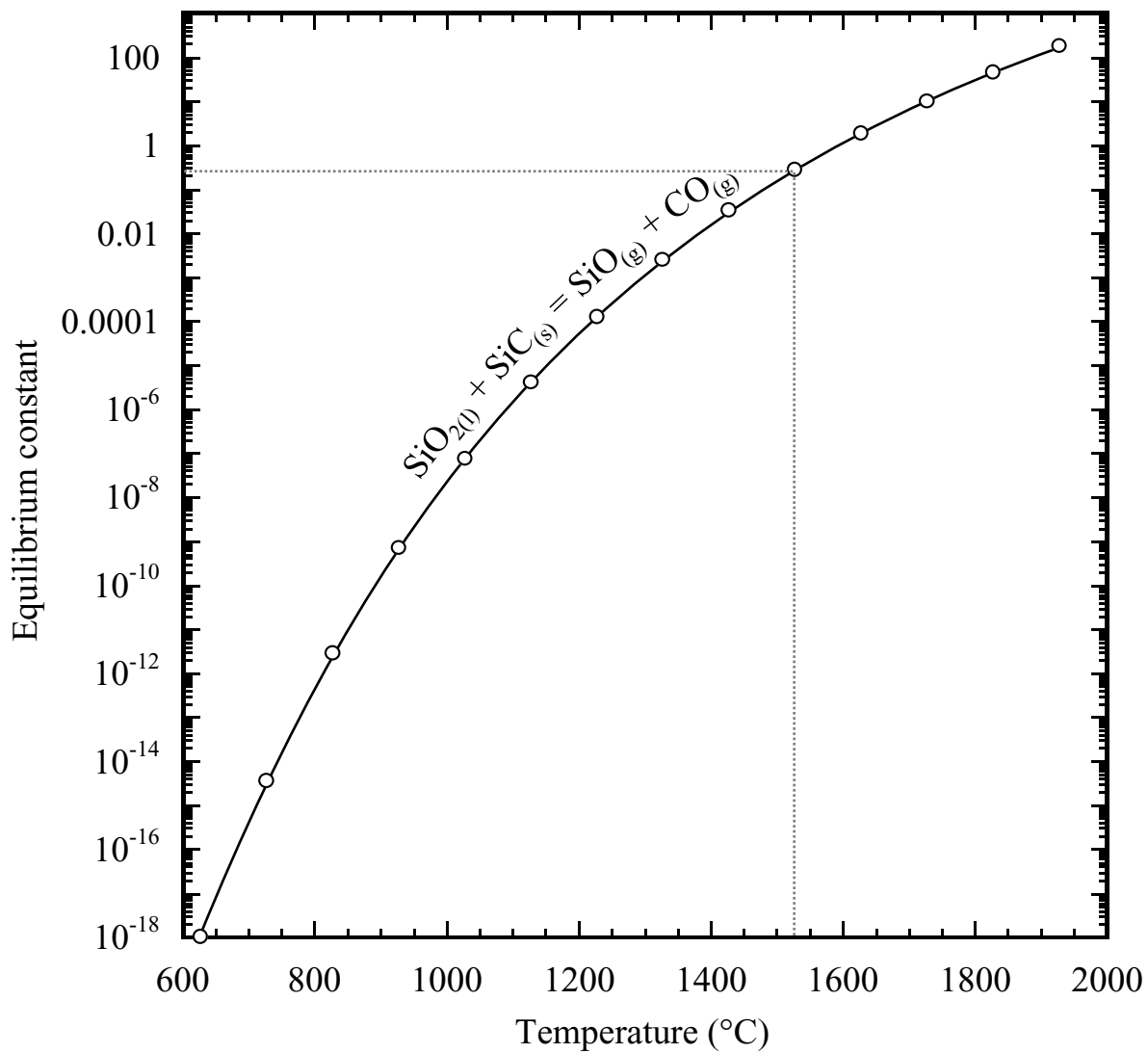
Figure 2.13: Equilibrium constant versus temperature for the indicated equilibria. For this reaction, $k_p = p_{CO}p_{SiO}$

50

(protected by even a thin layer of ZrO_2). This analysis is consistent with the observation that SiC-depleted ZrB_2 regions are not visually apparent until oxidation temperatures of $1700°C$ were used. The same result would be expected if the immediate oxidation product of SiC was $SiO_{(g)}$ rather than $SiO_{2(l)}$. Figure 2.14 shows that $SiO_{(g)}$ production is favored by high temperatures and low oxygen partial pressures. The extent to which $SiO_{2(l)}$ spontaneously decomposes to $SiO_{(g)}$ depends on the rate of escape of $SiO_{(g)}$ through the layers closer to the specimen exterior.

The formation of bubbles in the specimen with ~60 mol% SiC oxidized at $1900°C$, implying the formation of vapor pressures exceeding ambient, may be attributed to a number of contributing factors. Gaseous products of oxidation, e.g. $CO_{(g)}$ and $B_2O_{2(g)}$ are not thought to be a major contributor since these gases form only in equimolar quantities to the amount of oxygen consumed, and the oxygen partial pressure in these buried layers is interpreted to be quite low. Only if the diffusion of these gaseous products through layers closer to the surface is significantly hindered as compared to the diffusion of oxygen, would significant partial pressures of these reaction products form. A more significant contributer would be the volatilization of $B_2O_{3(l)}$ whose equilibrium vapor pressure is ~0.3 atm at $1900°C$. The high concentration of SiC would imbue relatively close proximity of SiC and $SiO_{2(l)}$ (since there is a vast SiC source near the surface, its consumption to form the passivating glass/liquid layer does not require much penetration into the specimen interior), and the lower viscosity of the fluid at this temperature would facilitate liquid migration to contact interior SiC, facilitating reaction. These condensed phase to gaseous phase reactions would form copious amounts of $SiO_{(g)}$ and $CO_{(g)}$.

V   Conclusions

The minimum SiC content for passivization in pore-free ZrB_2-SiC mixtures is between 15 and 30 mol% SiC. The passivating near-surface microstructure for isothermal heat-treatments at and above $1700°C$ consists of consecutive layers of a silicate liquid/glass, ZrO_2 infused with liquid/glass, ZrB_2 devoid of SiC, and then an unaltered ZrB_2-SiC microstructure. When more rapid oxidation is observed, a layer of zirconia and porosity is observed, which can be quite extensive. Use of ~6 mol% TaB_2 along with the ~28 mol% SiC resulted in what appeared to be thinner oxide passivating layers and equally good oxidation resistance. Bubbles observed in the glassy layer and their periodic bursting implied from thermogravimetry in the 60 mol% SiC specimen heat-treated at $1900°C$ indicate the buildup of product gases and/or condensed phase vapors which exceeded ambient pressure. The selective removal of SiC from near-surface ZrB_2-SiC microstructure was proposed to be the result of reaction products of SiC oxidation being unprotective to yet-unreacted SiC, as compared to reaction products of ZrB_2.

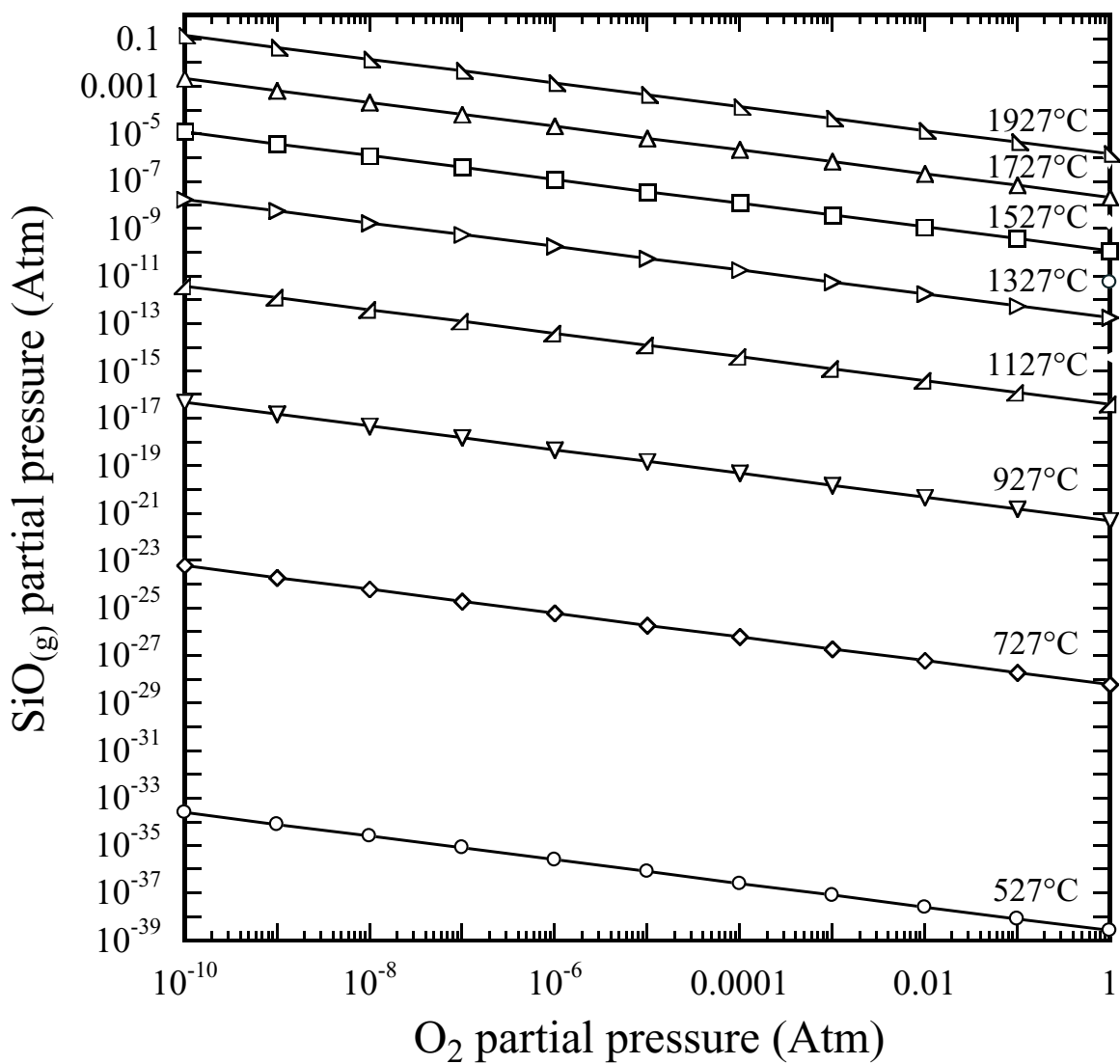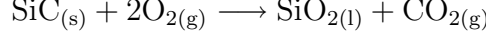# VI   Appendix

For the reactions
$$ZrB_{2(s)} + \frac{5}{2}O_{2(g)} \longrightarrow ZrO_{2(s)} + B_2O_{3(g)}$$
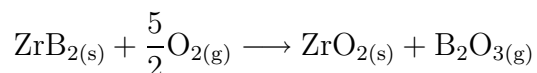
Figure 2.14: $SiO_{(g)}$ partial pressure as a function of oxygen partial pressure and temperature for the equilibria: $SiO_{2(l)} = SiO_{(g)} + (1/2)O_{2(g)}$.

and
$$SiC_{(s)} + 2O_{2(g)} \longrightarrow SiO_{2(l)} + CO_{2(g)}$$
it is assumed that boron oxide forms as an escaping gas and silica forms as a liquid/glass. These reaction stoichiometries dictate that the number of moles of ZrO_2 formed are equal to the number of moles of ZrB_2 consumed, $n_{ZrO_2} = n_{ZrB_2}$, and similarly $n_{SiO_2} = n_{SiC}$. Note that the latter equality holds even if the reaction produced CO as opposed to CO_2.

Let ΔM be the measured mass change after 100 min exposure to a given oxidation temperature. Then:
$$\Delta M = (M_{ZrO_2} - M_{ZrB_2}) + (M_{SiO_2} - M_{SiC})$$
where M_{ZrB_2} and M_{SiC} are the masses of zirconium diboride and silicon carbide converted, respectively, and M_{ZrO_2} and M_{SiO_2} are the masses of zirconia and silica produced, respectively. Letting W be the molar mass:
$$\Delta M = n_{ZrB_2}(W_{ZrO_2} - W_{ZrB_2}) + n_{SiC}(W_{SiO_2} - W_{SiC})$$
We define X_{SiC} as the mole fraction of SiC in the original ZrB_2-SiC composition, thus:
$$n_{SiO_2} = \frac{\Delta M}{\left(\frac{1}{X_{SiC}} - 1\right)(W_{ZrO_2} - W_{ZrB_2}) + (W_{SiO_2} - W_{SiC})} \tag{2.1}$$
Let ρ be the density and V' be the volume of oxide formed:
$$V' = \frac{n_{SiO_2}W_{SiO_2}}{\rho_{SiO_2}} + \frac{n_{ZrO_2}W_{ZrO_2}}{\rho_{ZrO_2}} \tag{2.2}$$
Given a disk geometry for the partially oxidized specimen of diameter d and height h, with a uniform oxide coating thickness of T:
$$V' = 2\pi \left(\frac{d}{2}\right)^2 T + (h - 2T)\left(\pi \left(\frac{d}{2}\right)^2 - \pi \left(\frac{d - 2T}{2}\right)^2\right) \tag{2.3}$$

The diameter d and and height h of the disk vary during oxidation since the densities of the consumed phases and the corresponding formed oxide phases are not the same. Let ΔV be the volume of products formed minus the volume of reactants consumed; that is, the change in volume of the disk. Recognizing the equivalence of moles of ZrB_2/ZrO_2 and SiC/SiO_2:
$$\Delta V = n_{SiC}\left(\frac{W_{SiO_2}}{\rho_{SiO_2}} - \frac{W_{SiC}}{\rho_{SiC}}\right) + n_{ZrB_2}\left(\frac{W_{ZrO_2}}{\rho_{ZrO_2}} - \frac{W_{ZrB_2}}{\rho_{ZrB_2}}\right) \tag{2.4}$$
If the dimensions of the disk before oxidation are d_0 and h_0, then after partial oxidation, the change in volume is:
$$\Delta V = \pi \left(\frac{d}{2}\right)^2 h - \pi \left(\frac{d_0}{2}\right)^2 h_0$$

Assuming that the thickness of oxide scale forming on all surfaces is the same, then the change in linear dimensions from oxidation in the axial and radial directions would be the same: $d - d_0 = h - h_0$, thus:
$$\Delta V = \frac{\pi}{4}\left((h - h_0 + d_0)^2 h - d_0^2 h_0\right) \tag{2.5}$$

Equation 2.2 (inserting in equation 2.1 and the definition of mole fraction) may be used to determine the volume of oxide formed. Inserting this into equation 2.3, along with calculated values of d and h from equations 2.4 and 2.5 will yield T through numerical solution.

Bibliography

[1] F. Peng, Y. Berta, and R. F. Speyer, "Effect of SiC, TaB$_2$ and TaSi$_2$ Additives on the Isothermal Oxidation Resistance of Fully Dense Zirconium Diboride," *J. Mater. Res.,* **24** [5] 1855-1867 (2009).

[2] R. F. Speyer, "Effect of SiC, TaB$_2$ and TaSi$_2$ Additives on the Isothermal Oxidation Resistance of Fully Dense Zirconium Diboride," Presented at the Workshop on Aerospace Materials for Extreme Environments," Aug 5, 2009.

[3] S. N. Karlsdottir, J. W. Halloran, and A. N. Grundy, "Zirconia Transport by Liquid Convection During Oxidation of Zirconium Diboride-Silicon Carbide," *J. Am. Ceram. Soc.,* **91** [1] 272-277 (2008).

[4] E. J. Opila, M. C. Halbig, "Oxidation of ZrB$_2$-SiC," *Elec. Chem. Soc. Proc.,* **12** 221-228 (2002).

[5] A. Rezaie, W. G. Fahrenholtz, and G. E. Hilmas, "Evolution of Structure During the Oxidation of Zirconium Diboride-Silicon Carbide in Air up to 1500°C," *J. Europ. Ceram. Soc.,* **27** 2495-2501 (2007).

[6] W. G. Fahrenholtz, "Thermodynamic Analysis of ZrB2-SiC Oxidation: Formation of a SiC-depleted Region," *J. Am. Ceram. Soc.,* **90** [1] 143-148 (2007).

[7] M. Opeka, I. Talmy, J. Zaykoski, "Oxidation-based Materials Selection for 2000°C $^+$ Hypersonic Aerosurfaces: Theoretical Considerations and Historical Experience," *J. Mater. Sci.,* **39** 5887-5904 (2004).

[8] A. R. Rezaie, W. G. Fahrenholtz, and G. E. Hilmas, "Oxidation of Zirconium Diboride-Silicon Carbide at 1500°C in a Low Partial Pressure of Oxygen, *J. Am. Ceram. Soc.,* **89** [10] 3240-45 (2006).

[9] J. Han, P. Hu, X. Zhang, and S. Meng, "Oxidation Behavior of Zirconium Diboride-Silicon Carbide at 1800°C," *Scripta Materialia,* **57** 825-828 (2007).

[10] W. Han, P. Hu, X. Zhang, J. Han, and S. Meng, "High-Temperature Oxidation at 1900°C of ZrB$_2$-xSiC Ultrahigh-Temperature Ceramic Composites," *J. Am. Ceram. Soc.* **91** [10] 3328-3334 (2008).

[11] S. N. Karlsdottir, and J. W. Halloran, "Rapid Oxidation Characterization of Ultra-High Temperature Ceramics," *J. Am. Ceram. Soc.,* **90** [10] 3233-3238 (2007).

[12] P. Hu, X. Zhang, J. Han, X. Luo, and S. Du, "Effect of Various Additives on the Oxidation Behavior of ZrB_2-Based Ultra-High-Temperature Ceramics at 1800°C," *J. Am. Ceram. Soc.*, **93** [2] 345349 (2010).

[13] X. Zhang, P. Hu, J. Han, and S. Meng, "Ablation Behavior of ZrB_2-SiC Ultra High Temperature Ceramics under Simulated Atmosphere Re-entry Conditions," *Composites Science and Technology*, **68** 1718-1726 (2008).

[14] F. Monteverde, R. Savino, M. D. S. Fumo, and A. D. Maso, "Plasma Wind Tunnel Testing of Ultra-High Temperature ZrB_2-SiC Composites under Hypersonic Re-Entry Conditions," *J. Euro. Ceram. Soc.*, **30** 2313-2321 (2010).

[15] F. Monteverde, and R. Savino, "Stability of Ultra-High Temperature ZrB_2-SiC Ceramics Under Simulated Atmospheric Re-Entry Conditions," *J. Euro. Ceram. Soc.*, **27** 4797-4805 (2007).

[16] J. Han, P. Hu, X. Zhang, S. Meng, and W. Han, "Oxidation-resistant ZrB_2-SiC Composites at 2200°C," *Composites Science and Technology*, **68** 799-806 (2008).

[17] R. F. Speyer, Thermal Analysis of Materials, Marcel Dekker, New York, 1994.

[18] M. W. Chase, Jr., "NIST-JANAF Thermochemical Tables", *J. Phys. Chem. Ref. Data, Monograph 9*, 4th Ed., American Institute of Physics, Woodbury, NY, 1998.

Chapter 3

Isothermal Oxidation of HfB$_2$ - 60% SiC at 1600-1800°C

I Introduction

Hafnium diboride (HfB$_2$) is a ultra-high temperature ceramic (UHTC), having similar in properties to zirconium diboride (ZrB$_2$), such as high melting point ($\geq$ 3000°C) and high thermal conductivity. Microstructures with it as the major phase are good candidates for leading surfaces for atmospheric reentry. SiC is the most commonly used second phase for oxidation passivation; a compact layer of silicate glass forms, acting as an oxygen diffusion barrier.

Oxidation kinetics studies on this material have been carried out in static air up to $\sim$1630°C (maximum temperature of common MoSi$_2$ heating element furnaces) [1]-[3]. Hinze et al. [1] showed that the oxidation rate of ZrB$_2$ - 20 vol% SiC was higher by a factor of four than HfB$_2$ - 20 vol% SiC during isothermal oxidation at 1400°C. From 1350-1550°C, oxidation of HfB$_2$ - 20 vol% SiC was parabolic and diffusion of oxygen through a liquid silicate surface coating was attributed to be the rate-limiting step. At lower oxygen partial pressures (generated by Ar-O$_2$ mixtures), active oxidation was observed as SiC oxidized to SiO$_{(g)}$. A layer of HfB$_2$ surrounded by porosity was observed in which SiC was preferentially attacked and removed as SiO$_{(g)}$. At still lower oxygen partial pressures generated by a CO$_2$-CO mixture, this region was not observed because the CO overpressure suppressed the SiC oxidation reaction (SiC$_{(s)}$ + O$_{2(g)}$ = SiO$_{(s)}$ + CO$_{(g)}$). Monteverde [2] showed that after constant heating rate thermogravimetry in air to 1450°C, a HfB$_2$ - 19.5 vol% SiC composition was more resistant to oxidation than a HfB$_2$/ZrB$_2$ - 19.5 vol% SiC composition (with an equimolar ratio of Zr to Hf). This was also found to be the case after isothermal oxidation at 1600°C for up to 60 min. Klein et al. [3] found that a Si$_3$N$_4$ - 27 vol% HfB$_2$ composition was oxidation resistant under constant heating rate studies up to 1400°C, with a protective silicate surface coating observed to form.

Carney [4] investigated the oxidation behavior of HfB$_2$ - 20 vol% SiC (fabricated through

spark plasma sintering) after 1 h isothermal exposures in the 1400-2000°C range. Specimen weight gain was modest up to 1800°C, but then accelerated after 1900°C and again after 2000°C exposures. At and above 1800°C oxidation exposures, a substantial fraction of SiO_2 oxidation product liquid was measured to have flowed from the specimen to its zirconia crucible.

Gasch et al. [5] studied hot-pressed HfB_2 - 20 vol% SiC exposed to arc jet testing. Such an ionized gas environment was argued to be a closer approach to service conditions for these materials, though the author pointed out that a higher percentage of air molecules are dissociated in an arc jet environment. After exposure to arc jet streams of approximately 1800 or 2400°C (two 10-minute durations), layers formed which were all devoid of silica: porous HfO_2, SiC-depleted HfB_2, and then the HfB_2-SiC interior.

In this investigation, the oxidation resistances of pore-free, pressureless-sintered, and post-HIPed HfB_2-SiC based compositions were characterized based on isothermal thermogravimetry. These results are compared against those of a similar study on ZrB_2-SiC composiitons.

II   Experimental Procedure

Commercially-available powders were used as raw materials (Table 3.1). The d_{50} particle

Table 3.1: Raw Material Powder Characteristics

	Phases	Particle Size	Supplier
HfB_2	HfB_2	< 43 μm	Grade B, H. C. Starck, GmbH
B_4C	stoichiometric B_4C	$d_{50} = 0.8$ μm	Grade HS, H. C. Starck, GmbH
SiC	α-SiC	$d_{50} = 0.88$ μm	Grade 8S490NDP, Superior Graphite, Chicago, IL

size of the HfB_2 powder was deemed too large for pressureless sintering; sedimentation-based selection was used to obtain finer particles: Powders were dispersed in ethanol using an ultrasonicator (FS-14 Solid State Ultrasonicator, Fisher Laboratory Equipment Division, Pittsburgh, PA) for 10 min. The mixture was allowed to settle in ethanol for ∼40 min. The top 7 cm (of a total column height of 14 cm) of fluid was then extracted using a pipette. Based on laser particle size analysis (Model LS 13320, Beckman Coulter, Fullerton, CA), decanted particles had a d_{50} of 0.96 μm. The decanted suspensions were dried in a beaker on a hot-plate.

The compositions of synthesized powder mixtures were (in mol%): HfB_2 - 7.27% B_4C - 15.35% SiC, HfB_2 - 6.04% B_4C - 29.70% SiC, and HfB_2 - 3.53% B_4C - 58.92% SiC. Fabrication of theoretically-dense specimens followed a procedure identical to our recent work on ZrB_2-based UHTCs [6]. All specimens after uniaxial pressing, cold isostatic pressing, thermolysis heat-treatment, sintering heat-treatment, and hot isostatic pressing (HIPing), were characterized via the Archimedes method to have achieved their theoretical densities (based on the rule mixtures of as-batched compositions). All of the surfaces of the post-HIPed samples were ground away and the resulting pellet dimensions were measured with calipers, from which surface areas were calculated. Pellets were ∼5.3 mm in diameter and 3-4 mm in height. The oxidation behaviors were then investigated using thermogravimetric analysis as

described in recent work [6]. Hafnia crucibles (green CNC machined out of pressed blanks of sinter-grade powder, and then sintered) were in contact with the specimens.

Crystalline phases in the samples were identified using X-ray diffraction (XRD). Diffraction patterns of oxidized specimens were taken from the oxidized surfaces. Microstructures of oxidized samples were investigated using scanning electron microscopy and energy dispersive spectrometry. For displayed micrographs, specimen cross-sections were taken through fracture. Specimens were coated with gold (sputtering for 2 min) to form a conductive surface.

III Results and Discussion

During sintering heat-treatments of powder compacts in a flowing argon atmosphere, slower cooling rates from the sintering soak temperature were required to avoid thermal shock of the various compositions. None of the samples containing $\sim$15% SiC and $\sim$30% SiC survived during raising into the hot zone of the thermogravimetry oxidation furnace; specimens were observed propelling out of their hafnia crucibles, even when slow loading speeds ($\sim$1 cm/min) were attempted. Only the high SiC-containing composition (58.92%) samples survived, and only when slow insertion rates were used. This is in contrast to our previous work with analogous ZrB_2 - SiC compositions which showed no thermal shock sensitivities during sintering or oxidation heat-treatments [6]. The coefficients of thermal expansion of ZrB_2 and HfB_2 have been reported to be similar, $\sim 6 \times 10^{-6}$ $^{\circ}C^{-1}$ [10], so these results are unexpected.

For the as-fabricated post-HIPed specimen cross sections, HfB_2 was detected by XRD but the B_4C additive was not. SiC was only detected when added in the two higher concentrations. From the oxidized surfaces, only the monoclinic form HfO_2 was detected. HfB_2 was detected (via x-rays penetrating through the oxide layers) after oxidation heat-treatment at 1600 and 1700°C, but not from the specimen oxidized at 1800°C. SiC was not detected from XRD of oxidized surfaces.

Figure 3.1 shows TG traces of HfB_2 - 58.92 mol% SiC oxidized at 1600, 1700, and 1800°C. These traces were selected among three for each temperature as those being most representative. At 1600°C, there was an initial weight loss over $\sim$20 min, after which, the specimen weight remained constant over time. The 1700°C TG trace showed a similar behavior, but the oxidation resistance as indicated by weight change was less extensive than at 1600°C. Periodic jumps in specimen weight corresponding to ruptures of the liquid surface layer [6] were recorded in the TG traces when specimens were oxidized at 1800°C.

The oxidation resistance (as indicated by resistance to weight gain) of HfB_2 - 58.92 mol% SiC was equivalent to ZrB_2 - 58.92 mol% SiC at 1600°C, but was greater at 1700°C. Periodic disruptions in the HfB_2 - 58.92 mol% SiC 1800°C trace are apparent, which are not seen for the analogous ZrB_2 - 58.92 mol% SiC trace. Such disruptions shifted more rapid weight gain trends which, without the step-function decreases in weight, would have visually implied lower oxidation resistance than ZrB_2 - 58.92 mol% SiC at this temperature.

After isothermal oxidation at 1600°C, a $\sim$10 μm thick glassy layer is observed with embedded rounded particles of HfO_2 (Figure 3.2). The hafnia particles are in a relatively higher concentration at the base of this layer. Beneath this layer is un-transformed HfB_2-SiC.

The most intense EDS peaks of Si and Hf overlap. Hafnium can be unequivocally identified by additional peaks at higher keV. Si is identified by only a single peak; hence, its presence
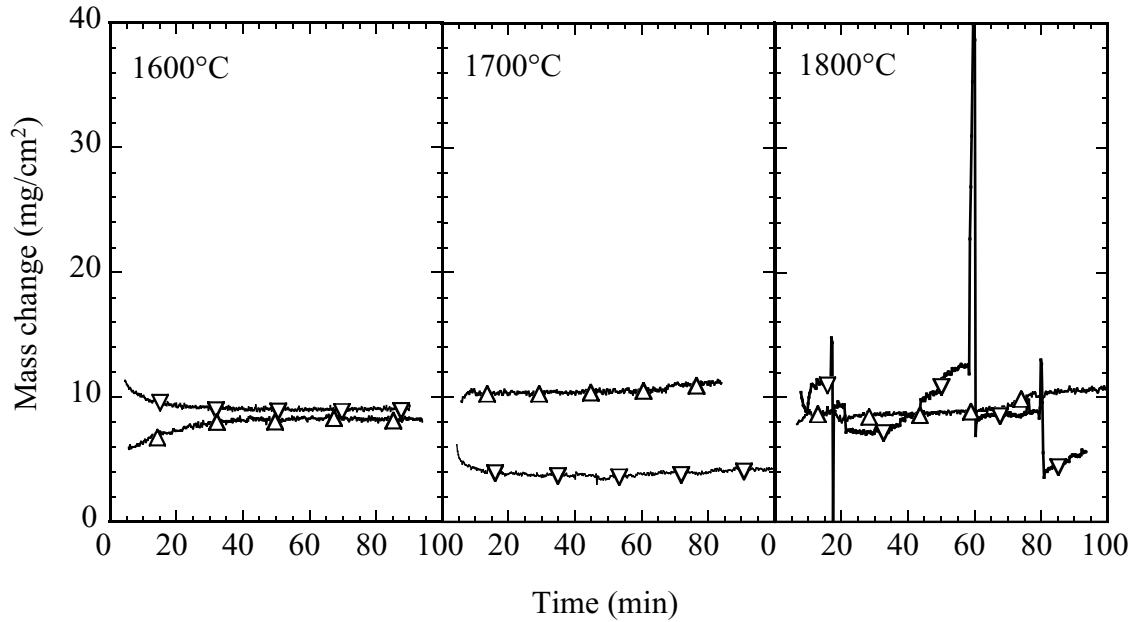
Figure 3.1: Compilation of thermogravimetry traces for various isothermal exposures to flowing dry air at the indicated temperatures. Downward triangle: HfB_2 - 58.92 mol% SiC; upward triangle: ZrB_2 - 58.92 mol% SiC [6]. In this figure, symbols are used only to identify traces; each TG trace is made up of ~1000 data pairs.

is only definitively indicated by the absence of the extra Hf peaks.

After exposure to 1700°C, a silicate glassy layer appears with less apparent immersed hafnia (Figure 3.3). A not fully distinct region beneath the glassy layer consists of HfO_2 and silicate glass, along with an indication by EDS that un-transformed SiC is retained. Beneath this region is one in which some porosity is implied at locations in which SiC was previously located, but complete removal of SiC in a distinct layer is not apparent.

After isothermal oxidation at 1800°C, the reaction layers are considerably more coarse and well-defined (Figure 3.4). Underneath a silicate liquid/glass layer is a mixture of HfO_2 crystals and a silicate phase. Under this layer is a porous region of HfB_2 depleted of SiC.

The thicknesses of the various layers for HfB_2 - 58.92 mol% were less coarse than ZrB_2 - 58.92 mol% isothermally oxidized at 1600 and 1700°C. However, these layers were coarser, most notably the SiC-depleted region, for HfB_2 - 58.92 mol% oxidized at 1800°C. The corresponding copious amounts of B_2O_3, CO, and SiO gaseous reaction products resulted in bubble formation and periodic rupture of the silicate liquid surface coating, in turn forming short circuit paths for oxygen attack. This occurred in ZrB_2 - 58.92 mol% only after oxidation at 1900°C.

IV   Conclusion

HfB_2-SiC compositions suffered thermal shock which prohibited oxidation thermogravimetry experiments, with the exception of the SiC-rich composition of HfB_2 - 58.92 mol%. This
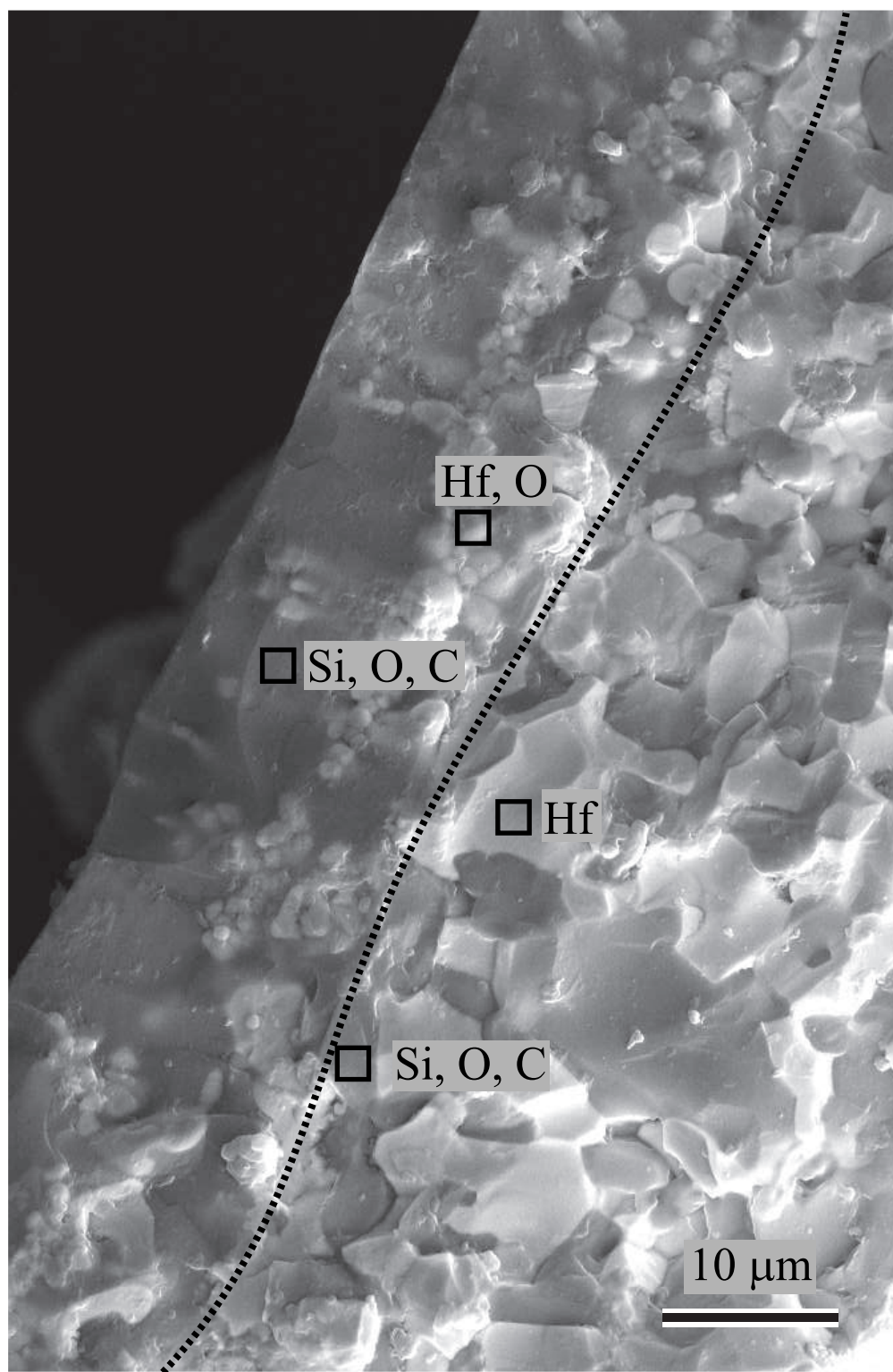
Figure 3.2: SEM micrograph of fracture-surface cross-section of HfB_2 - 58.92 mol% SiC oxidized at 1600°C for ~90 min. Based on compositional contrast and EDS results, light-shaded interior regions are HfB_2 and darker-shaded regions are SiC. Above and to the left of the dashed line is interpreted to be a silicate liquid/glass with embedded HfO_2 particles. Below and to the right of the dashed line is un-transformed HfB_2-SiC.
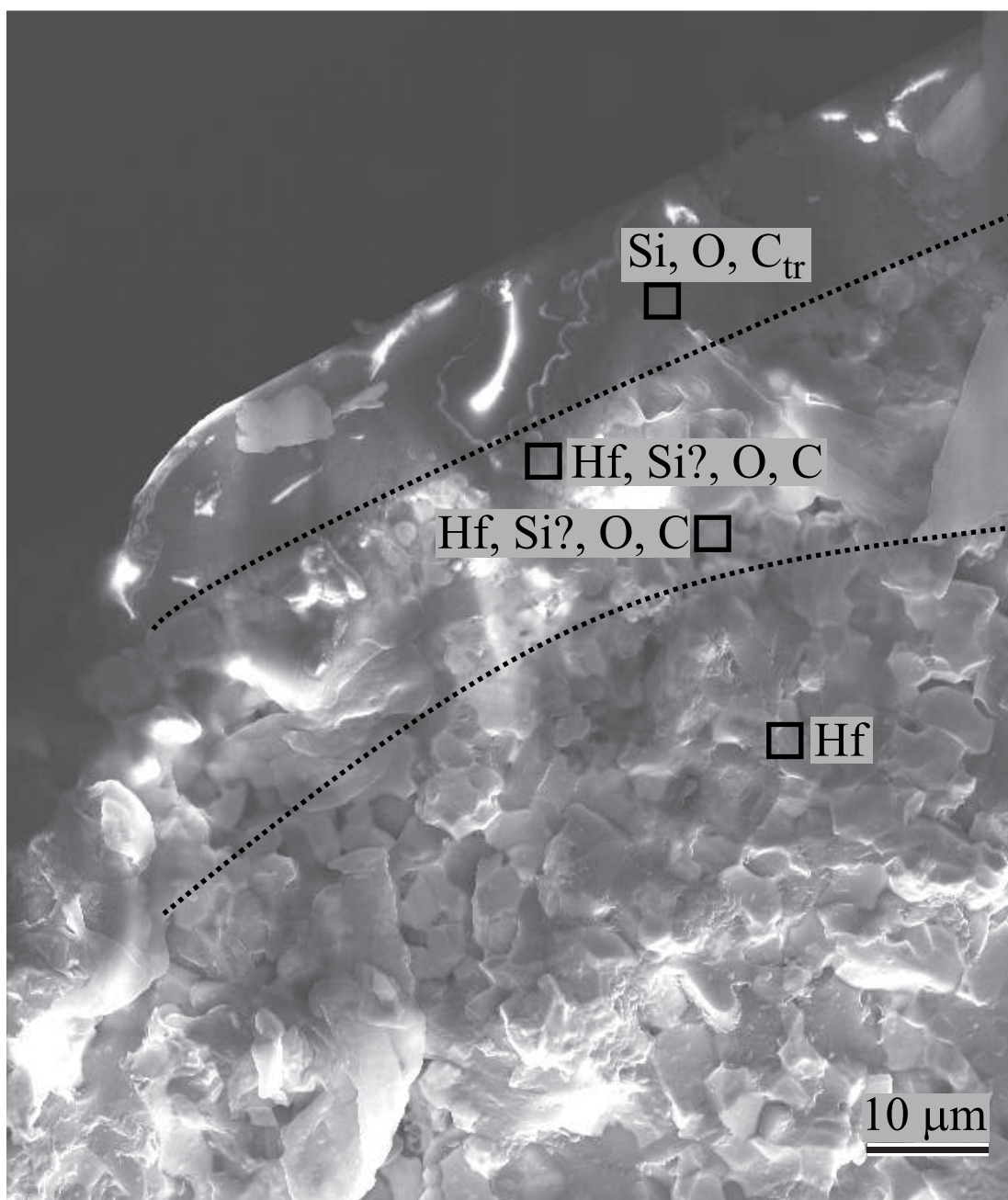
Figure 3.3: SEM micrograph of HfB_2 - 58.92 mol% oxidized at 1700°C for ~90 min. Above the upper dashed line is silicate liquid/glass with some immersed HfO_2. Between the dashed lines is a transition region containing hafnium oxide/diboride and silicon oxide/carbide. Below the lower dashed line is un-transformed matrix phases with some SiC extracted.
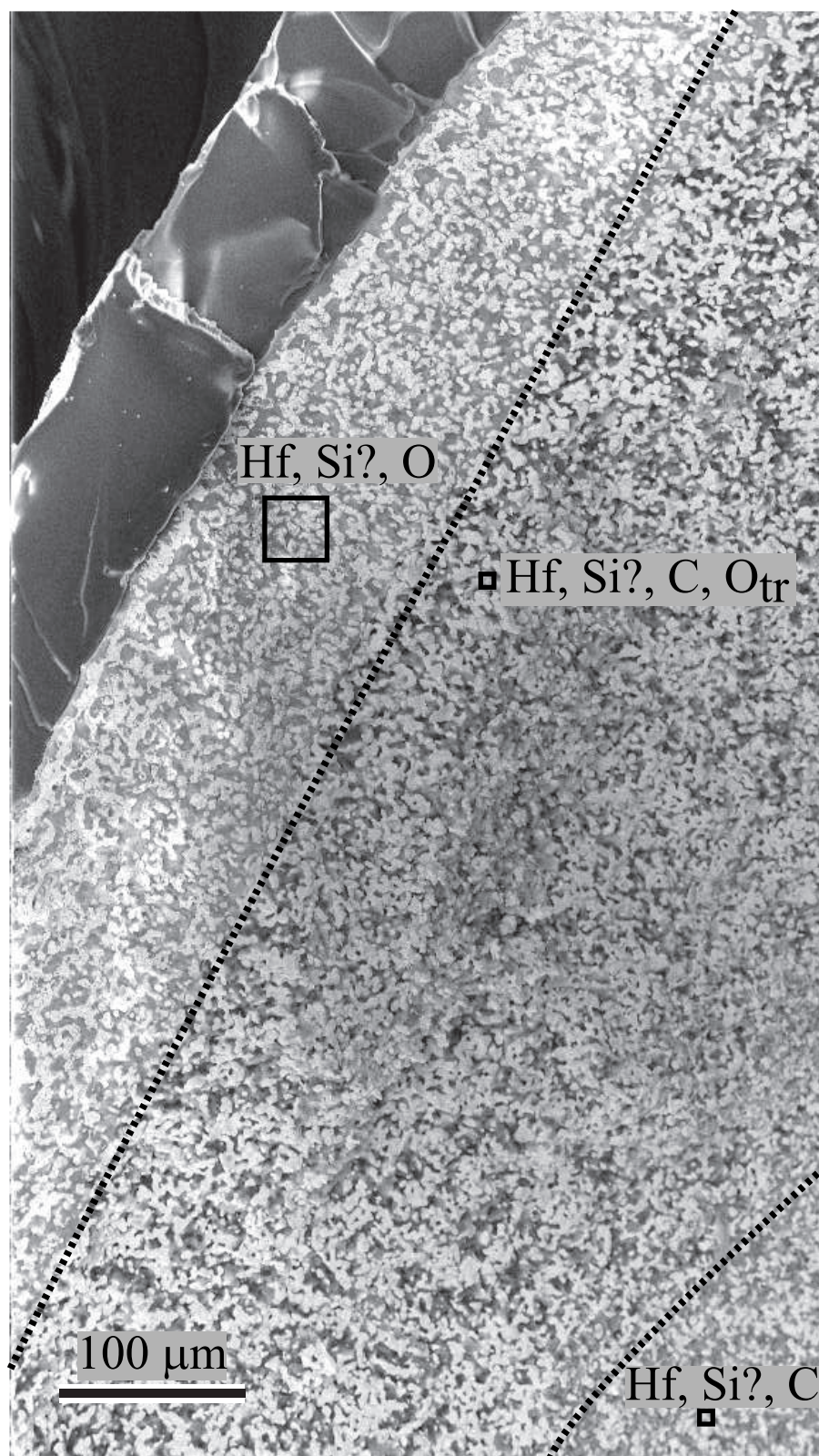
Figure 3.4: SEM micrograph of HfB$_2$ - 58.92 mol% oxidized at 1800°C for ~90 min. Layers are relatively coarse and visibly distinct: a silicate glass/liquid with few HfO$_2$ inclusions, above a region of HfO$_2$ and SiO$_2$. To the right and below the long dashed line is a region of HfB$_2$ partially depeted of SiC. To the right and below the lower dashed line are un-reacted matrix phases.

composition showed higher oxidation resistance than ZrB_2 - 58.92 mol% at 1700°C, but less oxidation resistance at 1800°C (90 min soaking periods) where gas bubble rupturing of the silicate glassy layer was observed in thermogravimetry traces. SEM micrographs from the specimen oxidized at 1800°C showed distinct layers of silicate liquid/glass, HfO_2 immersed in silicate liquid/glass, SiC-depleted HfB_2, and an unreacted HfB_2-SiC interior.

Bibliography

[1] J. W. Hinze, W. C. Tripp, H. C. Graham, "The High-Temperature Oxidation Behavior of a HfB_2 + 20 v/o SiC Composite," *J. Electrochem. Soc. Bull.,* **122** [9] 1249-1254 (1975).

[2] F. Monteverde, "The Thermal Stability in Air of Hot-pressed Diboride Matrix Composites for Uses at Ultra-high Temperatures," *Corr Sci*, **47** [8] 2020-2033 (2005).

[3] R. Klein, M. Desmaison-Brut, J. Desmaison, L. Mazerolles, and M. F. Trichet, "High-Temperature Oxidation Behavior of Hot Isostatically-Pressed Si_3N_4-HfB_2 Ceramic Composite," *Mater. Sci. Forum*, **461-464** 849-856 (2004).

[4] C. M. Carney, "Oxidation Resistance of Hafnium Diboride - Silicon Carbide from 1400 to 2000°C," *J. Mat. Sci.*, **44** [20] 5673-5681 (2009).

[5] M. Gasch, D. Ellerby, E. Irby, S. Beckman, M. Gusman, and S. Johnson, "Processing, Properties and Arc Jet Oxidation of Hafnium Diboride/Silicon Carbide Ultra High Temperature Ceramics."*J. Mater. Sci.*, **39** [19] 5925-5937 (2004).

[6] F. Peng, G. VanLaningham, and R. F. Speyer, "Thermogravimetric Analysis of the Oxidation Resistance of ZrB_2-SiC and ZrB_2-SiC-TaB_2-based Compositions in the 1500-1900°C Range," *J. Mater. Res.,* **26** [1] (2011).

[7] R. Karell, J. Kraxner, and M. Chromcikova, "Properties of Selected, Zirconia Containing Silicate Glasses," *Ceramics-Silikaty,* **50** [2] 78-82 (2006).

[8] J. Han, P. Hu, X. Zhang, and S. Meng,"Oxidation Behavior of Zirconium Diboride-Silicon Carbide at 1800°C," *Scipta Materialia,* **57** [9] 825-828 (2007).

[9] W. Han, P. Hu, X. Zhang, J. Han, and S. Meng,"High-Temperature Oxidation at 1900°C of ZrB_2-xSiC Ultrahigh-Temperature Ceramic Composites," *J. Am. Ceram. Soc.,* **91** [10] 3328-3334 (2008).

[10] G. V. Samsonov and I. M. Vinitskii, *Handbook of Refractory Compounds*, Plenum Press, 1980.

Chapter 4

Thermal Conductivity of ZrB$_2$-SiC-B$_4$C Compositions from 25-2000°C

I Introduction

Leading edges for space re-entry and hypersonic aviation are exposed to extreme heating via friction with the atmosphere. Ultra-high temperature ceramics such as ZrB$_2$ are favored candidates for these surfaces since they are highly refractory, having melting temperatures in excess of 3000°C. They have a relatively high emissivity to efficiently dissipate (through radiation) the heat load to the cold surrounding ambient. They also have relatively high thermal conductivities so that heat can be conducted to a wider surface area which can in turn be radiated away. ZrB$_2$ is generally mixed with SiC in a two-phase microstructure which forms a passivating silicate surface layer via high temperature surface oxidation. Boron carbide is typically added as a sintering aid. Measurements of the thermal conductivities of three compositions of such multi-phase mixtures is the focus of this study.

Thermal conduction in dielectric solids occurs by anharmonic waves, referred to as phonons, superimposed upon lattice vibrations. Conductive solids have the additional heat transfer mechanism of electron motion. Figure 4.1 [1] shows example thermal conductivity data for a variety of electrical conductors and dielectrics. For the typical dielectric, with rising temperature above zero Kelvin, thermal conductivity increases as T^3, reaching a maximum well below room temperature [2]. This maximum is limited by scattering of phonons with microstructural features which disrupt the periodicity of the lattice, e.g. dislocations and the strain fields around them, grain boundaries, and porosity. The temperature of the maximum is related to the Debye temperature, which is proportional to the maximum in the distribution of standing wave vibration frequencies. Since the Debye temperature increases with melting point and elastic modulus, diamond thermal conductivity reaches its maximum at a comparatively higher temperature. As a result, diamond has the highest known thermal
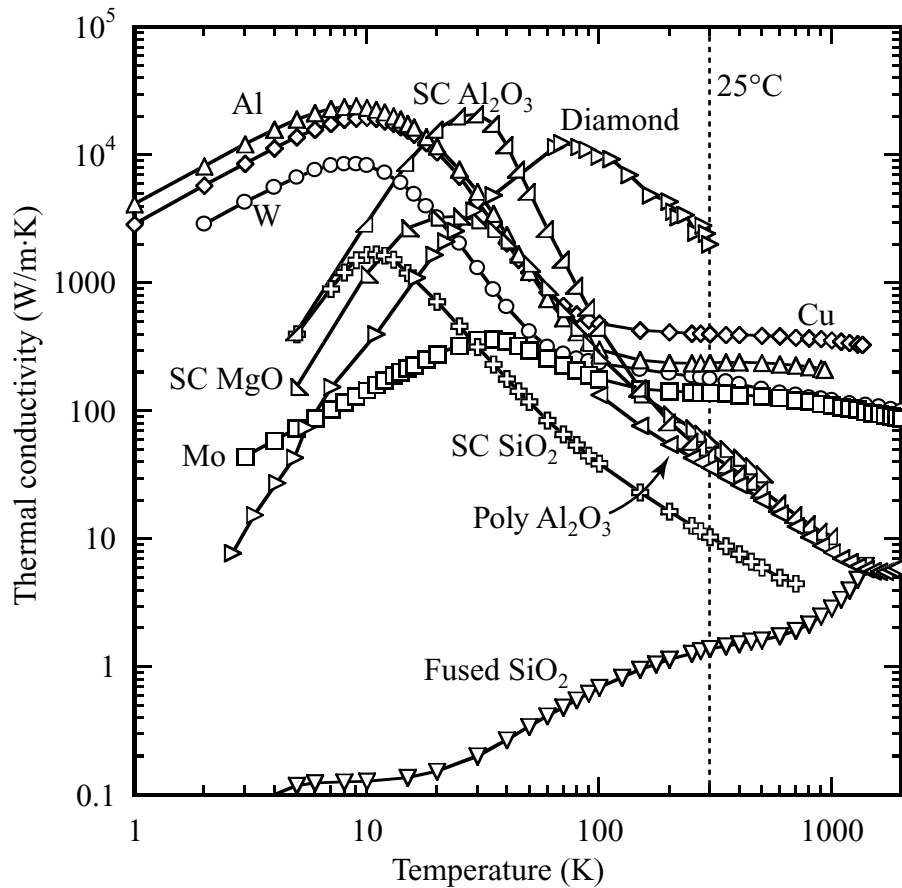
Figure 4.1: Thermal conductivities of various solids. SC indicates single crystal, "poly" indicates poly-crystalline. The metals shown are polycrystalline. Thermal conductivity data are based on the reference's recommended values determined from a critical review of a compilation of literature values, with the exception of the data for diamond, which is from a single source [1].

conductivity at room temperature.

At low temperatures, the concentration of generated phonons is low, hence there is a long mean-free path between interactions. This mean-free path decreases with increasing temperature; the thermal conductivity maximum represents the point at which the phonon mean free path is of the same order of magnitude as scattering from microstructural imperfections. As temperature is increased above this maximum, the thermal conductivity decrease is proportional to $1/T$ as the phonon-phonon scattering mean-free-path continues to decrease. The change in thermal conductivity with temperature tends to decrease to slopes below those predicted by $1/T$, as the phonon-phonon mean free path reaches atomic scale dimensions [2]. Other factors (negatively) affecting the thermal conductivity of dielectrics are the extent of solid solution and complexity of structure [3]. At the extreme, fused silica, having no lattice periodicity, has a very low thermal conductivity. Its rise with increasing temperature is from radiation contributions to heat transfer.

The electrically-conductive solids exhibit a similar maximum in thermal conductivity at cryogenic temperatures; however, at and above ~100 Kelvin, thermal conductivity is rel-

atively constant with increasing temperature, making electrically-conductive solids significantly more thermally conductive than the dielectrics (with the exception of diamond) at temperatures above room temperature.

II Experimental Procedure

Commercially-available ZrB_2 (Grade B, $d_{50} = 2.20$ μm, H. C. Starck, GmbH), α-SiC (Grade 8S490NDP, $d_{50} = 0.88$ μm, Superior Graphite, Chicago, IL), and B_4C (Grade HS, $d_{50} = 0.8$ μm, H. C. Starck) powders were used for raw materials. The compositions of synthesized powder mixtures are given in Table 4.1. Powders were ethanol-washed, and then mixed

Table 4.1: Sample Compositions

Code	Mole Percent			Volume Percent			Mass Percent		
	ZrB_2	B_4C	SiC	ZrB_2	B_4C	SiC	ZrB_2	B_4C	SiC
11SiC	77.39	7.27	15.34	80.36	8.92	10.72	89.57	4.12	6.31
22SiC	64.25	6.04	29.70	70.32	7.82	21.87	82.63	3.80	13.57
49SiC	37.55	3.53	58.92	46.15	5.13	48.72	62.36	2.87	34.77

in aqueous suspension with binder, dried, screened, uniaxially pressed into cylindrical pellets, cold isostatically pressed, and then exposed to thermolysis, sintering, and hot isostatic pressing heat (and pressure) treatment steps to form fully dense multi-phase bodies. This synthesis methodology is described in detail in our previous work [4, 5]. All HIPed specimens were 100% dense based on theoretical densities calculated from the rule of mixtures. The specimens were 12.7 mm in diameter by 2.0-2.1 mm in thickness. They were subsequently machined (Advanced Ceramic Machining, Tucson, AZ) to reach the specifications for diameter, width, and parallelness (within 0.025 mm) for thermal diffusivity measurements.

Thermal diffusivity was measured by the flash method using a Netzsch LFA 427 instrument, following the "Standard Test Method for Thermal Diffusivity by the Flash Method" standard ASTM E1461-01. The principle of the measurement is to irradiate (neodymium YAG laser, 1.06 μm) one radial face of the specimen with a short burst of energy (0.3-1.2 ms pulse width). An infrared pyrometer (InSb IR detector) measures the back face temperature, which quickly rises from the ambient temperature (established with a surrounding furnace, feedback controlled via a thermocouple). If the specimen is adiabatic with respect to its surroundings during the time period of the experiment, then the back face temperature would rise to a saturation temperature as temperature equilibrated throughout the part (generally 0.5-2°C). In one embodiment, the time required to reach the mid-point in temperature between the starting ambient temperature and the saturation temperature, $t_{1/2}$ would be measured from the data. If it was further assumed that the energy pulse time period was negligible compared to $t_{1/2}$, then the Parker [6] expression may be used to determine the thermal diffusivity:

$$D = \frac{0.1388a^2}{t_{1/2}}$$

where a is the specimen thickness.

In this work, the above assumptions were not made; rather, the software accounted for radial and axial heat loss and the effect of a finite pulse period [7, 8]. A non-linear regression routine was used, fitting to the entire time-temperature curve ($\sim$2000 points), adjusting both diffusivity and loss factor to best fit the data.

All the samples were coated with approximately 10 μm graphite to improve the absorption of radiation. Samples of each of the three compositions were evaluated at 25, 400, 800, 1200, 1600, and 1950°C, with some variation, with five measurements made at each temperature. Standard deviations are indicated as ± values in thermal diffusivity tabulations. Fluctuations in temperatures for these measurements were within 1.5°C.

III   Results and Discussion

Table 4.2 and Figure 4.2 show the results of the laser flash thermal diffusivity measurements

Table 4.2: Thermal Diffusivities Measured by the Laser Flash Method

Composition Designation	Temperature (°C)	Thermal Diffusivity ± Standard Deviation (mm²/s)
11SiC	25	36.4 ± 0.43
	400	21.2 ± 0.09
	800	17.9 ± 0.03
	1200	15.8 ± 0.04
	1600	14.1 ± 0.03
	1948	12.3 ± 0.11
22SiC	26	35.8 ± 0.29
	400	20.1 ± 0.10
	800	16.3 ± 0.05
	1200	14.0 ± 0.02
	1600	12.2 ± 0.03
	2000	9.78 ± 0.12
49SiC	26	42.9 ± 0.13
	400	19.9 ± 0.05
	801	14.5 ± 0.10
	1201	11.4 ± 0.18
	1599	9.31 ± 0.03
	1948	7.61 ± 0.04

on the three compositions. At any given temperature above 400°C, thermal diffusivity decreased with increasing SiC concentration. At room temperature, the composition with the highest SiC concentration had the highest thermal diffusivity.

Thermal diffusivity D (m²/s) was translated to thermal conductivity k (W/m · K) using the specific heat c_p (J/g ·K) and density ρ (g/m³): $k = D\rho c_p$. Heat capacities for the individual phases (ZrB$_2$, SiC, and B$_4$C) were taken from JANAF [9]data, and converted to specific heats using molar masses. The specific heats of the three compositions (shown in Figure 4.3) were calculated from a mass-based rule of mixtures using the as-batched compositions. Room temperature theoretical densities of the individual phases [10] were converted to values at other temperatures using thermal expansion data for ZrB$_2$ [11], α-
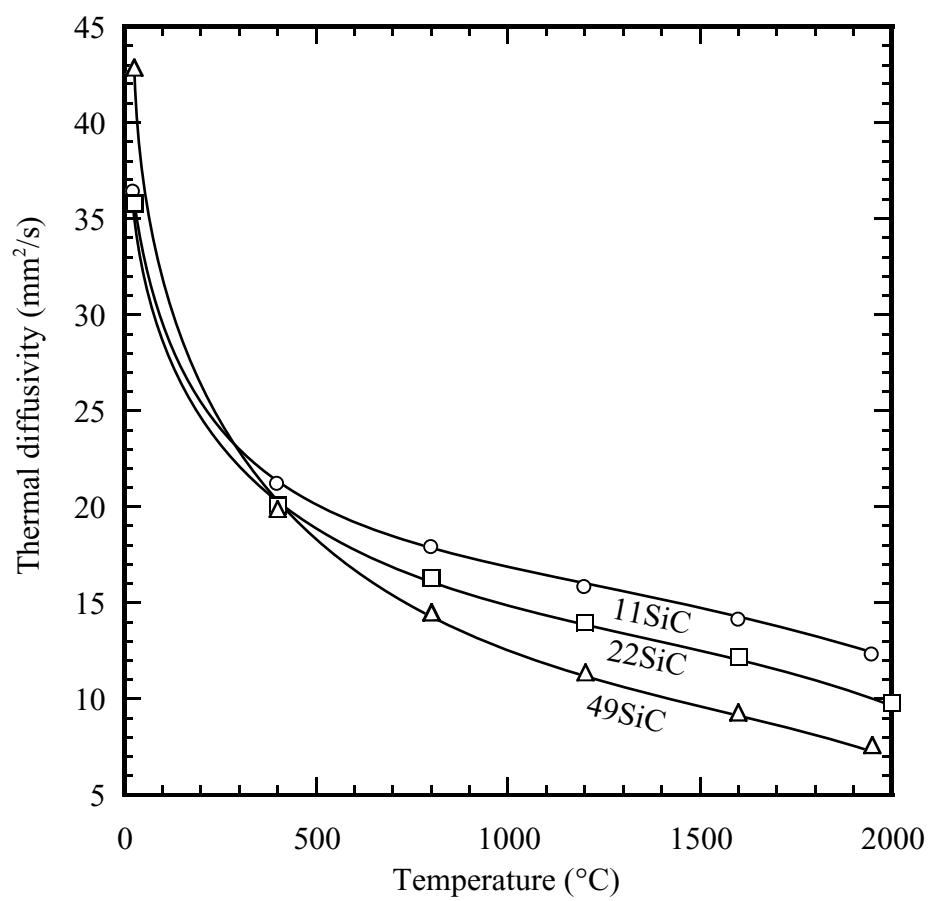
Figure 4.2: Thermal diffusivity measured by the laser flash technique over the temperature range of room temperature to ∼2000°C.
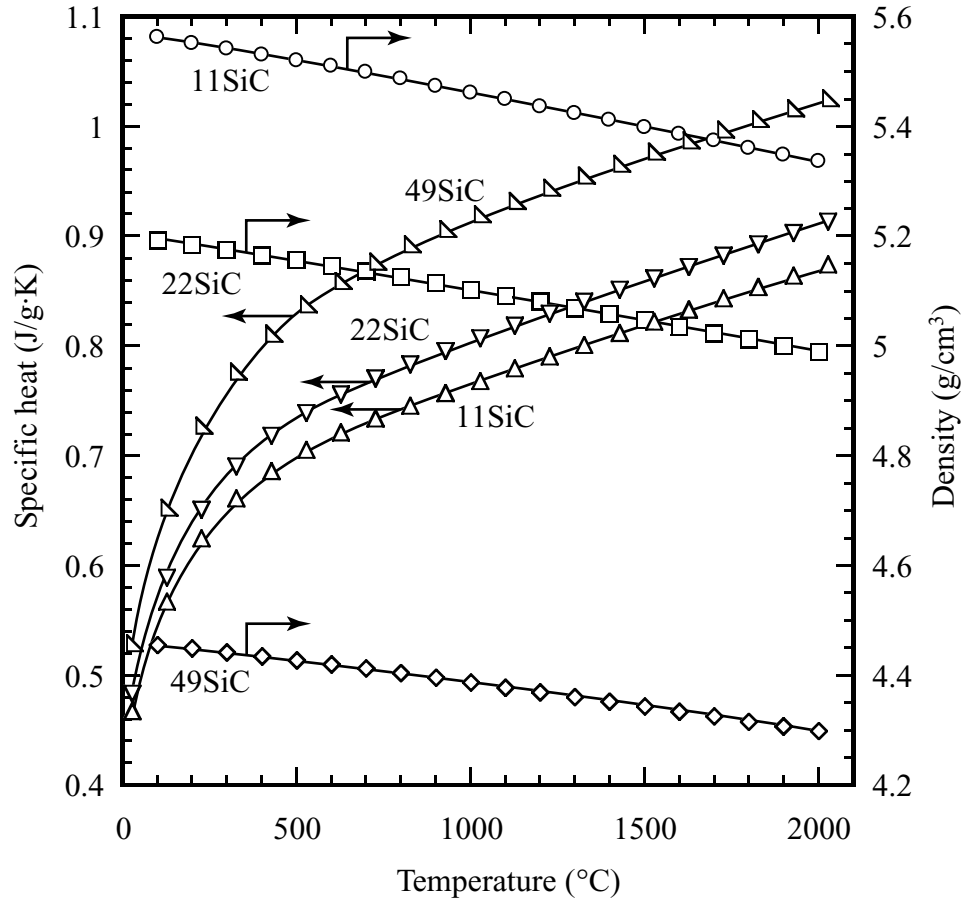
Figure 4.3: Temperature dependencies of specific heat and theoretical density for three compositions of ZrB$_2$-SiC-B$_4$C. Symbols for specific heat correspond to temperatures of JANAF heat capacity data. Symbols for theoretical density have no meaning other than curve identification.

SiC [12], and B$_4$C [13]. Linear coefficients of thermal expansion α_l were converted to volume coefficients α_V by: $\alpha_V = 3\alpha_l$. The temperature-dependences of theoretical densities were then determined by:

$$\rho = \frac{\rho_0}{1 + \alpha_V \Delta T}$$

where ρ_0 is the 25°C density, and ΔT is the temperature difference with 25°C. These values were then used in a volume-based rule of mixtures calculation of the temperature-dependent theoretical densities for the three compositions (Figure 4.3). Using these data, the thermal conductivities of the three compositions were calculated (using linear interpolation to line-up data points), and are shown in Figure 4.4. The temperature and compositional dependencies of thermal conductivities followed similar trends as those followed by the original thermal diffusivity data. The figure shows comparisons with literature data on similar compositions. The data obtained herein falls somewhat between Tye et al. [14] and Zimmerman et al. [15], though closer to Tye et al., and better follows the smooth decreasing (in absolute value) negative slope with temperature behavior of the Tye et al. data. The inconsistent slopes of the Zimmerman et al. data with temperature do not follow the more common trend of constant or smoothly decreasing (in absolute value) thermal conductivity slopes with temperature for refractory solids.

Figure 4.5 shows the thermal conductivities of SiC, B$_4$C, and ZrB$_2$ from the literature. On the overall scale of the graph, the agreement among the various sources for B$_4$C is relatively good, while SiC and the two sources of ZrB$_2$ data are relatively more divergent. The increasing thermal conductivity with increasing temperature of the Zimmerman et al. data is typically observed when radiation heat transfer becomes increasingly dominant, and the thermal conductivity that is measured is an "effective thermal conductivity." Such behavior; however, would not be expected from an electrically conductive solid such as ZrB$_2$ in which radiation heat transfer would be prohibited (conduction electrons move to oppose an electromagnetic field attempting to propagate through the solid).

Above room temperature, the decrease in thermal conductivity of SiC emulates that of a dielectric (though it is actually a semiconductor), while (Tye et al.) ZrB$_2$ behavior is more typical of an electrical conductor. Thus for a multi-phase microstructure at room temperature, SiC is comparable to or higher in thermal conductivity than ZrB$_2$ (depending on the literature citation selected), while at the high end of the literature temperature spectrum, SiC is thermally insulating relative to ZrB$_2$. This is consistent with the trends observed in Figure 4.4 in which, on a comparative basis, higher SiC concentration in the multi-phase microstructure facilitated higher thermal conductivity at ambient temperature, and increasingly lower thermal conductivity at temperatures of ∼400°C and above.

The literature data in Figure 4.5 were used in a finite-difference [23] calculation. The microstructures of the three compositions fabricated in this work are shown in Figure 4.6. These microstructures were mathematically divided up into 80×20 grids, and the majority phase in each cell was assigned to be the thermal conductivity of that cell (shown as distinct colors in Figure 4.7b). In the case of 49SiC, a small amount of porosity (likely grain pull-outs) was indicated in the microstructure; cells with this as the predominant phase were assigned a thermal conductivity of 0.05 W/m·K. Based on this construction, and assuming area% = vol%, the microstructures indicate compositions for 11SiC (80.2 vol% ZrB$_2$, 10.9 vol% SiC, 8.9 vol% B$_4$C), 22SiC (68.2 vol% ZrB$_2$, 22.8 vol% SiC, 9.0 vol% B$_4$C), and 49SiC (47.9 vol% ZrB$_2$, 48.0 vol% SiC, 4.1 vol% B$_4$C), which are remarkably close to the as-batched
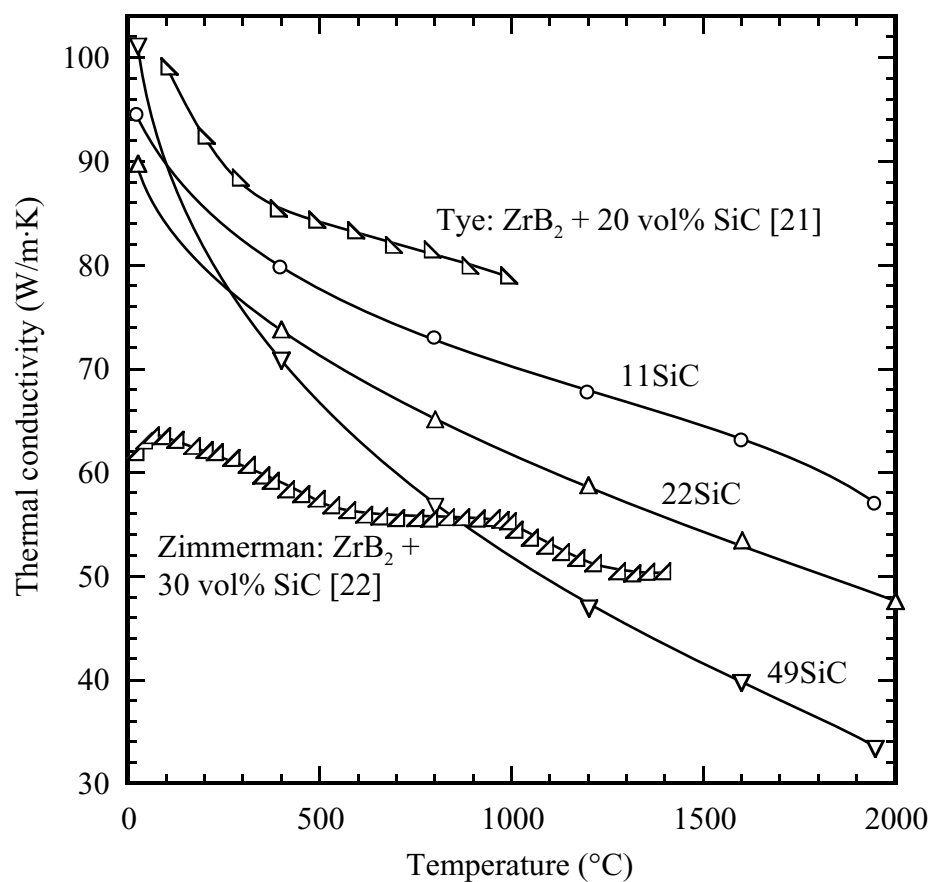
Figure 4.4: Thermal conductivities calculated from thermal diffusivity, specific heat, and theoretical density data. These are compared to literature ZrB_2-SiC thermal conductivity data.
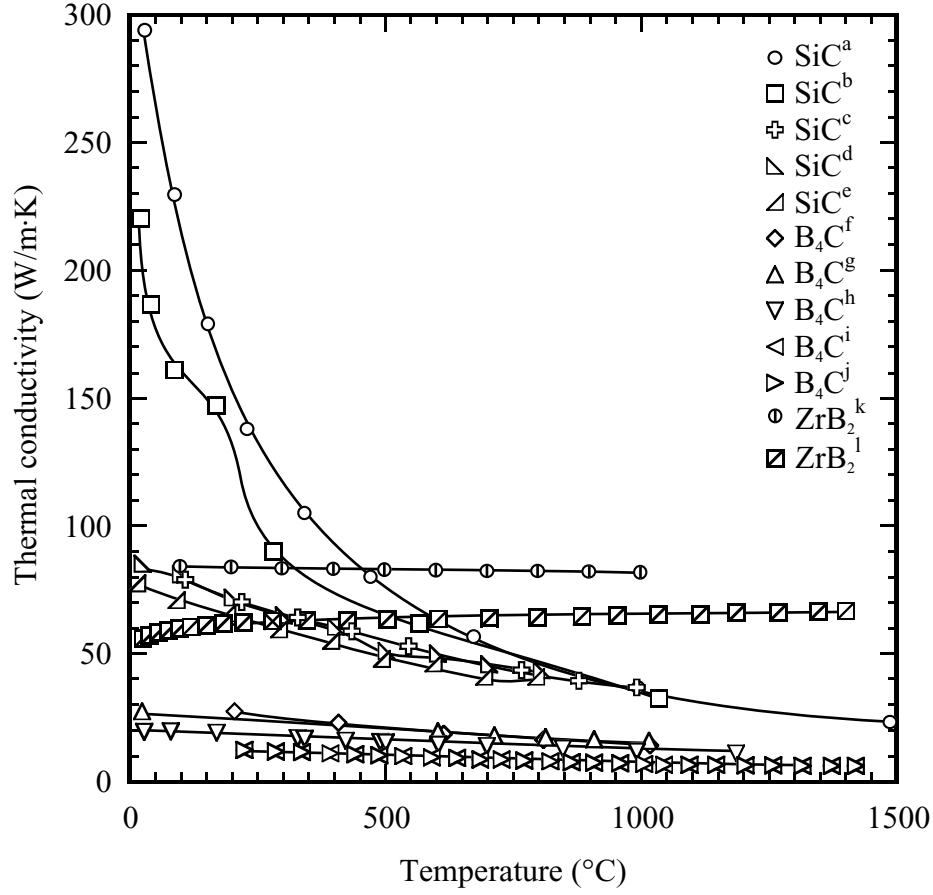
Figure 4.5: Literature values of thermal conductivity for B_4C, SiC, and ZrB_2. a. Single crystal SiC (R66) plotted in Watari et al. [16], based on Slack [17]. b. Mixture of α and β SiC hot pressed with BeO sintering aid, 100% dense [16]. c. (pre-) Hexoloy SA (Saint Gobain, Niagara Falls, NY) α-SiC, 98% relative density [12]. d. 95 vol% α-SiC - 5 vol% β-SiC, hot-pressed [18]. e. 76 vol% β-SiC - 24 vol% α-SiC, hot-pressed [18]. f. B_4C corrected for porosity [19]. g. B_4C data of Gilchrist and Preston [20] as plotted by Bouchacourt [19]. h. Spark-plasma sinterered B_4C (not isotopically enriched), 98% relative density [21]. i. EP (Eagle-Pitcher) hot-pressed B_4C [22]. j. Hot-pressed B_4C, 98% relative density [22]. k. Hot-pressed ZrB_2 [14]. l. Hot-pressed ZrB_2 [15].
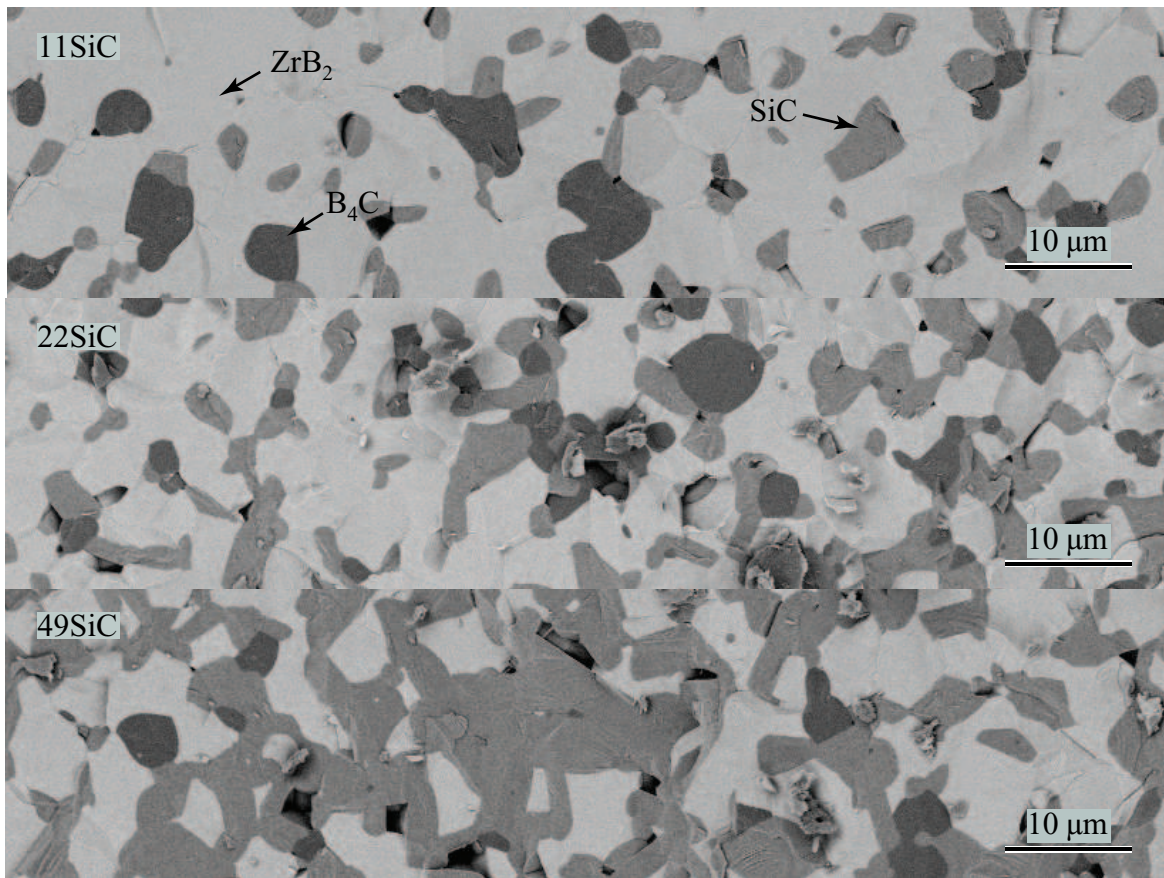
.

Figure 4.6: Fracture-surface (SEM backscattered) microstructures of the three evaluated compositions. Phases are identified by compositional contrast as ZrB_2, SiC, and B_4C, light to dark, respectively.
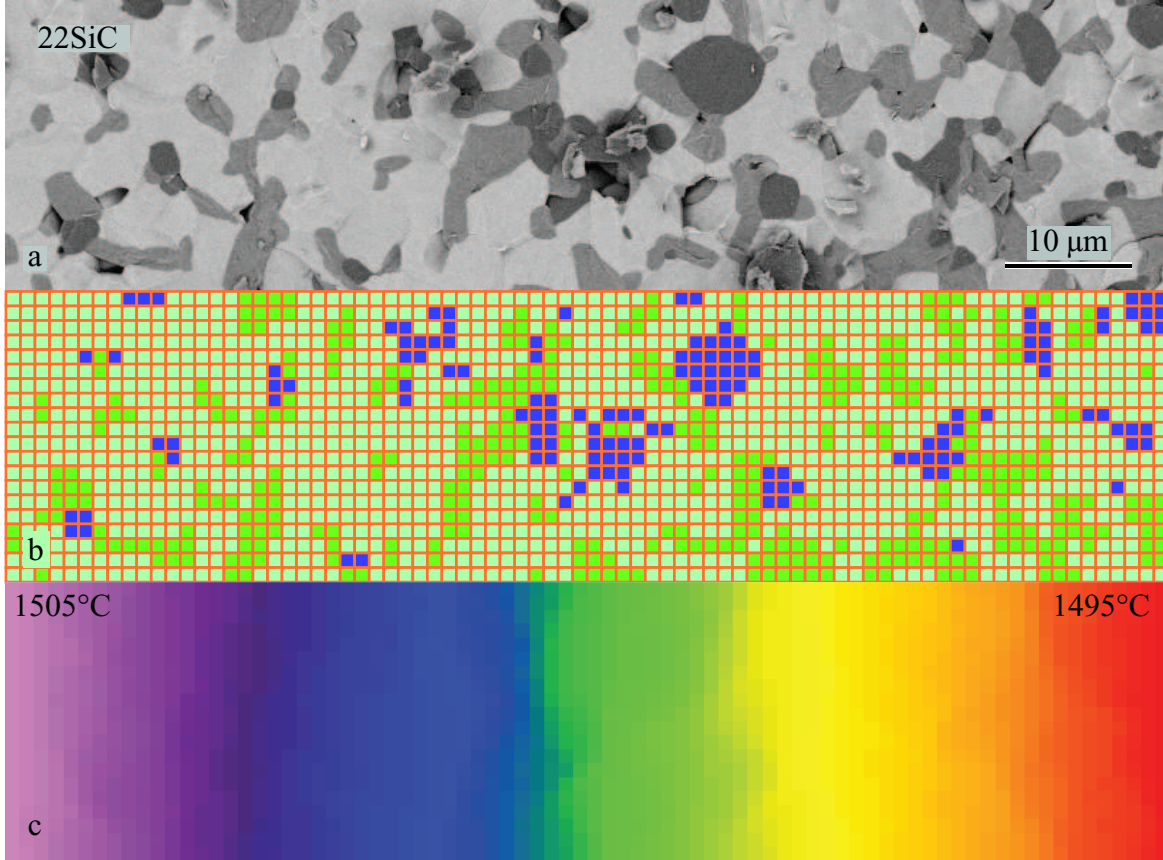
Figure 4.7: a. Electron micrograph of a 22SiC fracture surface. b. 80 × 20 grid with colors assigned to each cell based on the majority phase in that cell. c. Cells with rainbow sequence coloring to indicate relative temperature; violet indicates highest temperature and red indicates lowest temperature. For 22SiC at 1500°C: $k_{\text{SiC}} = 21.0$ W/m·K, $k_{\text{B}_4\text{C}} = 9.06$ W/m·K, $k_{\text{ZrB}_2} = 73.78$ W/m·K, based on averages of literature values.

compositions (volume percent) listed in Table 4.1.

The finite difference method was applied as depicted in Figure 4.8. Nodes were assigned to be at the centers of each cell. The temperatures at the left and right edges of the microstructure (cell array) were assigned to fixed values of 5°C above (left side) and 5°C below (right side) a specified temperature. Heat flow was assumed to be two-dimensional, with the third dimension being of unit dimension. The upper and lower edges were assumed to be adiabatic. The adiabatic boundary for the upper and lower edges was positioned directly on the nodes for mathematical convenience. Steady state heat flow was assumed, and the temperature gradients between neighboring cells were assumed to be linear. Under these conditions, the sum of heat flows into and out of each node must be zero. Such equations fall into categories a-i, as shown in Figure 4.8 and below:

$$a. \quad \frac{T_{m,n} - T_{m,n+1}}{\frac{1}{k_{m,n+1}} + \frac{1}{k_{m,n}}} + \frac{T_{m,n} - T_{m,n-1}}{\frac{1}{k_{m,n-1}} + \frac{1}{k_{m,n}}} + \frac{T_{m,n} - T_{m-1,n}}{\frac{1}{k_{m-1,n}} + \frac{1}{k_{m,n}}} + \frac{T_{m,n} - T_{m+1,n}}{\frac{1}{k_{m+1,n}} + \frac{1}{k_{m,n}}} = 0$$

$$b. \quad \frac{T_{m,n} - T_{m+1,n}}{\frac{1}{k_{m+1,n}} + \frac{1}{k_{m,n}}} + \frac{T_{m,n} - T_{m-1,n}}{\frac{1}{k_{m-1,n}} + \frac{1}{k_{m,n}}} + \frac{2\left(T_{m,n} - T_{m,n-1}\right)}{\frac{1}{k_{m,n-1}} + \frac{1}{k_{m,n}}} = 0$$

$$c. \quad \frac{T_{m,n} - T_{m-1,n}}{\frac{1}{k_{m-1,n}} + \frac{1}{k_{m,n}}} + \frac{T_{m,n} - T_{m+1,n}}{\frac{1}{k_{m+1,n}} + \frac{1}{k_{m,n}}} + \frac{2\left(T_{m,n} - T_{m,n+1}\right)}{\frac{1}{k_{m,n+1}} + \frac{1}{k_{m,n}}} = 0$$

$$d. \quad k_{m,n}\left(T_{m,n} - T_{\text{left}}\right) + \frac{T_{m,n} - T_{m+1,n}}{\frac{1}{k_{m+1,n}} + \frac{1}{k_{m,n}}} + \frac{T_{m,n} - T_{m,n-1}}{\frac{1}{k_{m,n-1}} + \frac{1}{k_{m,n}}} + \frac{T_{m,n} - T_{m,n+1}}{\frac{1}{k_{m,n+1}} + \frac{1}{k_{m,n}}} = 0$$

$$e. \quad k_{m,n}\left(T_{m,n} - T_{\text{right}}\right) + \frac{T_{m,n} - T_{m-1,n}}{\frac{1}{k_{m-1,n}} + \frac{1}{k_{m,n}}} + \frac{T_{m,n} - T_{m,n-1}}{\frac{1}{k_{m,n-1}} + \frac{1}{k_{m,n}}} + \frac{T_{m,n} - T_{m,n+1}}{\frac{1}{k_{m,n+1}} + \frac{1}{k_{m,n}}} = 0$$

$$f. \quad k_{m,n}\left(T_{m,n} - T_{\text{left}}\right) + \frac{T_{m,n} - T_{m+1,n}}{\frac{1}{k_{m+1,n}} + \frac{1}{k_{m,n}}} + \frac{2\left(T_{m,n} - T_{m,n-1}\right)}{\frac{1}{k_{m,n-1}} + \frac{1}{k_{m,n}}} = 0$$

$$g. \quad k_{m,n}\left(T_{m,n} - T_{\text{left}}\right) + \frac{T_{m,n} - T_{m+1,n}}{\frac{1}{k_{m+1,n}} + \frac{1}{k_{m,n}}} + \frac{2\left(T_{m,n} - T_{m,n+1}\right)}{\frac{1}{k_{m,n+1}} + \frac{1}{k_{m,n}}} = 0$$

$$h. \quad k_{m,n}\left(T_{m,n} - T_{\text{right}}\right) + \frac{T_{m,n} - T_{m-1,n}}{\frac{1}{k_{m-1,n}} + \frac{1}{k_{m,n}}} + \frac{2\left(T_{m,n} - T_{m,n-1}\right)}{\frac{1}{k_{m,n-1}} + \frac{1}{k_{m,n}}} = 0$$

$$i. \quad k_{m,n}\left(T_{m,n} - T_{\text{right}}\right) + \frac{T_{m,n} - T_{m-1,n}}{\frac{1}{k_{m-1,n}} + \frac{1}{k_{m,n}}} + \frac{2\left(T_{m,n} - T_{m,n+1}\right)}{\frac{1}{k_{m,n+1}} + \frac{1}{k_{m,n}}} = 0$$

For the 80×20 matrix, this generated 1600 simultaneous equations. Code for setting up the matrix and solving the simultaneous equations by matrix inversion was written in Visual Basic 4.0. The temperature-dependent thermal conductivities of the individual phases were

taken as the average of the literature values (single-crystal SiC excluded). A depiction of the solution set of node temperatures for 22SiC at 1500°C is shown in Figure 4.7c. From these temperatures, the thermal conductivities of the multi-phase microstructures were then determined by calculating the heat flux from the left-end reservoir to the left edge nodes, and then determining an effective thermal conductivity through the entire microstructure based on a 10°C temperature gradient. The results of this calculation are shown in Figure 4.9. These data are consistent in trend with those experimentally derived for these compositions (Figure 4.4); above 400°C, thermal conductivity decreased with increasing SiC concentration, and at room temperature, the specimen with the highest SiC content had the highest thermal conductivity. These data were lower in thermal conductivity for a given composition and temperature than those experimentally determined; agreement was closer at higher temperatures. The model data were generally in greater disagreement with experimental results with decreasing SiC content. Decreasing SiC content in the model requires increasing dependence on the literature ZrB_2 thermal conductivity data. Clearly, if the Tye et al. ZrB_2 data were used alone, rather than averaged with the Zimmerman et al., the finite-difference-calculated thermal conductivities of the multi-phase microstructures would have been higher, and much closer to the experimental results of Figure 4.4.

The finite difference method was used for a separate calculation in which the thermal conductivities of SiC and B_4C were taken as the average of literature values, as before. The thermal conductivities of the three compositions were taken from the experimentally-derived results herein, and the values of the thermal conductivities of the ZrB_2 phase were back-calculated. The determination was based on a numerical search routine written into the code, iterating seed values of k_{ZrB_2}, comparing the resulting calculated multi-phase thermal conductivity to that experimentally determined, generating a corrected seed value, and so on, until the calculated and measured composite thermal conductivities were within 0.1 W/m·K. The results of these calculations are shown in Figure 4.10. With one exception (ZrB_2:49SiC at 1600°C), calculated thermal conductivities (Figure 4.10) were relatively constant at ∼88-104 W/mK, which is higher than the two literature data sets in Figure 4.5, being closer to the results of Tye et al. [14] than Zimmermann et al. [15]. The solution for 49SiC at 1600°C was based on an extrapolated value of the averaged literature thermal conductivity for SiC from lower temperature values, which is likely unreliable. Since 49SiC had the highest concentration of SiC, the 1600°C calculated thermal conductivity of ZrB_2, now a minority phase, was substantially shifted upward to compensate for the assumed value of thermal conductivity of SiC.

IV   Conclusion

Thermal conductivities in the temperature range 25-2000°C were calculated from laser-flash thermal diffusivity data, using specific heat, theoretical density, and thermal expansion data. The more dielectric-like behavior of the SiC imbued a greater temperature sensitivity to ZrB_2-SiC-B_4C multiphase ceramics with increasing SiC content. Finite difference calculations, using averaged literature values for the thermal conductivities of individual ZrB_2, SiC, and B_4C phases, correctly predicted the trends observed from experimental measurements; the composition with the highest SiC content (48.7 vol%) showed the highest room temperature thermal conductivity, but above ∼400°C, demonstrated the lowest thermal conduc-

tivity. The temperature-dependent thermal conductivity of pure ZrB_2 was back-calculated using finite-difference calculations, experimental results for multi-phase compositions, and averaged literature values for SiC and B_4C; it was relatively constant (88-104 W/m·K) over the full evaluated temperature range.
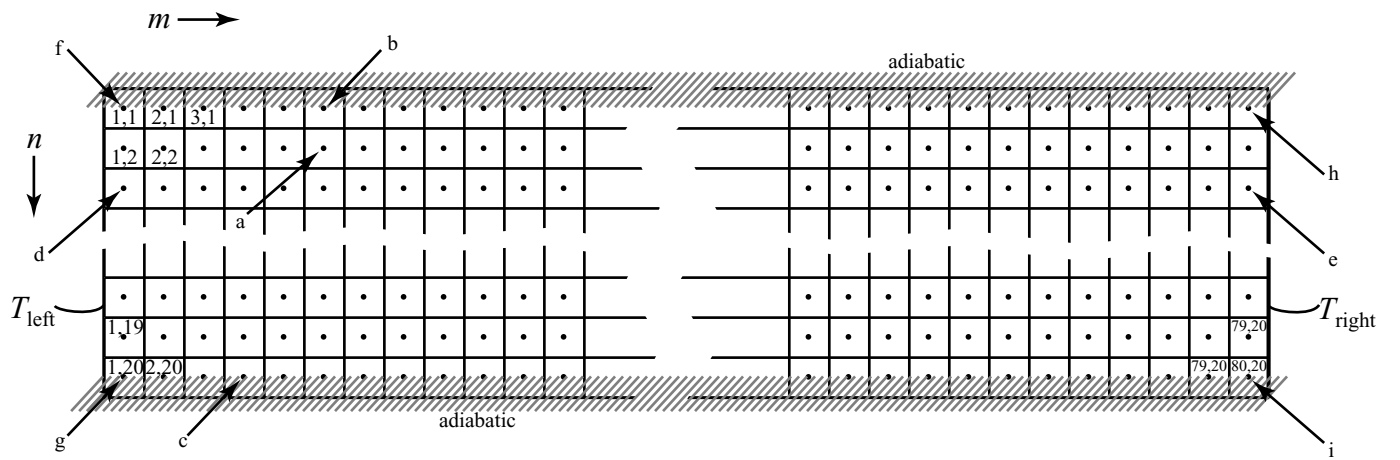
Figure 4.8: Depiction of 80×20 cells/nodes indicating regions for node equations: a. Interior. b. Upper edge (insulated). c. Lower edge (insulated). d. Left edge (fixed temperature of $5°C$ above designated temperature). e. Right edge (fixed temperature of $5°C$ below designated temperature). f. Upper left corner. g. Lower left corner. h. Upper right corner. i. Lower right corner.
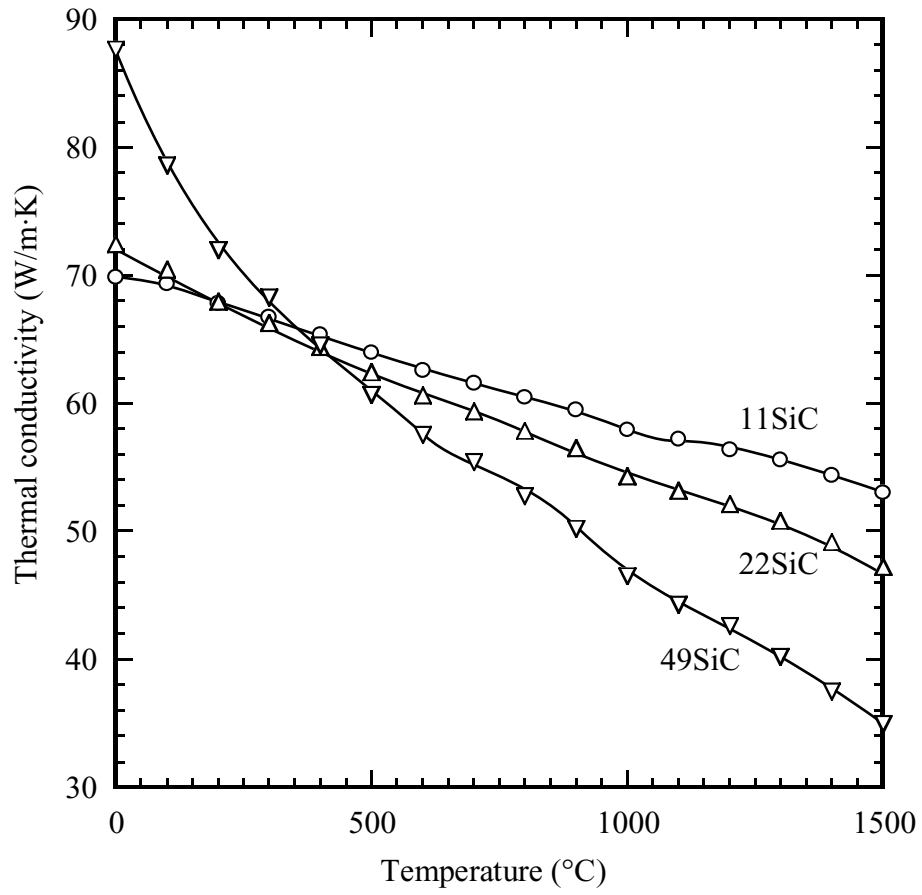
Figure 4.9: Thermal conductivity of three compositions calculated using averaged literature values of ZrB_2, SiC, and B_4C, the distribution of phases based on a grid overlay of SEM micrographs, and the finite difference method.
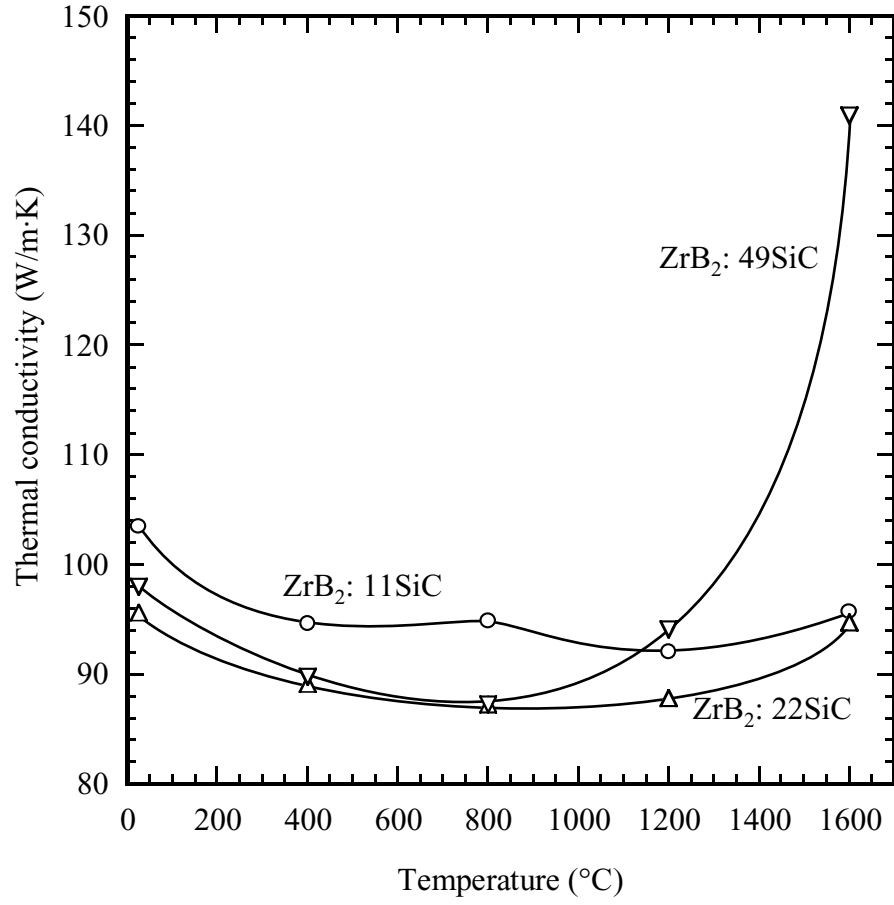
Figure 4.10: Thermal conductivity of ZrB_2 calculated based on thermal conductivities of ZrB_2-SiC-B_4C multi-phase microstructures and averaged literature thermal conductivities for SiC and B_4C.

Bibliography

[1] Y. S. Touloukian, *Thermophysical Properties of Matter*, Vols. 1 and 2, Plenum Press, New York, 1970.

[2] G. Grimvall, *Thermophysical Properties of Materials*, Elsevier Science Pub. Co. Inc., New York, 1986.

[3] W. D. Kingery, H. K. Bowman, and D. R. Uhlmann, *Introduction to Ceramics,* John Wiley and Sons, New York, 1976.

[4] F. Peng, G. Van Laningham, and R. F. Speyer, "Thermogravimetric Analysis of the Oxidation Resistance of ZrB_2-SiC and ZrB_2-SiC-TaB_2-Based Compositions in the 1500-1900°C Range," *J. Mater. Res.,* **26** [1], 96-107 (2011).

[5] F. Peng, Y. Berta and R. F. Speyer, "Effect of SiC, TaB_2 and $TaSi_2$ Additives on the Isothermal Oxidation Resistance of Fully Dense Zirconium Diboride," *J. Mater. Res.,* **24** [5] 1855-1867 (2009).

[6] R. J. Parker, R. J. Butler, C. P. Butler, and G. I. Abbott, "A Flash Method of Determining Thermal Diffusivity, Heat Capacity, and Thermal Conductivity," *J. Appl. Phys.,* **32** 1679-1684 (1961) .

[7] T. R. Lee, Ph. D. Thesis, "Thermal Diffusivity of Dispersed and Layered Composites," Purdue University, University Microfilms International, 1977.

[8] J. N.. Sweet, "Data Analysis Methods for Flash Thermal Diffusivity Experiments," Sandia National Laboratories Report SAND89-0260 US-25, 1989.

[9] M. W. Chase, Jr., Ed., *NIST-JANAF Thermochemical Tables,* 4th Ed., Monograph No. 9, Parts I and II, American Institute of Physics, Woodbury, NY, 1998.

[10] D. R. Lide, Ed., *CRC Handbook of Chemistry and Physics*, 81st Ed., CRC Press, Boca Raton, FL (2001).

[11] F. G. Keihn and E. J. Keplin, "High-Temperature Thermal Expansion of Certain Group IV and Group V Diboides," *J. Am. Ceram. Soc.,* **50** [2] 81-84 (1967).

[12] R. G. Munro, "Material Properties of a Sintered α-SiC," *J. Phys. Chem. Ref. Data,* **26** [5] 1195-1203 (1997).

[13] G. V. Tsagareishvili, T. G. Nakashidze, J. S. Jobava, G. P. Lomidze, D. E. Khulelidze, D. Sh. Tsagareishvili, and O. A. Tsagareishvili,"Thermal Expansion of Boron and Boron Carbide," *J. of the Less-Common Metals*, **117** [1-2] 159-161 (1986).

[14] R. P. Tye, and E. V. Clougherty, "The Thermal and Electrical Conductivities of Some Electrically Conducting Compounds," *Proceedings of the Fifth Symposium on Thermophysical Properties*, Newton, MA, September 30 - October 2, 396-401, 1970.

[15] J. W. Zimmermann, G. E. Hilmas, W. G. Fahrenholtz, R. B. Dinwiddie, W. D. Porter, and H. Wang, "Thermophysical Properties of ZrB_2 and ZrB_2-SiC Ceramics," *J. Am. Ceram. Soc.,* **91** [5] 1405-1411 (2008).

[16] K. Watari, H. Nakano, K. Sato, K. Urabe, K. Ishizaki, S. Cao, and K. Mori, "Effect of Grain Boundaries on Thermal Conductivity of Silicon Carbide Ceramic at 5 to 1300 K," *J. Am. Ceram. Soc.,* **86** [10] 1812-14 (2003).

[17] G.A. Slack, "Thermal Conductivity of Pure and Impure Silicon, Silicon Carbide, and Diamond," *J. Appl. Phys.,* **35** 3460-66 (1964).

[18] D.-M. Liu and B.-W. Lin, "Thermal Conductivity in Hot-Pressed Silicon Carbide," *Ceram. Int.,* **22** 407-414 (1996).

[19] M. Bouchacourt and F. Thevenot, "The Correlation Between the Thermoelectric Properties and Stoichiometry in the Boron Carbide Phase B_4C-$B_{10.5}C$," *J. Mater. Sci.,* **20** 1237-1247 (1985).

[20] K. E. Gilchrist and S. D. Preston: "Thermophysical Property Measurements on Some Neutron Absorbing Materials," *High Temp. High Press.,* **11** 643651 (1979).

[21] Y. Nishi, Y. Arita, T. Matsui, and T. Nagasaki, "Isotope Effects on Thermal Conductivity of Boron Carbide," *J. Nuc. Sci.,* **39** [4] 391-394 (2002).

[22] C. Wood, D. Emin, and P. E. Gray, "Thermal Conductivity of Boron Carbides," *Phys. Rev. B,* **31** 6811-6814 (1985).

[23] F. P. Incropera and D. P. DeWitt, *Fundamentals of Heat and Mass Transfer*, John Wiley and Sons, New York, 2002.

Chapter 5

Spectral Emittance of ZrB$_2$-30 mol% SiC Electrically Heated Ribbons over 1-6 μm

I   Introduction

The efficiency of heat transfer by thermal radiation is described by the spectral emissivity, which is the ratio of the emission from a real body to that of a blackbody at a given wavelength. A blackbody is a perfect emitter and perfect absorber (no transmission, no reflection) of radiant energy, and follows Planck's law with respect to wavelength and temperature:

$$R_T(\lambda) = \frac{2\pi hc^2}{\lambda^5} \frac{d\lambda}{\exp\left(\frac{hc}{\lambda kT}\right) - 1}$$

where $R_T(\lambda)$ is the spectral radiosity, h is Planck's constant, k is Boltzmann's constant, λ is wavelength, c is the speed of light, and T is the absolute temperature. The term "spectral" in spectral emissivity refers to the wavelength dependence of this ratio. In dielectrics, for example, there are regions in the infrared portion of the spectrum which are highly absorbing because the electromagnetic radiation is resonant with the vibration frequencies of atoms in the lattice. The spectral emissivity is a material's property which assumes polished surfaces. For rough-surfaced materials there is the potential for multiple reflections inside of crevices, increasing the odds of absorption of a quanta of light. The spectral emittance has been coined as a term to describe the effective emissivity for such real surfaces; spectral emittance increases with increasing surface roughness.

Emittance is an important consideration for UHTCs since the temperatures they reach via friction with the atmosphere will be determined, in part, by the efficiency with which they radiate heat away to the cold surrounding ambient. Experimental measurement of emittance is often complicated by the fact that the self-luminescent sample must be observed in relative isolation; reflections of thermal radiation from nearby hot regions (such as heating elements

or furnace walls) become merged with radiation emitted by the specimen. Halloran, et al. took advantage of the fact that ZrB_2-based materials behave as a metallic conductor. Thinly machined ribbons of ZrB_2-based ceramic compositions were able to be directly resistively heated [2]. Ribbon temperatures were controlled via an infrared pyrometer. A modification of this setup has been developed for the work described herein.

Scatteia et al. studied the radiative properties of two compositions: ZrB_2-15 vol% SiC and ZrB_2-15 vol% SiC-10 vol%HfB_2, and reported that total (wavelength aveaged) emittance generally increased with temperature due to the formation of the protective oxide layer, and that the specimen containing no HfB_2 showed a comparatively higher emittance overall (Figure 5.1). The data presented, however, were only of total emissivity; spectral emissivity data are available in the literature for homogeneous specimens of zirconium diboride, zirconia, or borosilicate glass (Figure 5.2), but as shown in the figure, this behavior is dependent on morphology of the surface.

II   Experimental Procedure

Theoretically-dense test specimens were fabricated using techniques as described elsewhere in this report. The composition of the synthesized powder mixture is given in Table 5.1. Rectangular specimens were machined (Advanced Ceramics Manufacturing, Tucson, AZ)

Table 5.1: Sample Composition

Mole Percent			Volume Percent			Mass Percent		
ZrB_2	B_4C	SiC	ZrB_2	B_4C	SiC	ZrB_2	B_4C	SiC
64.25	6.04	29.70	70.32	7.82	21.87	82.63	3.80	13.57

into ribbons of ∼1 cm in height, ∼3 cm in length, and ∼0.3 mm in thickness (in the thinned center regions).

A custom-built chamber supported and made electrical contact to the specimens, and allowed observation of their surfaces while at selected temperatures in a flowing argon atmosphere. The specimens were positioned in the center of the unit, held in place by a copper clamping system connected to two large copper feed-through bus bars, in turn connected to the secondary stage of a step-down transformer. Electrical connections were made on thickened extremes of the specimens, leaving a thinned center region (of higher resistance) as the heating zone. The specimens were oriented such that the front and back sides faced opposing modular viewports through which a spectral radiometer and a pyrometer, respectively, could receive radiation (an accessory viewport was positioned to observe the front of the ribbon at an angle of 45° from the surface normal, but this was not used in this work). Thus spectral radiosity measurements were performed at an angle normal to the ribbon surface. Specimens were loaded and removed from the chamber via an O-ring-sealed plate on the top of the unit.

Atmosphere control was accomplished via two 6.35 mm gas flow tubes on opposite sides of the ribbon. The inlet tube provided ultra-high purity argon at a known flow rate, and the outlet tube led to either a mechanical vacuum pump or a bubble flow-back check valve,
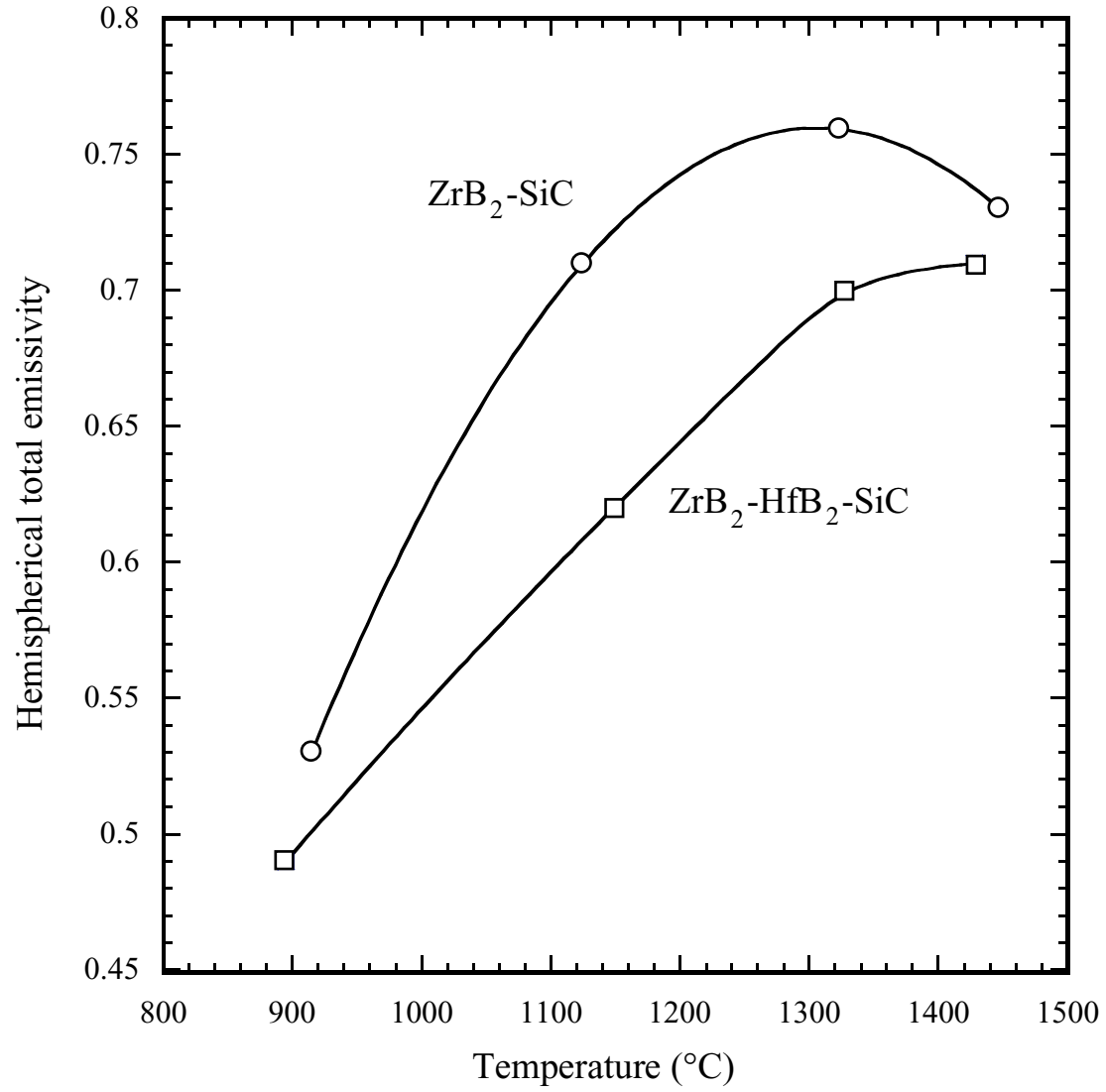
Figure 5.1: Total hemispherical emissivity (from 0.6 to 40 μm) as a function of temperature for two UHTC compositions (ZrB$_2$-15 vol%SiC and ZrB$_2$-15 vol%SiC-10 vol%HfB$_2$) heated under 10 Pa of air in a solar collector [3].
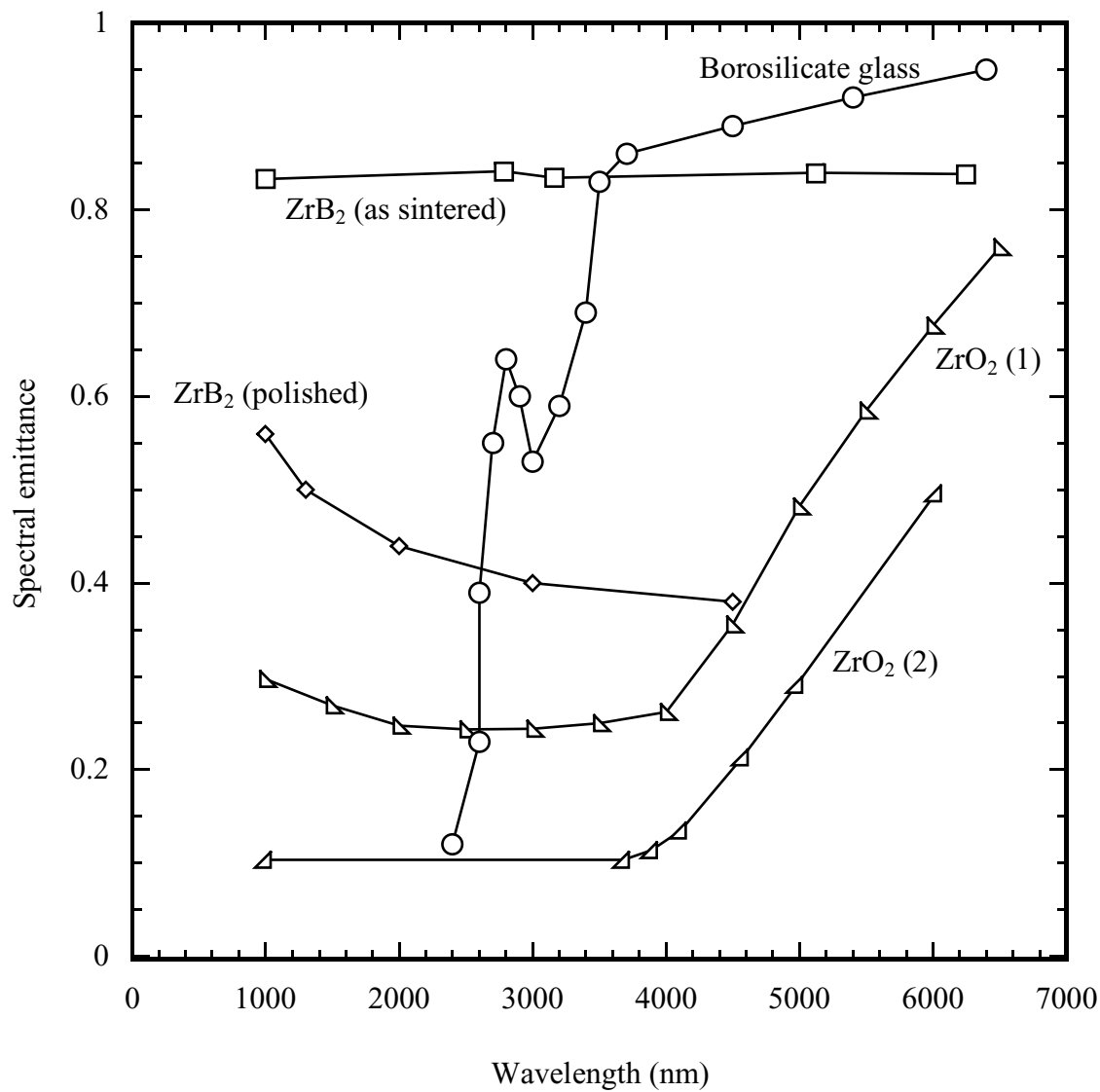
Figure 5.2: Literature values of the normal spectral emittance of ZrB_2, ZrO_2, and borosilicate glass, demonstrating the range of reported values. The higher ZrB_2 values correspond to an un-polished, as-sintered sample [1].

selected via a 3-way junction. Internal pressure of the chamber was monitored with a mechanical pressure gauge mounted downstream on the outlet line.

The temperature feedback control system itself consisted of an infrared pyrometer with a digital output read by a personal computer via RS232 protocol. A PID algorithm in the computer generated a 4-20 mA signal (via a 12 bit D/A converter) to an SCR throttling power to the step down transformer. The temperatures of the specimens were monitored from their back faces through a fused silica view port by a two-color pyrometer (Modline 5R, IRCON, Inc, Santa Cruz, CA) focused on a circle of approximately 4 mm in diameter at the center of the heated ribbon. The two-color pyrometer was not adequately sensitive to temperatures below 1000°C, so specimens were heated to this temperature by a gradual linear rate of power increase until a valid signal was reported by the pyrometer. The SCR chopped power delivered from a 280 V 60 Hz single-phase wall source to a series of two step-down transformers rigged to provide a maximum 10 V RMS ac potential across the ribbon samples.

Spectral radiosity data collection was accomplished with a computer-controlled spectral radiometer (OL Series 750 Automated Spectroradiometric Measurement System, Gooch & Housego (formally Optronic Laboratories), Orlando, FL) which diffracts incoming radiation on a grated mirror mounted on a rotating turret, thereby directing specific wavelengths to a detector. The unit was capable of evaluating the spectral radiosity of the specimens over a range of wavelengths from 350 to 16,000 nm using one of two detectors: a silicon detector (350 to 1000 nm), and a liquid nitrogen-cooled CdHgTe detector (1000 to 16,000 nm). At 1400 K, over 98% of blackbody radiation is emitted at wavelengths less than 14,000 nm [1]).

The spectral radiometer was calibrated against a specially-constructed steel blackbody cavity mounted within a $MoSi_2$ furnace at ∼1500°C. The cavity was protected against excessive oxidation via a flow of dry argon gas. The back-wall temperature of the cavity was measured using a Type S thermocouple in direct contact with it, before and after spectra was captured by the radiometer. Using Planck's law for that temperature, the radiometer was then calibrated for all evaluated wavelengths. These calibrations were then confirmed by measuring the spectral radiosity of the cavity back wall held at another known temperature.

The spectral radiometer was equipped with two reflex telescopes: one with optics constructed from fused silica, the other with optics of ZnSe, which allowed measurements over the entire detectable spectrum to be made, with a target area less than 1 cm in diameter from a distance of 90 cm. The spectral radiometer itself was not air-tight, but instead featured a purge gas port through which a positive pressure of shield gas could be provided to flood the unit. The optical path from the radiometer to the ribbon chamber was contained by a length of PVC pipe which was itself outfitted with a purge gas port. To minimize the effect of atmospheric absorption due to the presence of H_2O and CO_2 across some bands of the infrared spectrum, a shield gas of dry synthetic air was flooded through the spectral radiometer and its line-of-sight to the specimen for a period of no less than four hours prior to measurement, and continued throughout each measurement.

Ribbon specimens first underwent oxidation in a $MoSi_2$ furnace in stagnant air on a zirconia setter at 1500°C for 1 h. For electrical contact surface locations, the oxide coating on these samples was ground by hand from the top and bottom surfaces of the thickened regions with dry 220 grit SiC sandpaper so that a low-resistance electrical connection could be achieved. A handheld multimeter was used to measure resistance as a check on the progress of the oxide removal, with sub-ohm readings being considered indicative of a fully

cleaned surface. In-situ oxidation of the ribbons was attempted by running a ribbon open to the atmosphere to 1400°C, but the specimens typically fractured, and the aforementioned higher-yield pre-oxidation procedure, with subsequent spectral radiosity measurements under flowing argon, was determined to be preferred. Samples were loaded into the copper clamping system (which was periodically sanded with 220 grit SiC paper to remove trace oxidation at the contact points) and the chamber was evacuated and backfilled with ultra-pure argon three times. The argon was then set to flow through the ribbon chamber at a typical rate of 100 cm^3/min, and a measurement program was prepared to scan through wavelength ranges and record data.

A thermal schedule was then programmed; linear power ramp to pyrometer detection range (1000°C), then 200°C/min 1200°C, and a dwell period of 60 minutes during which spectral measurements were taken. The overhead lights in the room were lowered both to limit external influence on the measurement and to allow for better observation of the sample through the auxiliary viewport.

A large fraction of ribbon specimens tested over the course of this project failed during heating to the setpoint. More cautious heating rates (30°C/min) were attempted, but did not yield a lower specimen mortality rate; the cause of failure is believed to have been associated with defects within the specimens resulting in regions of uneven heating which then led to local thermal shock cracking, in turn resulting in catastrophic failure. Emittance measurements were not begun until the specimens had attained a temperature within 3°C of the specified setpoint (the control system was found to reliably hold the observed specimen temperature to within this range of the setpoint during steady operation). Identical measurements were conducted one after the other to characterize any changes over the time at temperature.

Spectral radiosity measurements were performed in two separate batches corresponding to the availability of machined ribbon specimens. The first batch of measurements were performed under the control of a different pyrometer than that which was used for the second batch (the first batch pyrometer being a unit on loan from the distributer). The recorded wavelength step sizes of the batch 1 and batch 2 scans were 20 and 10 nm, respectively. Batch 2 ribbons were scanned twice over the 1000-6000 nm range while the ribbon was maintained at a selected temperature, each scan requiring ~30 min.

II.1   Results and Discussion

The make, model, and settings of the pyrometers for batches 1 and 2 were identical, however the calibrations of the two units, performed by the supplier, were deemed to be different. Figure 5.3 shows the spectral radiosities from 1-6 μm of two similarly-oxidized ribbons held at a pyrometer-reported temperature of 1200°C. The spectra are remarkably grey; there are no apparent peaks in the spectra associated with vibration resonance with a dielectric.

Attempts to independently measure the temperatures of the incandescent ribbon samples by means of a thermocouple were thwarted both by inadequate contact between the thermocouple junction and the ribbon to be measured, as well as a reaction between the metal leads of the thermocouple and the oxide surface. An independent measure of actual ribbon temperature was made using Wien's displacement law,
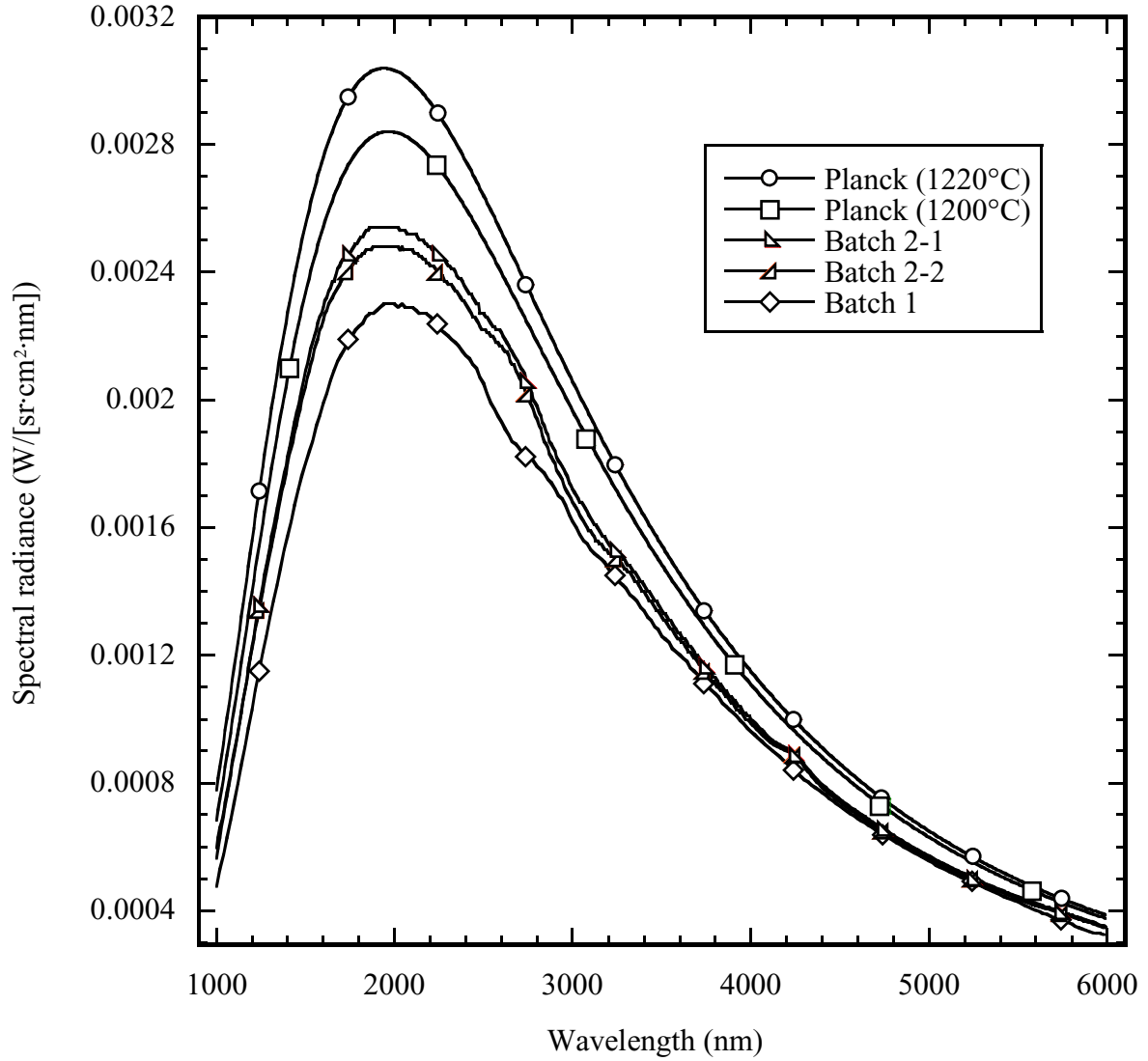
$$\lambda_{max} = \frac{b}{T}$$

Figure 5.3: Experimental data curves from oxidized ribbons (Batch 2 was evaluated twice) are shown beneath blackbody emittance curves (Planck's law) for the indicated temperatures, 1200 and 1220°C, which correspond to the Wien's displacement law-derived values for the Batch 1 and Batch 2 ribbons, respectively. Symbols are for the sole purpose of identifying the curves; this is the case for all such plots in this document.

wherein λ_{max} is the peak wavelength, b is a constant (2897768.5 nm·K), and T the absolute temperature. Wien's displacement law assumes blackbody or greybody behavior (constant emittance with wavelength), the latter of which appears to be an acceptable approximation for these data. For the Batch 1 spectra in Figure 5.3 at a pyrometer-reported temperature of 1200°C, Wein's displacement law indeed indicates a temperature of ~1200°C ($\lambda_{max} \approx 1.97$ μm), while the spectra collected for Batch 2 indicates a temperature of ~1220°C ($\lambda_{max} \approx$ 1.94 μm). Similar Wein's displacement law corrections were applied to other ribbon soak temperatures.

Figure 5.3 displays experimental data falling below the respective blackbody values . The spectral emittance values, calculated as a ratio of measured spectral radiosities to those of a blackbody at the same temperature, are displayed in Figures 5.4, 5.5, and 5.6. The shaded regions in the figures indicate portions of the infrared spectrum in which gaseous absorption (if cold) or transmission (if hot) is expected (~2,800 and 4,250 nm for CO_2 and 5,500-6000 nm for H_2O). These figures show an increasing emittance with longer wavelengths.

Countering the effect of the increasing spectral emittance with longer wavelength is an observed decline in spectral emittance over the time period of the data scan, as evidenced by the lower radiance values of the second runs of Batch 2. Data were collected with hot ribbon specimen surfaces exposed to a flowing Ar atmosphere, within which the previously-formed silicate oxide layer is unstable. The use of a flowing inert atmosphere was deemed necessary to sustain good electrical contact of the ribbons with the copper clamping system for the lifetime of the isothermal measurments. For each soak temperature, the two spectral radiosity data sets were collected over the course of a single heating of a newly oxidized ribbon. Two identical data collection programs were run by the spectral radiometer, each lasting ~30 min and one occurring immediately after the other. Figure 5.7) reveals a ~0.02-0.04 decrease in the second relative to the first spectral emittances at 1120°C. Similarly a ~0.01-0.02 shift is seen for the 1220°C soak, and a ~0.01 shift is seen for the 1330°C soak. Behavior in spectral regions in which atmospheric gases influence the signal were ignored in this analysis.

As the time span between measurements at each wavelength value was equal, a constant difference in spectral emittance between first and second scans implies a linear decline in spectral emittance with time from changes to the near-surface microstructure. This was generally the case with the exception of the shorter wavelengths (1000-2400 nm). Adopting this assumption, the spectral emittance plots were modified to correct for the decline in emittance values over the wavelength scan period. These corrected data are shown in Figure 5.8. The corrected spectral emittance data for the three soak temperatures overlapped in values over much of the measured spectrum. The increase in spectral emittance from ~0.76 at 1000 nm to 0.90 at 6000 nm is in contrast to the behavior of pure metals such as tungsten and platinum, which show a decrease in spectral emittance with longer wavelengths [5]. Dielectrics such as Al_2O_3 display a peak in spectral emmissivity (~ 20 μ at 1400°C [5]). Thus, the measured spectral emissivity dependence on wavelength may be speculated to be a result of the rising spectral emittance of the oxide coating of the ribbon over the 1-6 μm range, toward a longer wavelength maximum.

The spectral emittance of the oxidized ribbons is likely a complex combination of the emission behavior of the metallically-conducting ribbon interior and the multi-phase dielectric coating. Emissions from the metallic interior may transmit directly through more non-absorbing portions of the spectrum of the oxide coating, while in absorbing spectral
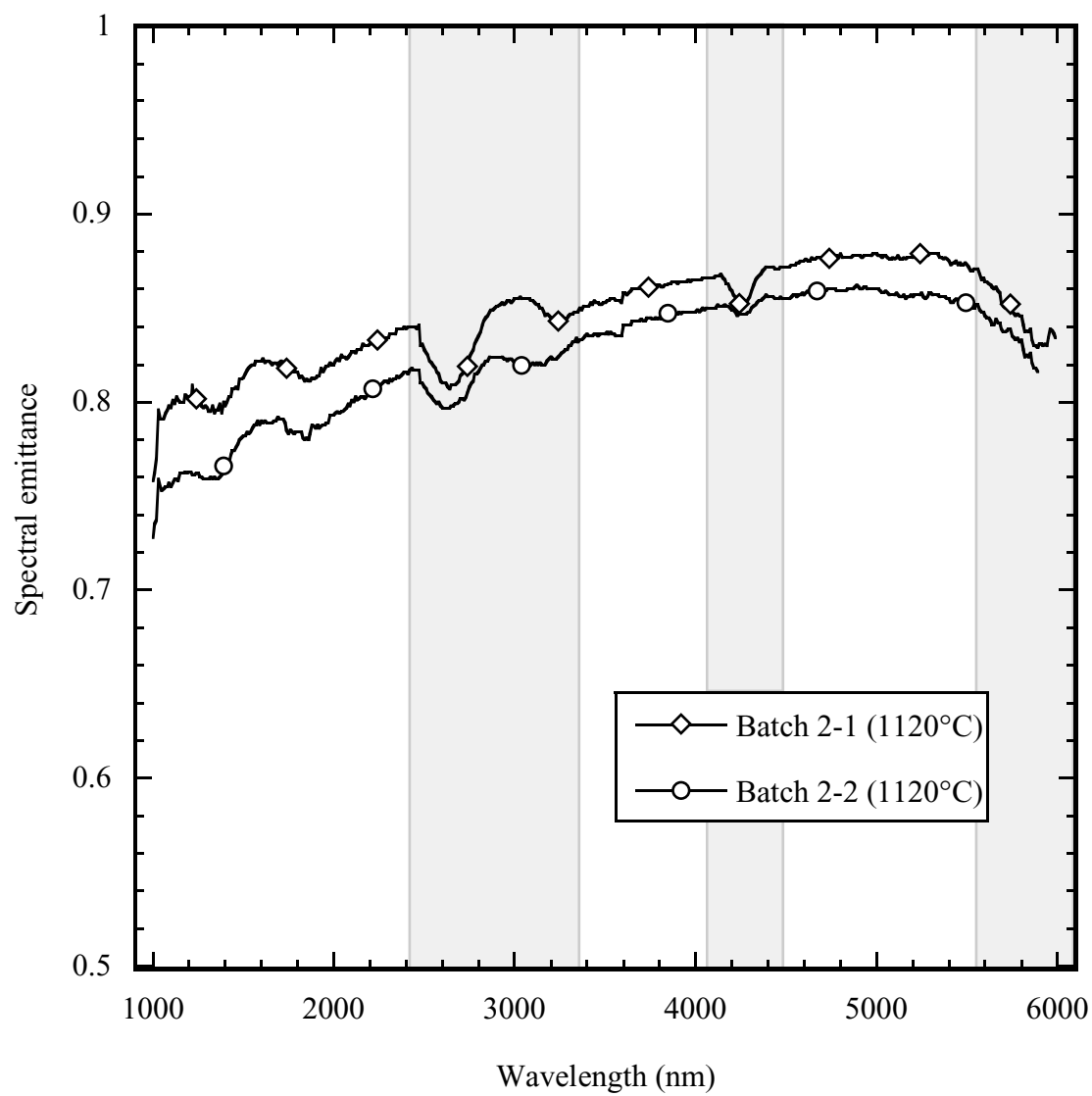
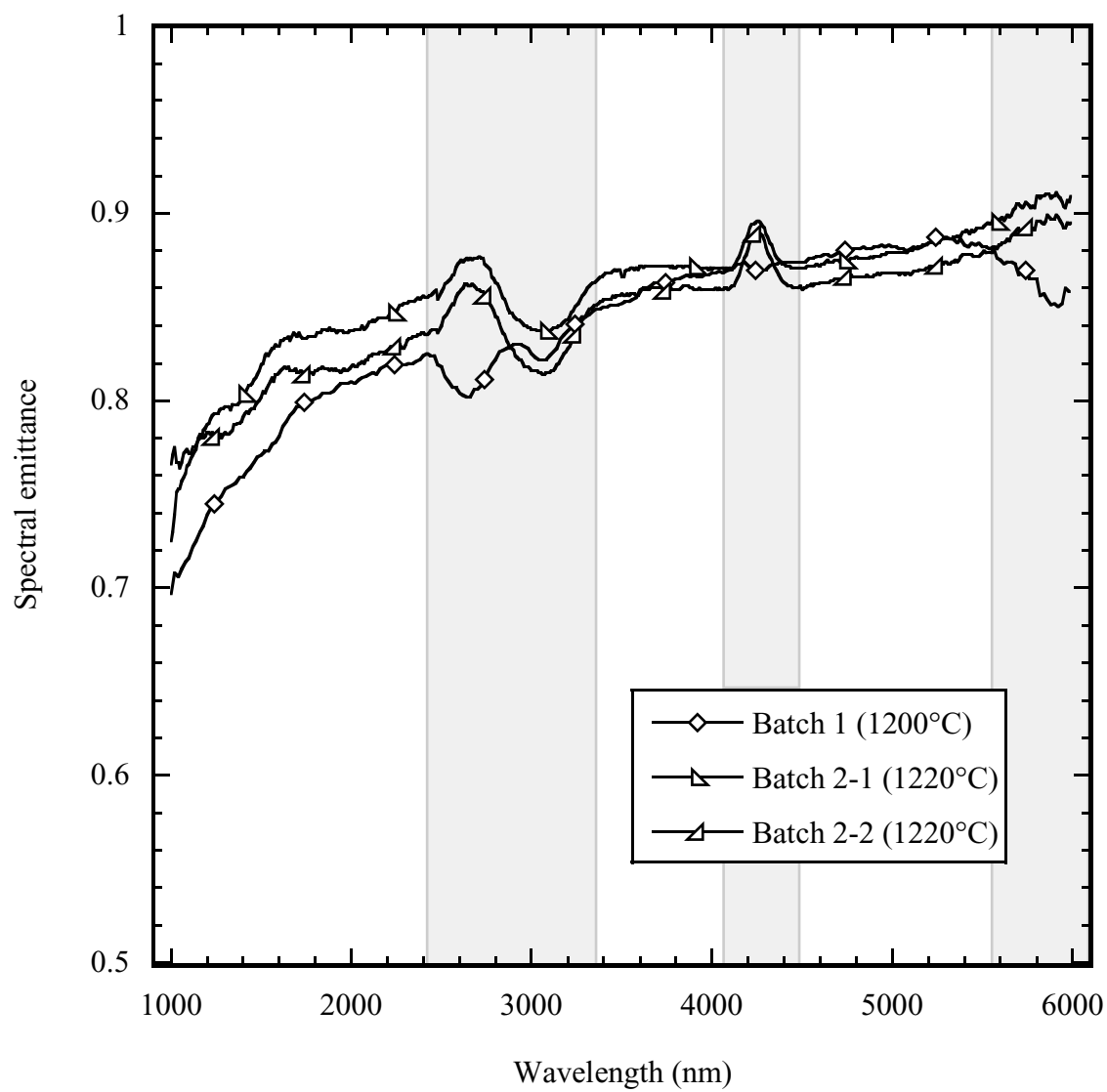Figure 5.4: Spectral emittance values for specimens at ∼1120°C.

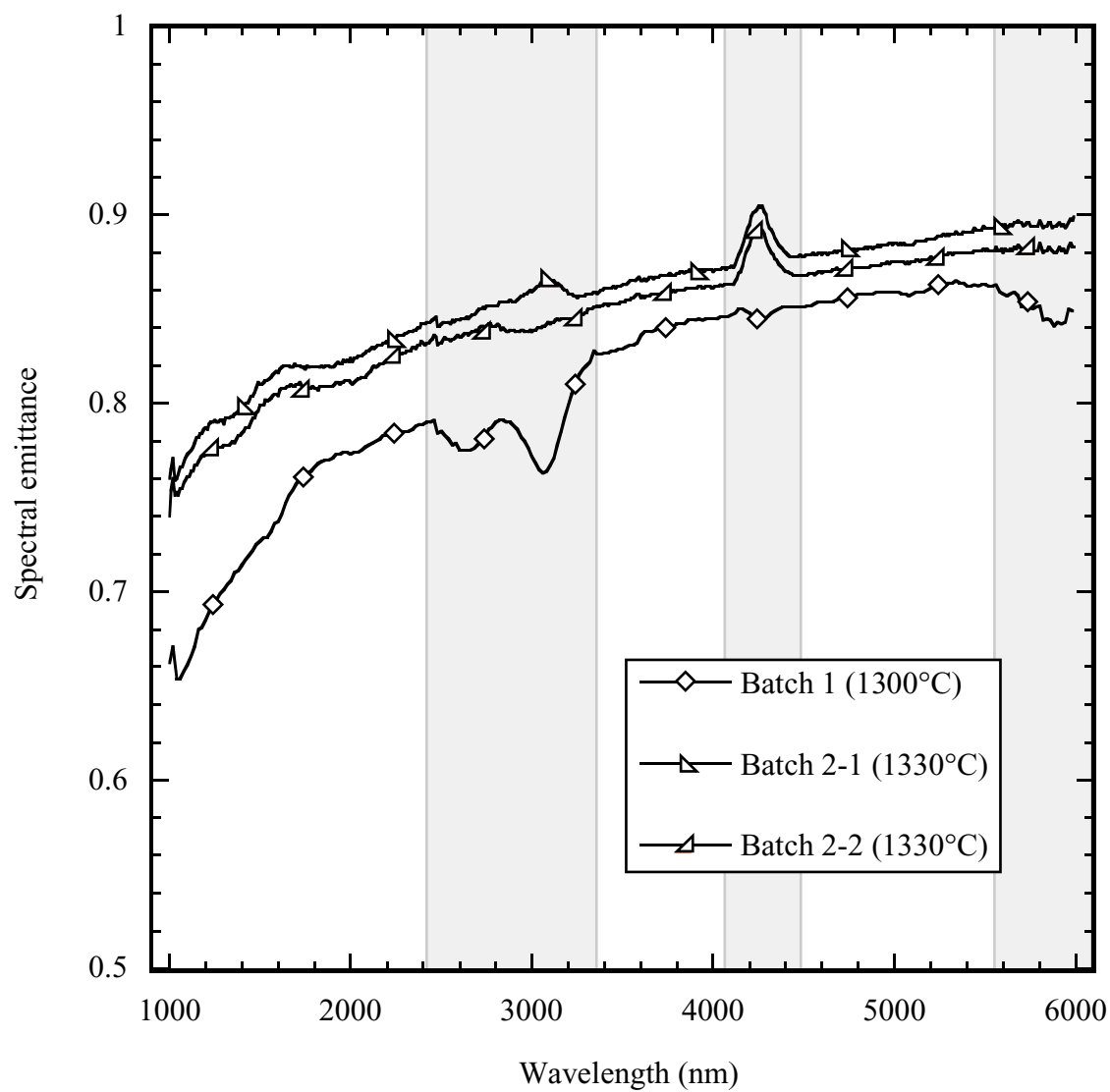Figure 5.5: Spectral emittance values for specimens at 1200-1220°C.

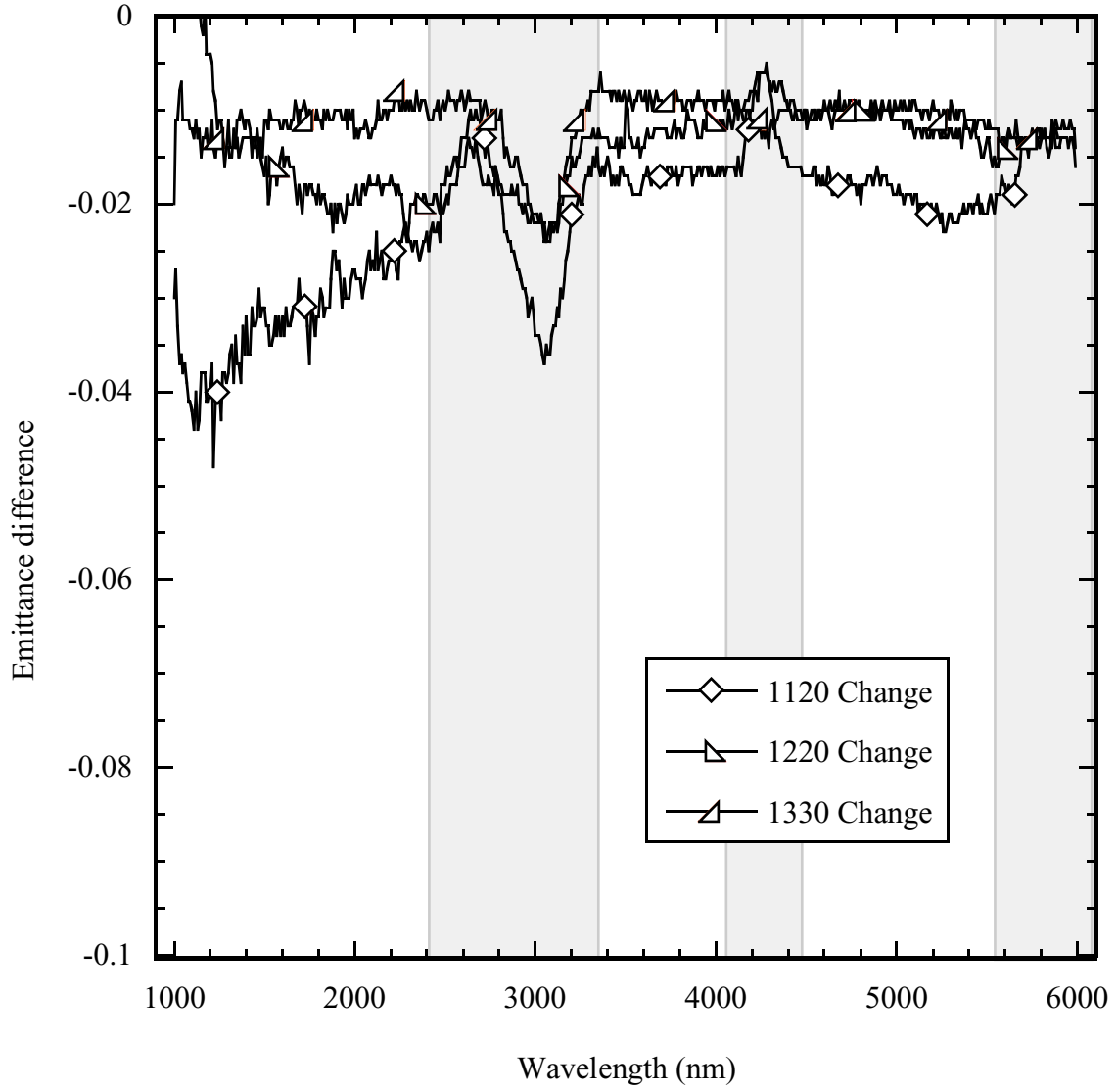Figure 5.6: Emittance values for specimens at 1300-1330°C.

Figure 5.7: Differences in the observed spectral emittance values obtained during the subsequent observations of the second batch of oxidized ribbons held at temperatures (based on Wein's displacement law) of 1120, 1220, and 1330°C. Data points obtained by subtracting the emittance values of the first observation from those of the second; the difference corresponds to the change in apparent spectral emittance after ∼30 min at the indicated temperature.
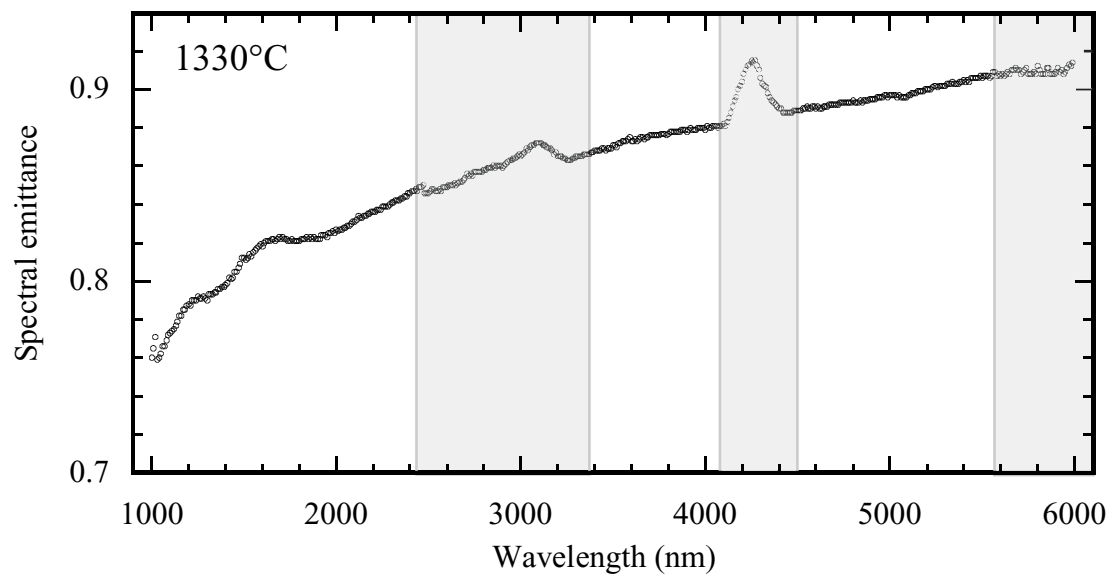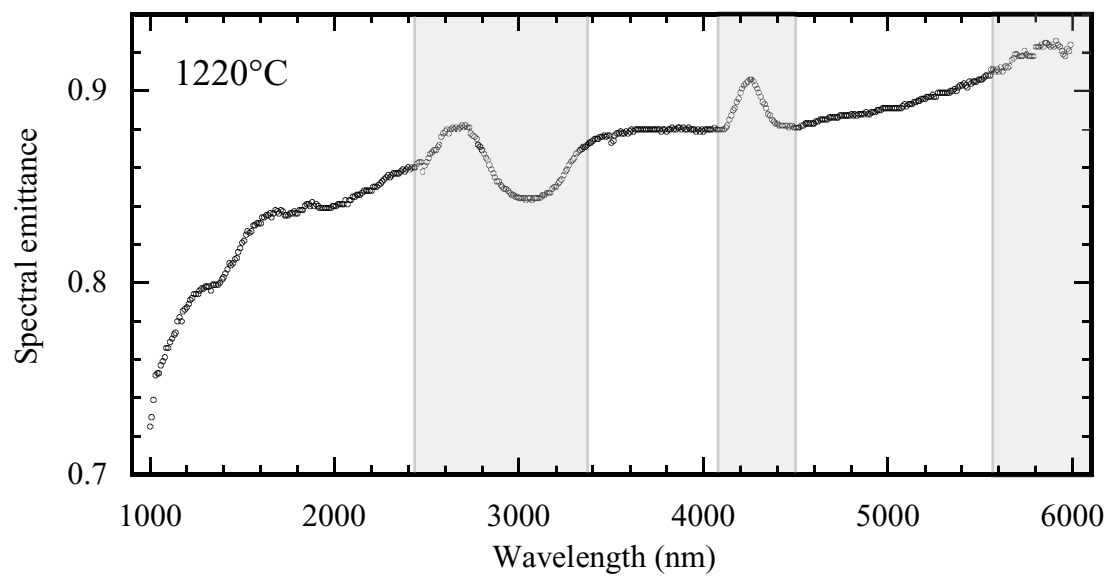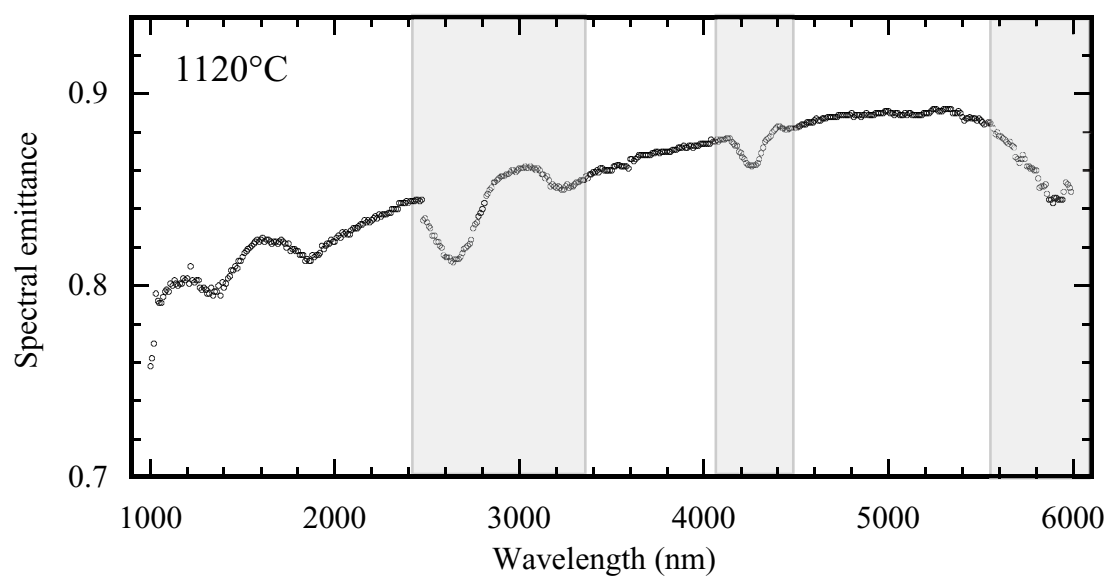
Figure 5.8: Corrected spectral emittances.

regions of the dielectric, it may capture and re-radiate an interior emission. The multi-phase and potentially porous nature of the oxide coating would certainly increase the emittance of the ribbon as compared to a ribbon of a polished metal. Average emittances in the 1-6 μm range of 0.8-0.9 imply that these materials in service as UHTC's will efficiently dispose of thermal energy by radiation.

Bibliography

[1] Touloukian, Y. S. *Thermophysical Properties of Matter*: the TPRC Data Series; a Comprehensive Compilation of Data. New York: IFI/Plenum, 1970.

[2] S. N. Karlsdottir, J. W. Halloran, and A. N. Grundy, "Zirconia Transport by Liquid Convection during Oxidation of Zirconium Diboride-Silicon Carbide," *J. Am. Ceram. Soc.,* **91** [1] 272-277 (2008).

[3] L. Scatteia, D. Alfano, F. Monteverde, J. Sans, and M. Balat-Pichelin. "Effect of the Machining Method on the Catalycity and Emissivity of ZrB_2 and ZrB_2-HfB_2-Based Ceramics," *J. Am. Ceram. Soc.,* **91** [5] 1461-8 (2008).

[4] F. Peng and R. F. Speyer, "Oxidation Resistance of Fully Dense ZrB_2 with SiC, TaB_2, and $TaSi_2$ Additives," *J. Am. Ceram. Soc.,* **91** [5] 1489-1494 (2008).

[5] R. Siegel, J. R. Howell, *Thermal Radiation Heat Transfer*, Fourth Edition, Taylor and Francis, New York, 2002.